Interfacial Mechanics in Fiber-Reinforced Composites: Mechanics of Single and Multiple Cracks in CMCs

Byung Ki Ahn

Dissertation submitted to the Faculty of the
Virginia Polytechnic Institute and State University
in partial fulfillment of the requirements for the degree of

DOCTOR OF PHILOSOPHY
in
Engineering Mechanics

William A. Curtin, Chair
David A. Dillard
Leonard Meirovitch
Kenneth L. Reifsnider
Yuriko Renardy

December 12, 1997
Blacksburg, Virginia

Keywords: ceramic matrix composites, crack deflection/penetration, energy criterion, sliding interface, multiple matrix cracking, statistical aspects

Interfacial Mechanics in Fiber-Reinforced Composites: Mechanics of Single and Multiple Cracks in CMCs

Byung Ki Ahn

(ABSTRACT)

Several critical issues in the mechanics of the interface between the fibers and matrix in ceramic matrix composites (CMCs) are studied. The first issue is the competition between crack deflection and penetration at the fiber/matrix interface. When a matrix crack, the first fracture mode in a CMC, reaches the interface, two different crack modes are possible; crack deflection along the interface and crack penetration into the fibers. A criterion based on strain energy release rates is developed to determine the crack propagation at the interface. The Axisymmetric Damage Model (ADM), a newly-developed numerical technique, is used to obtain the strain energy in the cracked composite. The results are compared with a commonly-used analytic solution provided by He and Hutchinson (HH), and also with experimental data on a limited basis.

The second issue is the stress distribution near the debond/sliding interface. If the interface is weak enough for the main matrix crack to deflect and form a debond/sliding zone, then the stress distribution around the sliding interface is of interest because it provides insight into further cracking modes, i.e. multiple matrix cracking or possibly fiber failure. The stress distributions are obtained by the ADM and compared to a simple shear-lag model in which a constant sliding resistance is assumed. The results show that the

matrix axial stress, which is responsible for further matrix cracking, is accurately predicted by the shear-lag model.

Finally, the third issue is multiple matrix cracking. We present a theory to predict the stress/strain relations and unload/reload hysteresis behavior during the evolution of multiple matrix cracking. The random spacings between the matrix cracks as well as the crack interactions are taken into account in the model. The procedure to obtain the interfacial sliding resistance, thermal residual stress, and matrix flaw distribution from the experimental stress/strain data is discussed. The results are compared to a commonly-used approach in which uniform crack spacings are assumed.

Overall, we have considered various crack modes in the fiber-reinforced CMCs; from a single matrix crack to multiple matrix cracking, and have suggested models to predict the microscopic crack behavior and to evaluate the macroscopic stress/strain relations. The damage tolerance or toughening due to the inelastic strains caused by matrix cracking phenomenon is the key issue of this study, and the interfacial mechanics in conjunction with the crack behavior is the main issue discussed here. The models can be used to interpret experimental data such as micrographs of crack surface or extent of crack damage, and stress/strain curves, and in general the models can be used as guidelines to design tougher composites.

Dedication

This work is dedicated to my parents and my wife.

Without their sacrifices and undying support I could have never fulfilled my dreams.

ACKNOWLEDGEMENTS

The author wishes to thank the following individuals for their contribution to this work:

- Dr. William A. Curtin for providing the opportunity to perform this work and guiding me in the right direction whenever I was lost. Without his timely advice and encouragement, I would still be coming back to my office after midnight to work. He also showed me that "TO THINK" is the first step in solving any complicated problem.
- Dr. Loenard Meirovitch, Dr. Kenneth L. Reifsnider, Dr. David A. Dillard, and Dr. Yuriko Renardy for taking time away from their busy schedules to serve on my committee.
- Dr. Nicholas J. Pagano at Wright-Patterson Air Force Base for his help with the ADM code. He never minded answering any of my silly questions.
- U.S. Air Force Office of Scientific Research and Hyper-Therm Co. for the support of this research.
- Dr. Hyo-Chul Sin, my Master's thesis advisor at Seoul National University for encouraging me to study abroad.
- My parents, Yoon-Mo Ahn and Sang-Sook Nam, and my brothers, Byung-Jae and Heejoon for their caring and patience. They surely deserve all the credit.
- My wife, Jaewon, for her immeasurable love and endless support. She has been a constant source of strength and a brilliant helper throughout times of adversity while trying to fulfill my goal.
- My daughter, Grace Hayne for cheering me up since she first opened her eyes at the Radford Hospital.
- Ms. Shelia Collins of Materials Response Group and Ms. Cindy Hopkins of Engineering Science and Mechanics department for their excellent job in setting

everything in order. I also wish to extend to my thanks to former MRG employees, Ms. Paula Lee and Melba Morrozoff for their efficient secretarial work.

- Dr. Curtin's group members and ex-members; Dr. Nirmal Iyengar, Dr. M'hammed Ibnabdeljalil, Mr. Howard Halverson, Mr. Rob Carter, Mr. Glenn Foster and Mr. Brendan Fabeny for the fruitful discussions on research and life in general.
- Past and present MRG members; Dr. Hari Parvatareddy, Dr. Scott Case, Dr. Yong Li Xu, Dr. Wen-Lung Liu, Dr. Axinte Ionita, Mr. Mike Pastor, Mr. Blair Russell, Mr. Ari Caliskan, Mr. Fred McBagonluri-Nuri, Mr. Nikhil Verghese, Mr. Jean-Matthieu Bodin, Mr. Steve Phifer, Mr. Brady Walther, Mr. Mike Hayes, Ms. Celine Maiheux and Ms. Sneha Patel for their contributions to the positive working environment of the MRG. They came from all over the world, but have all become part of the "Chicago maroon and burnt orange of the Hokies".
- My friends in Korean community; Rev. Hyun Chung, Dr. and Mrs. Sang-Gyun Kim, Dr. and Mrs. Sungsoo Na, Dr. and Mrs. Dal-Yong Ohm, Mr. Myung-Hyun Kim, and Mr. and Mrs. Tae-In Hyon for their true friendship in Christ.
- Members of Korean Campus Crusade for Christ of Virginia Tech with whom I had the honor to serve as their staff member. Without their sincere prayer, I would have been frustrated so many times.
- Finally, but most importantly, I thank God Almighty and Jesus Christ, my Lord and Savior for giving me the will power and strength to make it this far when I didn't see a light.

TABLE OF CONTENTS

LIST OF FIGURES

LIST OF TABLES

Chapter 1. INTRODUCTION

Ceramic materials are attractive for use in high temperature applications because of their high strength and low density. Their service temperature limits are as high as 1500° C, which are far beyond the limits of polymers and metals, two of the most frequently used material systems in the modern applications of structural materials. However, low fracture toughness, or poor resistance against crack propagation, of monolithic ceramics restricts their use to a large extent. Unlike polymers or metals, ceramics do not show visco-elastic or plastic deformations under tensile and impact loading conditions. The absence of such energy absorbing phenomena in ceramics leads to catastrophic failure of the materials once a pre-existing microscopic flaw (or crack) grows and propagates. It is understandable that the major effort in developing advanced ceramic materials has been focused on enhancing fracture toughness of ceramics, thereby imparting to them a damage-tolerant behavior [1-3].

Reinforcing ceramics with ceramic fibers has been shown to be very effective for improving toughness, and despite the difficulty in their manufacturing process due to the brittleness of the constituents, ceramic matrix composites (CMCs) are a promising material system in the field requiring strong and tough materials. It is now well established that many of the mechanical properties of the fiber-reinforced composites are determined by the conditions of the fiber/matrix interface, and the behavior of cracks at the interface is known to be the key factor for obtaining the enhanced toughness [1,2]. The importance of the interface in the CMCs stems from three main reasons: (1) the interface occupies a very large area and it possibly contains small voids or flaws which reduce the transverse strength of the composite; (2) the interface is an area of discontinuity in the thermomechanical properties such as elastic modulus, strength, fracture toughness and thermal expansion coefficient; and (3) debonding at the interface can contribute to enhancing fracture toughness. Characterization of the physics and mechanics of the interface is thus necessary to understand the overall characteristics of the fracture of CMCs.

In most CMCs, the failure strain of the matrix in uniaxial tension is generally smaller than that of fibers, and this provides the reasonable assumption that the first crack in a ceramic composite is developed from the largest intrinsic flaw in the matrix. Under increasing tensile loading in the fiber direction, this microcrack grows until it reaches the fiber/matrix interface; then it may either deflect along the interface or penetrate into the fiber. If the interface is weak enough for the matrix crack to be deflected along the interface, the fibers remain intact and the composite can be tough. If the interface is too strong, the matrix crack penetrates into the fibers and the composite becomes brittle like a monolithic ceramic. Therefore, the crack propagation behavior at the interface is critical to toughening in CMCs. The prerequisite conditions to obtain an interfacial debond crack from a main matrix crack has recently been analyzed in terms of energy release rates by a number of researchers [17-19]. The deflection of a matrix crack at the fiber/matrix interface is assumed to occur when the energy required to grow the interfacial debond crack is less than that required to grow the crack across the interface. Since crack deflection is a desirable failure mode from a toughness perspective, as compared to brittle cracking through the fibers, one can use such criteria as a design guide to determine the interfacial toughness to obtain deflection, considering the underlying parameters which dictate the criteria, such as elastic modulus and Poisson's ratio.

Supposing the matrix crack is induced to deflect at the fiber/matrix interface, it is of considerable importance to understand the growth of the deflected crack with increasing load, and the stresses around the crack that may or may not drive further cracking. Slip or sliding along the interface around the matrix crack plane is then critical to determining the stress distributions in the composite constituents, and the stress concentration near the matrix crack tip and the debond crack tip may dictate the next possible failure mode. Traditionally, stress analysis around a matrix crack or a debond crack is performed using simple shear-lag models which provide analytic results and satisfy some aspects of basic equilibrium. However, the models assume that the axial stresses in the matrix or fibers are uniform on the respective surface and neglect the possibly important variations of the

stresses in the direction perpendicular to the fiber orientation. Various approaches have been suggested to take the variations into account for model composites in which sliding interfaces are assumed, and to study the effect of a frictional interface on the stress distributions and the extent of debonding [42,53-55]. It is understood that the size of the slip region is a function of the applied loads as well as the sliding resistance at the interface, τ. It should be noted again that debonding and frictional sliding contribute to energy absorbing mechanisms of CMCs and lead to a noncatastrophic gradual failure of the composites.

In CMCs, multiple matrix cracking is another important phenomenon involved in toughening. Even though not directly related to the ultimate composite strength, multiple matrix cracking is the first nonlinear event under tensile loading, and the inelastic strains associated with matrix cracking are responsible for the considerable damage tolerance in these materials. Fig. 1.1 shows an SEM (Scanning Electron Microscope) micrograph of a multiply matrix cracked CMC (SiC/SiC). Crack bridging by the intact fibers is also evident. The inelastic strains caused by the matrix cracks are most directly assessed on unidirectional materials, for which the stress/stain behavior is illustrated schematically in Fig. 1.2. The onset of matrix cracking occurs at the stress σ^*-σ_{th} , and σ_s is the stress at which matrix cracks saturate. A key feature determining the onset is the interfacial sliding resistance τ after interfacial debonding. Traditionally, experimental approaches such as pull-out test and push-out test [66-68] were used to measure the sliding resistance, and recently, more reliable ways to evaluate τ at elevated temperatures using the measured crack spacing, composite stress/strain curves, or hysteresis loops have been devised [80-82]. Overall, understanding the multiple matrix cracking is a valuable means for determining the in-situ fiber/matrix interfacial quantities, such as τ, which are directly relevant to composite strength and work-of-fracture [2,3,78].

The main purpose of this research is to study the crack evolution phenomena in ceramic matrix composites before fiber failure occurs, i.e. from a single matrix crack impinging upon the fiber/matrix interface up to the crack saturation at which multiple matrix

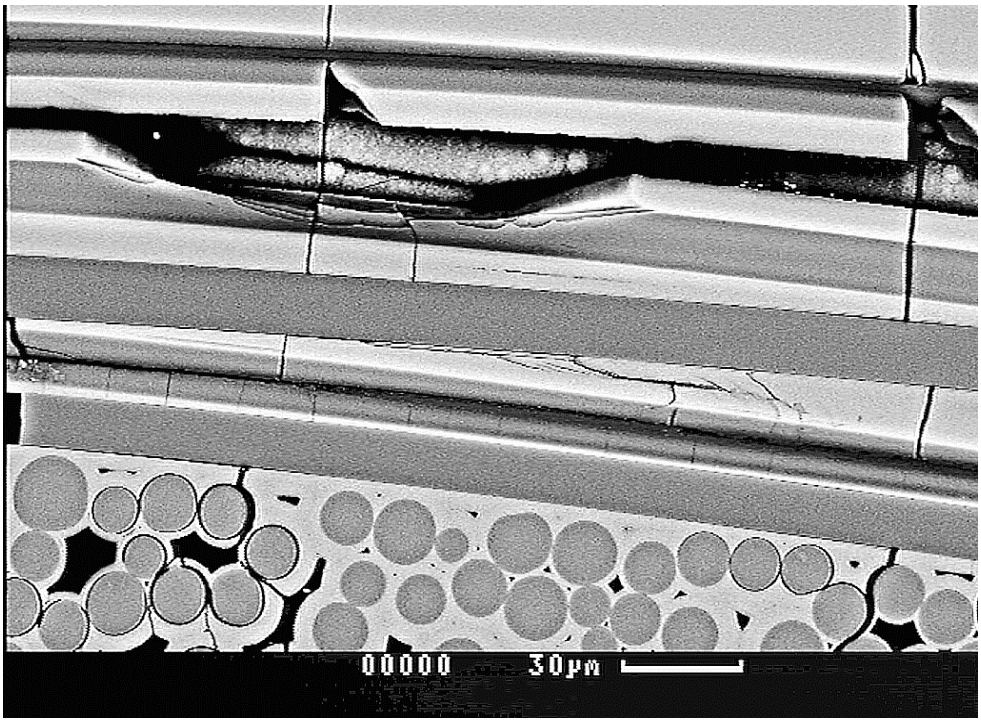

Figure 1.1: SEM micrograph of SiC/SiC composite showing multiple matrix cracks. (Courtesy Robert Carter, Virginia Tech.)

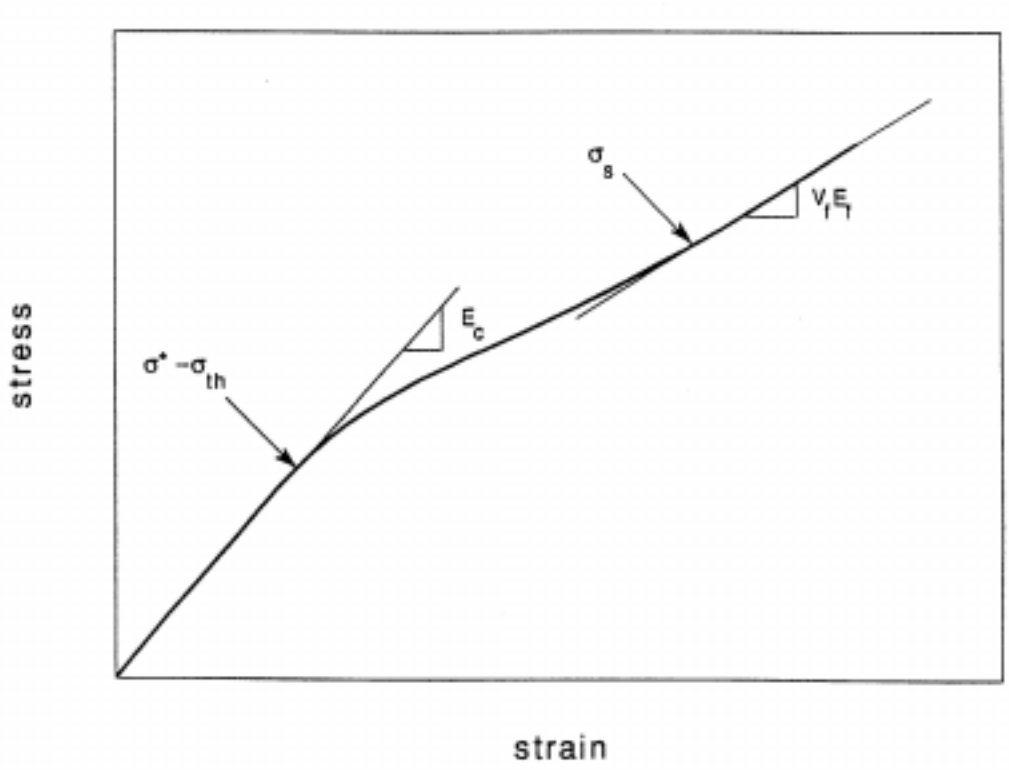

Figure 1.2: Tensile stress/strain behavior of a uni-directional fiber-reinforced composite loaded in the fiber direction.

cracking ceases. We discuss three different research problems involving each of the critical mechanics issues in fiber-reinforced CMCs: (1) assessing crack deflection/penetration at interfaces; (2) determining the stress state around a slipping interface; and finally (3) relating the evolution of multiple matrix cracking to the measured stress/strain behavior. Primarily, we desire to properly model the above problems and solve them using recent developed theories. The modeling efforts are performed on the recognition that since traditional empirical procedures to optimize the variable constituents property profiles for composite design are expensive, such mechanism-based models are needed [2]. The models and techniques presented here are based on the linear elasticity or linear elastic fracture mechanics which are adequate to analyze the ceramic-based materials. Considering the increasing need of CMCs in the aerospace and nuclear applications, these analyses through modeling approaches will possibly not only reduce total material development cost in those fields but also provide insight into developing better composites.

The remainder of this dissertation is organized as follows. Chapter 2 discusses the problem of prediction of the crack propagation at the fiber/matrix interface. A circular edge type matrix crack in a cylindrical composite geometry is assumed to be approaching the interface, and the relative tendency of the crack to penetrate the interface or deflect along the interface is examined. In general, we have developed a criterion for determining deflection versus penetration as a function of the fiber and matrix elastic mismatch, finite fiber volume fraction, and length of the deflected or penetrated crack. Several detailed examples are presented and the results compared with a widely-used approach in which "zero" fiber volume fraction is assumed. To do this requires the calculations of energy release rates as the matrix crack grows, and we adopt the Axisymmetric Damage Model (ADM), a numerical approach recently developed by Pagano and his colleagues [25,26]. The ADM model will be described in detail with a theoretical background and examples of possible applications. In the present study, we also desire to understand the significance of the crack extension lengths and try to correlate them to available experimental data. Crack extension lengths are needed to calculate the energy release rates from the obtained

strain or potential energies, and they are assumed to be infinitesimal in all existing analytical works [17-19]. However, in that extreme range for the crack extensions the energy release rates are not practically physical, and there must be some intrinsic length scales at which the continuum limits apply. We present some recent results to assess the effect of finite crack extensions on the crack deflection criteria. We then investigate the effect of different crack extensions for the deflected and penetrating cracks and the effect of pre-existing cracks in the fiber and along the interface on the suggested criteria.

In Chapter 3, we investigate the stress fields in a composite around a frictional interface which is developed along the deflected interface crack. We assumed, in Chapter 2, the interface crack from the main matrix crack is a traction-free open crack, which is reasonable for a tiny incipient crack. However, the assumption does not hold any longer if the crack propagates along the interface and makes a finite size of debond zone. Thus, we postulate here that after interface debonding occurs, the clamping stress at the interface due to thermal mismatch or roughness between fiber and matrix is large enough to induce a sliding zone with friction. An axisymmetric geometry is assumed for model composites, and the ADM model is utilized to solve for the stress distributions under given boundary conditions. The axial stress profiles in the fiber and matrix are analyzed to understand the stress distributions within the debond zone. In general, the simple shear-lag model in which a constant τ is assumed appears to be accurate enough to predict the matrix stress distributions and the average fiber stress across the cross-section distribution, but it cannot estimate the near-tip stresses due to its incapability of assessing the stress singularity. The ADM is then used to study the radial variations in the axial stresses in the fiber. However, since accurate analysis of fiber failure requires Weibull statistics for the fiber flaws as well-documented in Weitsman and Zhu [69], the detailed stress analysis and its influence on fiber failure will remain as one of recommendations for future study.

In Chapter 4, the multiple matrix cracking phenomenon is studied from a stochastic viewpoint. A theory is presented to predict the stress/strain relations and unload/reload hysteresis behavior during the evolution of multiple matrix cracking in unidirectional fiber-

reinforced CMCs. The theory uses the shear-lag model which is found to be accurate for the matrix stress analysis in Chapter 3. The theory is based on the similarity between multiple matrix cracking and fiber fragmentation in a single fiber composite, and determines the crack and strain evolution as a function of the statistical distribution of initial flaws in the material, the interfacial sliding resistance τ, and the thermal residual stresses in the composite. The procedure by which experimental stress/strain and hysteresis data can be interpreted to derive values for the interfacial shear stress, thermal stresses, and intrinsic matrix flaw distribution is discussed. Several examples are presented, and the results are compared to an approach in which the crack spacing is assumed constant and equal to the average spacing obtained directly from experiment. The effect of changing temperature, and hence residual stresses, without changing either matrix flaws or interfacial sliding resistance, is also studied.

Finally, in Chapter 5, overall conclusions will be presented. As discussed above, the main purpose of this research is to identify the matrix crack evolution in the fiber-reinforced CMCs. Among the practical goals in the design of CMCs, toughness enhancement to avoid catastrophic composite failure is our primary concern. Of most importance in the modeling effort of a matrix crack impinging upon an interface, we have examined the relative tendency of the crack to penetrate the interface or deflect. We have developed a criterion for determining penetration versus deflection for an axisymmetric cylindrical composite geometry; this criterion can be used as a design guide to determine the interfacial toughness required to obtain deflection. For a deflected crack with a finite size of debond slip zone, we have analyzed the microstresses in the fiber and matrix as a function of slip length and applied stress. Results show that the matrix stresses in the debond zone are nearly independent of the radial positions, which is actually one of the assumptions of shear-lag models. Stresses in the fiber are also calculated to examine the radial variations in the fiber axial stresses. Through these efforts, validity and limits of the shear-lag model used in this study is assessed. Finally for the multiple matrix cracking problem, we have developed a model to predict the stress/strain relations and hysteresis behavior. The model includes all statistical aspects such as fragment length distribution

and the intrinsic flaw distribution. We have suggested a relatively simple and convenient method to obtain the interfacial sliding resistance from the stress/stain or hysteresis curves, which is substantially useful for the materials systems in high temperature conditions. Recommendations for future study will be discussed for each of these problems.

Chapter 2. CRACK DEFLECTION AND PENETRATION AT INTERFACES

Deflection of a matrix crack at the fiber/matrix interface is the initial mechanism required for obtaining enhanced toughness in ceramic matrix composites. In this Chapter, a criterion is presented to predict the competition between crack deflection and penetration at the interface, using an energy criterion analogous to that suggested by He and Hutchinson [17]. The Axisymmetric Damage Model (ADM) developed by Pagano [25] is used to calculate the strain energy release rates for matrix cracks that either deflect or penetrate at the interface of an axisymmetric composite as a function of elastic mismatch, fiber volume fraction, and length of the deflected or penetrated crack. Results show that, for equal crack extensions in deflection and penetration, crack deflection is more difficult for finite crack extension and finite fiber volume fraction than in the He and Hutchinson limit of zero volume fraction and/or infinitesimal crack extension. Allowing for different crack extensions for the deflected and penetrating cracks is shown to have a small effect at larger volume fractions. Fracture mode data on model composites with well-established constitutive properties show penetration into the fibers, as predicted by the present criteria and in contrast to the He and Hutchinson criterion, which predicts crack deflection. This result suggests that the latter criterion may overestimate the prospects for crack deflection in composites with realistic fiber volume fractions and high ratios of fiber to matrix elastic modulus. The effect of pre-existing cracks in fiber and along fiber/matrix interface on the criteria is also evaluated. The pre-existing cracks are assumed to be connected to the main matrix crack at the fiber/matrix interface. It appears that having two pre-existing cracks of the same size in both directions at the same time encourages crack penetration rather than deflection. From these results, we conclude that the finite values of fiber volume fraction and crack extension lengths play an important role in determining the tendency for interfacial crack deflection, which in turn then controls the toughness of entire composite, even though the physical interpretation of the crack extension lengths is still an unsolved issue.

A discussion of relating the crack extension to the size of the flaws in the fiber or along the interface is presented in the summary.

2.1. Introduction

2.1.1 Crack Behavior at Interfaces

Before the problem of crack deflection/penetration at a bi-material interface is addressed, the general problem of an interface crack is briefly outlined. A good deal of basic research on the problem of crack propagation at an interface between two dissimilar materials has been accomplished since the late 1950's. In an enlightening paper, Williams [4] considered the interface crack problem in plane elasticity and for the first time he found the so-called oscillatory near-tip behavior for stresses and displacements. Williams used an eigenfunction expansion technique to solve the interface crack problem and discovered that the stresses ahead of the crack tip possess an oscillatory character of the type $r^{-1/2}sin$ (or cos) of the argument $\varepsilon log r$, where r is the radial distance from the crack tip and ε is a function of material constants

$$\varepsilon = \frac{1}{2\pi}\ln\left[\left(\frac{\kappa_1}{\mu_1}+\frac{1}{\mu_2}\right)\Big/\left(\frac{\kappa_2}{\mu_2}+\frac{1}{\mu_1}\right)\right] = \frac{1}{2\pi}\ln\left(\frac{1-\beta}{1+\beta}\right) \quad . \tag{2.1}$$

In Eq. (2.1), μ_i are the shear moduli of the two adjoining materials, and $\kappa_i=3-4\nu_i$ for plane strain and $\kappa_i=(3-\nu_i)/(1+\nu_i)$ for plane stress where ν_i are the Poisson's ratios. β is one of the elastic mismatch parameters defined by Dundurs [5] as

$$\alpha = \frac{\mu_1(\kappa_2+1)-\mu_2(\kappa_1+1)}{\mu_1(\kappa_2+1)+\mu_2(\kappa_1+1)} \quad , \quad \beta = \frac{\mu_1(\kappa_2-1)-\mu_2(\kappa_1-1)}{\mu_1(\kappa_2+1)+\mu_2(\kappa_1+1)} \quad . \tag{2.2a}$$

For a *linear elastic* composite material, consisting of a fiber and a matrix, under *plane strain* assumptions, Eq. (2.2a) can be rewritten as

$$\alpha = \frac{E_f\left(1-\nu_m{}^2\right)-E_m\left(1-\nu_f{}^2\right)}{E_f\left(1-\nu_m{}^2\right)+E_m\left(1-\nu_f{}^2\right)} \quad , \tag{2.2b}$$

$$2\beta = \frac{E_f\left(1+\nu_m\right)\left(1-2\nu_m\right)-E_m\left(1+\nu_f\right)\left(1-2\nu_f\right)}{E_f\left(1-\nu_m{}^2\right)+E_m\left(1-\nu_f{}^2\right)} \quad .$$

where subscripts *f* and *m* refer to the fiber (material *1* in Eq. (2.2a)) and the matrix (material *2*), respectively. In Eq. (2.2b), the parameter α approaches +1 when the stiffness of fiber is extremely large compared to the stiffness of matrix, and both parameters become zero in the case of homogeneous material systems. If the materials of the fiber and the matrix are switched both α and β change signs.

While the approach by Williams [4] was a pioneering method for determining qualitatively the characteristic behavior in the vicinity of crack tips, it did not give the solution quantitatively, i.e. the stresses are not specifically given as a function of *r* and θ, with θ being the angle between *r* and the crack plane. Furthermore, Williams gave eigenvalues λ of the form $\lambda=n(integer)-1/2+i\varepsilon$, with near-tip stress varying in proportional to r^{λ}, but did not consider other possible integer eigenvalues of the form $\lambda=n$. Hence, the full form of the near tip field for the interface crack was not successfully obtained.

Among more advanced approaches to quantitatively investigate the stress distributions near crack tips were the work by Erdogan [6,7] and Rice and Sih [8]. Erdogan [6] considered the stress distribution in two semi-infinite elastic planes subjected to external loads at infinity. He confirmed the oscillating stresses observed by Williams [4] and obtained the relations between stress intensity factors and applied loads for some example

problems with more general loading conditions including the residual thermal stresses due to temperature changes, tractions on the crack surfaces, and concentrated forces and couples at arbitrary locations. More importantly, Erdogan estimated that the oscillatory region is infinitesimally small compared to the finite bonded zone between two neighboring interface cracks and concluded that, for all practical purposes, the oscillating phenomenon may be ignored. Rice and Sih [8] applied the complex variable method to solve the elasticity problems of in-plane extension of two dissimilar materials containing interface cracks. It was shown that the concept of stress intensity factor in the Griffith-Irwin theory of fracture could be extended to cracks in dissimilar materials. It was also recognized that the tensile and shear effects near the crack tip are intrinsically inseparable into analogues of classical mode I and mode II conditions. In contrast to Erdogan's results [6], Rice and Sih showed that the stress intensity factors depend on the bimaterial constant (or oscillation parameter), ε, regardless of the number of bonded zones along the interface (Erdogan claimed that the stress intensity factor does not depend on ε if only "one" bonded zone exists between two infinite-sized interface cracks).

Although the importance and complexity of near-tip stresses in the interface crack problems was recognized in the 1960's, it was more than two decades later when the complete solution for the problem was given by Rice [9]. Using the complex variable function formulation, Rice provided a series solution that includes integer order term that Williams [4] missed in his work. Rice [9] and Hutchinson *et al*. [10] are among the first who have explicitly shown that the singular stress a distance r ahead of the interface crack tip is given by

$$\sigma_{yy} + i\sigma_{xy} = \frac{K}{\sqrt{2\pi r}} r^{i\varepsilon} \tag{2.3}$$

where $K=K_1+iK_2$ is the complex stress intensity factor for interfacial fracture problems. Note that K_1 and K_2 are different from the classical stress intensity factors, K_I and K_{II}.

Instead, as discussed in Rice [9] and Hutchinson *et al*. [10], K is related with the complex intensity factor k_1+ik_2 introduced by Rice and Sih [8] by $K=(k_1+ik_2)\sqrt{\pi}\ cosh(\pi\varepsilon)$, and reduces to K_I+iK_{II} for a homogeneous solid (ε=0). In Eq. (2.3), subscript "x" denotes the parallel axis to the interface between two materials and "y" is for the perpendicular axis to the interface, and the origin of the coordinate is fixed at the tip of the reference crack, which is located at the interface (see Fig. 2.1).

The problem of a crack perpendicular to the elastic bi-material interface, with the crack tip on the interface, was first studied by Zak and Williams [11]. Instead of the square root singularity known from analysis of cracks in homogeneous materials, the stresses near such a crack tip is characterized by

$$\sigma_{xx} = k_I(2\pi y)^{-\lambda} \tag{2.4}$$

where k_I is a Mode I stress-intensity-like factor and the exponent λ represents the strength of stress singularity. It has been shown that the value of λ, which is real and a function of the elastic mismatch between the fiber and matrix, can be determined as a root of the following characteristic equation [11-13]

$$\cos\lambda\pi = \frac{2(\beta-\alpha)}{1+\beta}(1-\lambda)^2 + \frac{\alpha+\beta^2}{1-\beta^2} \quad . \tag{2.5}$$

For infinitesimally sharp cracks physically admissible solutions require $\lambda \leq 1$ with the possible range of α. And for a homogeneous body ($\alpha=\beta=0$) the square root singularity ($\sigma_{xx} \propto y^{-1/2}$ in Eq. (2.4)) is returned, independently of ν [14].

Figure 2.2 shows how λ varies with α in two different cases of β; $\beta=0$ and $\beta\neq0$. To examine the β effect in a simple but realistic manner, we fix the Poisson's ratios of fiber and matrix so that β can be proportional to α over all α. The dotted line represents the

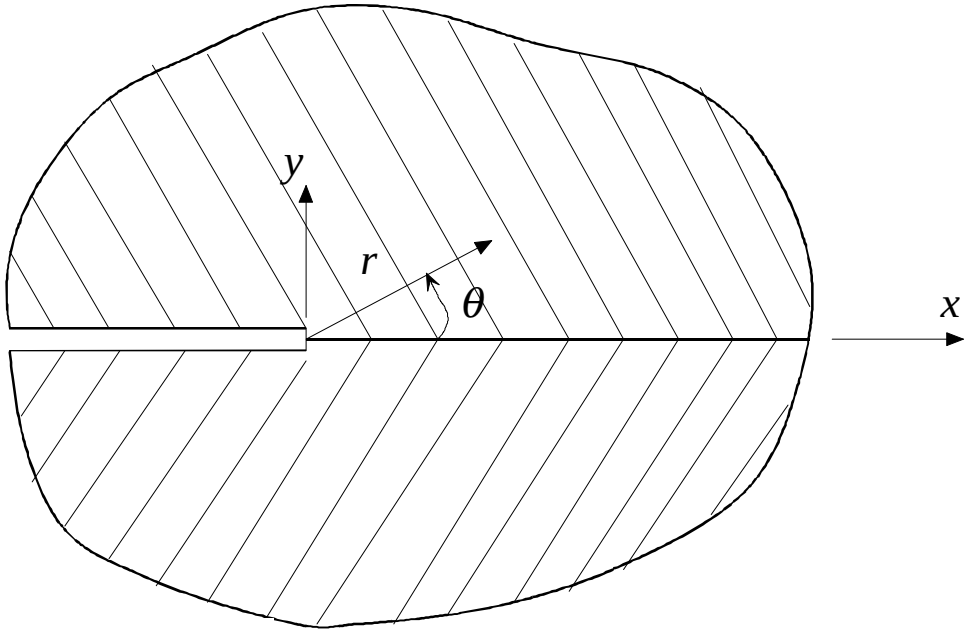

Figure 2.1: Interface crack between two different materials. Local r-θ coordinate system at the crack tip is shown.

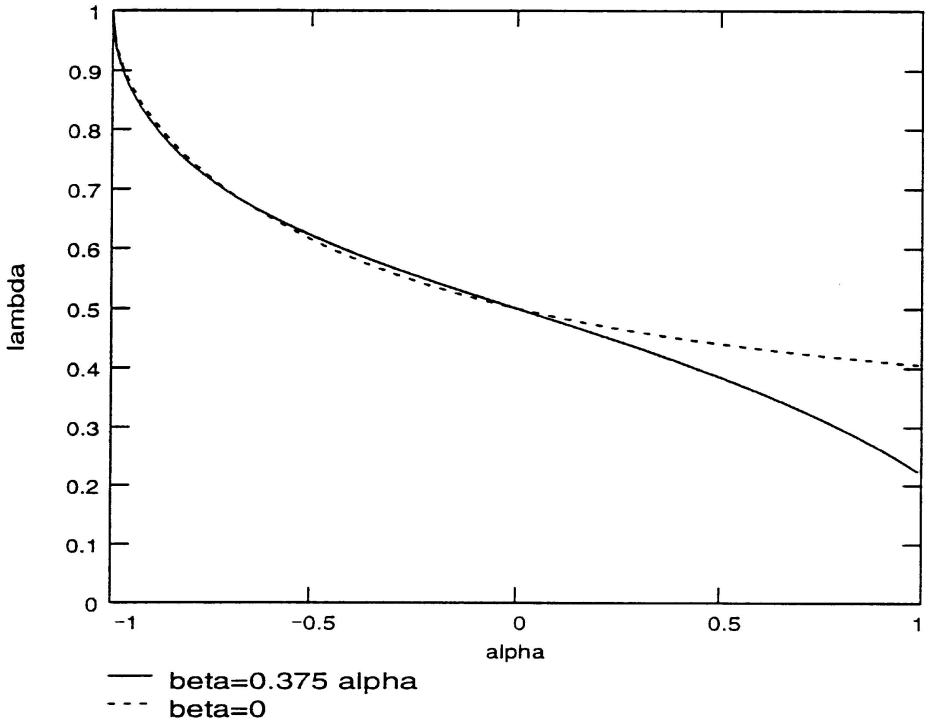

Figure 2.2: Stress singularity exponent λ versus α with two different β; β=0 (dotted line), β=0.375α (solid line).

case of β=0, and the solid line is for β=0.375α which is obtained by fixing ν_f and ν_m at 0.2 in Eq. (2.2b). Note that to fix β=0 needs certain combinations of ν_f and ν_m, and is hard to apply to realistic composites in which the properties are not variables once the composite constituents are chosen. Generally in Fig. 2.2, both curves show that for identical elastic properties λ=1/2, but for fibers stiffer than the matrix λ<1/2, while for matrix stiffer than the fibers λ>1/2. Furthermore, it is observed that the two curves in Fig. 2.2 are practically identical over negative α region, but show a large discrepancy in the high α range which is in fact the case for most CMCs.

Considering Eqs. (2.4) and (2.5) along with Fig. 2.2, we find that for large values of elastic ratio, α, the strength of the stress singularity diminishes considerably towards –0.2. This case corresponds to a crack propagating from a soft to a hard material. On the other hand, the strength of the stress singularity increases significantly for a very small α. Zak and Williams [11] showed that when a crack proceeds from a hard into a soft material, the maximum stress occurs along the interface and is almost an order of magnitude larger than the largest principal stress of the crack. On the contrary, when the crack propagates from a soft to hard material the maximum principal stress occurs ahead of the crack at non-zero angular position, ±70°. This implies the crack approaching the softer material is most likely arrested at the interface and deflected along the interface. It should be noted, however, that the detailed research on the competition between two cracking modes at the interface, i.e. crack deflection and crack penetration, was not performed in Zak and Williams.

2.1.2. Crack Deflection/Penetration at Interfaces

As a matrix crack reaches an interface, there are at least three possible crack paths for the crack. Figure 2.3 shows the simplest possible failure paths in an axisymmetric

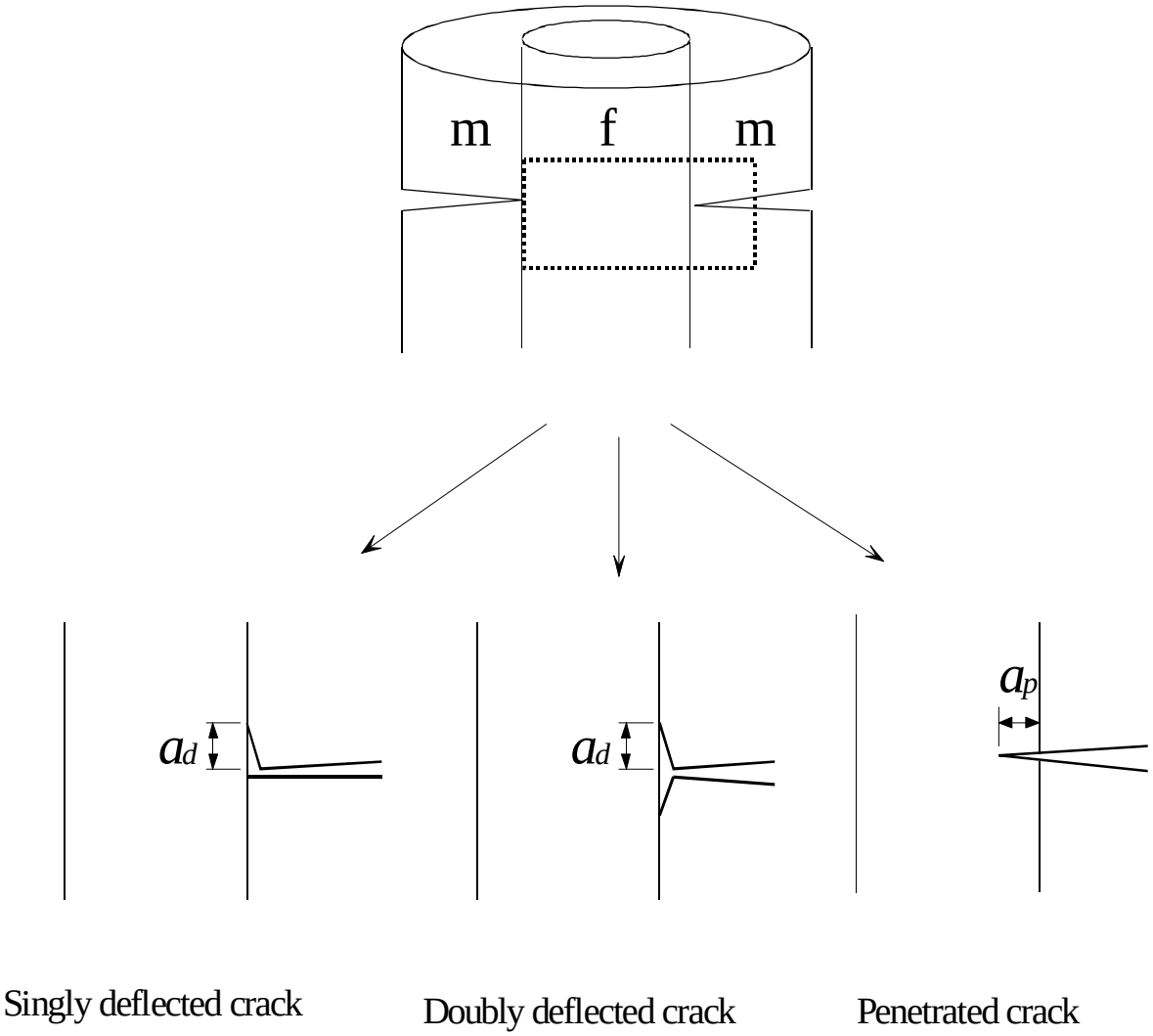

Figure 2.3: Three potential fracture modes at a fiber/matrix interface.

model composite: (1) crack deflection on one side of the interface (singly deflected crack); (2) crack deflection on both sides (doubly deflected crack); and (3) crack penetration across the interface. Here, a matrix crack perpendicularly approaching the interface is of interest. Which of these three paths the crack selects is the central issue of the present Chapter, and of much previous work. Stress criteria and energy criteria are typically used to determine the crack path; the former is governed by the local asymptotic stress field at the interface [15,16], while the latter is based on the differences of work of fracture along possible alternative crack paths [17,18,19].

Cook and Gordon [15] were the first to investigate the conditions for a crack to be deflected at an interface, from a stress perspective. They found that the stress acting perpendicular to the interface, σ_{yy}, is zero at the crack tip but rises to a sharp peak within a small distance from the crack tip and decreases, while the stress component opening an elliptical shape crack, σ_{xx}, reaches its maximum value at the crack tip and decreases monotonically with distance from the crack tip. The ratio of the peak value of σ_{yy} to σ_{xx} is 1/5 and from this it was understood that an interface with a theoretical tensile strength of less than 1/5 that of the matrix will debond ahead of the main crack allowing crack deflection to occur. When a crack tip is sharp, however, both σ_{xx} and σ_{yy} have the same high value at the crack tip and decrease with distance from the crack tip at the same rate. Thus, the criterion suggested by Cook and Gordon does not hold. For this case, Gupta *et al.* [16] proposed a deflection criterion as

$$\frac{\sigma_i^*}{\sigma_f^*} < \frac{\sigma_{yy}(0^\circ)}{\sigma_{xx}(90^\circ)} \tag{2.6}$$

where σ_i^* and σ_f^* are, respectively, the interface and fiber strength and $\sigma_{yy}(0°)$ and $\sigma_{xx}(90°)$ are, respectively, the stresses acting normal to the interface and in the fiber. It was predicted that the interface must have a strength less than about 35% that of the fiber to ensure the crack deflection in the case of no elastic mismatch (see Fig. 2 of Ref. [16]).

From the energy perspective, a crack will grow when the energy available in the stress field around it, which is relieved as the crack grows, is sufficient to make up for the loss in energy upon creation of the new crack surface. To predict crack growth thus requires an ability to calculate the strain energy release rate G, or elastic energy relieved per unit area of crack advance, and a knowledge of the underlying surface fracture energy Γ created as the crack grows. The recent development of effective techniques to measure the interface toughness has made it possible to use the energy criterion more easily while measuring the interface strength still remains difficult to perform [20]. Here, we denote by G_d and Γ_d the strain energy release rate and surface energy for the case of deflection, and by G_p and Γ_p the corresponding quantities for penetration. If $G_d \geq \Gamma_d$ the crack can deflect while if $G_p \geq \Gamma_p$ the crack can penetrate the fiber. It is not clear which path is selected if both conditions are satisfied, and in fact other fundamental problems related to the degree of crack extension arise for elastically-mismatched materials, as discussed briefly below.

For a crack perpendicular to the interface and under applied load parallel to the interface, the strain energy release rates as a function of crack extension a_d along the interface (deflection) and a_p into the fiber (penetration) are well-known to be of the forms [17,19]

$$G_d = d(\alpha,\beta)k_I^2 \pi a_d^{1-2\lambda} \; ; \qquad G_p = c(\alpha,\beta)k_I^2 \pi a_p^{1-2\lambda} \tag{2.7}$$

where d and c are complex functions of the Dundurs' parameters, and k_I is a Mode I stress-intensity-like factor as shown in Eq. (2.4). The above forms arise from the asymptotic near-tip field of the crack, and hence hold in the limit of a_d, $a_p \to 0$. The singularity exponent, λ, was discussed earlier with Fig. 2.2, and note again that for fibers stiffer than the matrix $\lambda < 1/2$, while for matrix stiffer than the fibers $\lambda > 1/2$. *Therefore, taking the limit of zero crack extension in either case of elastic mismatch leads from Eq. (2.7) to either (i) zero strain energy release rate ($\lambda < 1/2$) and hence no possible cracking*

or (ii) infinite strain energy release rate ($\lambda>1/2$) and hence cracking at any finite stress level.

To overcome the basic difficulties evident from the above results, He and Hutchinson (HH) proposed a nice concept that led to an analytic and finite result for assessing deflection versus penetration [17]. HH proposed to consider the ratio G_d/G_p with $a_d=a_p$, in which case the crack extension length drops out of the problem. Furthermore, HH proposed that crack deflection would occur if $G_d/G_p > \Gamma_d/\Gamma_p$. For a penetrating crack at the fiber surface, $\Gamma_p=\Gamma_f$ where Γ_f is the critical strain energy release rate or surface energy of the fiber, and for a deflecting crack at the interface, $\Gamma_d=\Gamma_i$ where Γ_i is the surface energy of the interface. Hence, the deflection criterion at the fiber/matrix interface is

$$G_d/G_p < \Gamma_i/\Gamma_f \quad . \tag{2.8}$$

This criterion was then studied in considerable detail by He and Hutchinson under certain conditions. They studied a planar interface under plain strain and traction boundary conditions, with isotropic "matrix" and "fiber". Their analysis implicitly assumed that the crack size in the "matrix" is semi-infinite and, as noted above, the crack extensions are considered infinitesimal. The special case of β=0 was studied, although very limited results suggested that the deflection criterion was only weakly affected by the value of β relative to its dependence on α. Singly and doubly deflected interface cracks were considered within the limitations of plane strain. HH also considered cracks approaching the interface at oblique angles.

Gupta *et al.* [16] extended He and Hutchinson's work [17] to the area of anisotropic materials for the case of a crack approaching perpendicular to the interface. They also derived a strength criterion for crack deflection as shown earlier in this Section, and confirmed their analysis by using laser spallation experiment. Gupta *et al.* concluded that it is impossible to provide generalized delamination charts as a function of α alone. Instead, they have tabulated the required values of the interface strength and fracture

toughness for delamination in a number of composite materials. A later work by Martinez and Gupta (MG) [18] showed that, compared to the strength criterion, the energy-based criterion is more sensitive to the material anisotropy. Furthermore, MG have corrected one of the important results in the previous work by HH. In contrast to He and Hutchinson's results, their calculations show that the G_d/G_p for the doubly deflected crack is higher than G_d/G_p for singly deflected crack when Dundurs' parameter α is larger than zero. That is, the doubly deflected crack is the dominating crack mode. Martinez and Gupta also examined the effect of anisotropy on the crack deflection by manipulating the anisotropy-related parameters including the other Dundurs' parameter, β. They showed that β=0 assumption may overestimate the G_d/G_p vs. α behavior by 20-25% over the range β=-0.2~0.2.

Following the work of Martinez and Gupta, He, Evans and Hutchinson (HEH) [19] provided a corrected result for the ratio G_d/G_p for the doubly deflected crack. More importantly, HEH investigated the influence of the residual stresses on the competition between interface cracking and substrate cracking. Their result showed that thermal expansion misfit can be significant in systems with planar interfaces such as layered materials and thin film structures, but in fiber-reinforced composites the effect of misfit is expected to be minimal because of the coupling between axial and radial residual stresses. Of some importance and relevance to the present work, HEH demonstrated that when residual stresses are present, the ratio of G_d/G_p is always dependent on a_d and a_p; the convenient cancellation obtained in the absence of residual stresses does not occur. Thus, the deflection criterion is an explicit function of both a_d and a_p. In the present work we show that, for realistic volume fractions and small to moderate crack extensions, the ratio G_d/G_p depends on the crack extension even in the absence of residual stresses. Furthermore, these finite length effects are probably larger than the effects obtained from realistic residual stress levels obtainable in ceramic composites, particularly for the axisymmetric geometry. In HEH, the ratios of G_d/G_p with various residual stress parameters asymptotically approach the non-thermal stress case at reasonable fiber volume fractions (see Fig. 9 in HEH for details). We will show here, however, that the

effect of various crack extension lengths make significant discrepancies in G_d/G_p especially at high α, which was not accounted for in HEH.

In this study, we adopt the HH deflection criterion based on energy and a ratio of strain energy release rates (see Eq. (2.8)). We then investigate, using a numerical technique developed by Pagano that employs Reissner's variational principle, the dependence of the deflection criterion on crack extension lengths a_d and a_p and on fiber volume fraction V_f for an axisymmetric fiber/matrix interface geometry. We restrict the problem to a perpendicular matrix crack impinging onto the interface, and to the doubly-deflected crack case shown previously to be the dominant fracture mode. In the limits of small a_d, a_p and small V_f accessible numerically, we reproduce the corrected HH results (or HEH results), which also validates the use of the relatively new numerical technique. We then demonstrate the insensitivity of the deflection criterion on β. At finite a_d, a_p and V_f, we find that the ratio of G_d/G_p *decreases* well below the HH limit for $\alpha>0$, implying that deflection is more difficult than previously anticipated in this regime. We also compare various predictions of deflection and penetration to experimental results on model composites with well-established constitutive properties. Finally, presentation of the effect of different crack extensions in both cracks on the criterion is followed by the problem of the pre-existing crack-like flaws along the interface and/or in the fibers. This modeling effort is based on the recognition that the length scales of crack extensions could be different in deflection and penetration, and controlled by characteristic structural defects at large scales such as misfit dislocation and grain boundary orientation.

The remainder of this Chapter is organized as follows. In Section 2.2, we introduce the details of Pagano's Axisymmetric Damage Model with a basic concept of Reissner's variational principal. In Section 2.3, we define the specific problem to be solved. Section 2.4 contains detailed results on deflection versus penetration. Comparison of the various deflection criteria with new experimental data is also presented. In Section 2.5, we summarize and discuss directions for future work.

2.2. Axisymmetric Damage Model

2.2.1. Introduction

In order to solve classical mechanics problems, we normally adopt two different ways; one path is vectorial mechanics based on Newton's laws, another path is the principal of virtual work which was formulated by Bernoulli, and developed as a mathematical tool by Lagrange in the eighteenth century [21]. The principle of stationary potential energy by Lagrange is well adapted to elasticity problems that are formulated in terms of displacements while Castigliano's theorem of least work is adapted to problems that are formulated in terms of stresses. In the middle of twentieth century, a variational theorem which simultaneously provides the stress-displacement relations, the equilibrium equations, and the boundary conditions of linear elasticity was developed by Reissner [22], and it became possible for the variational theorem to be effectively used to solve the boundary value problems with mixed boundary conditions of stresses and displacements. Reissner showed that the governing equations and boundary conditions of linear elasticity could be derived as a result of minimizing the following functional with respect to both stress and displacements.

$$J = \int_V F dV - \int_{S'} T_i \xi_i dS \tag{2.9}$$

where

$$F = \frac{1}{2}\sigma_{ij}(\xi_{i,j} + \xi_{j,i}) - W \quad . \tag{2.10}$$

In these equations, T_i is the prescribed traction, and σ_{ij} and ξ_i are the stress and displacement components, respectively, in Cartesian coordinates. A comma after a subscript represents a derivative with respect to the indicated coordinate, and Einstein's summation convention is understood. V is an arbitrary volume enclosed by the entire surface S, while S' is the portion of the boundary on which one or more traction

components are prescribed. The body forces have been neglected in the formulation, and W is the complementary energy density given by

$$W = \frac{1}{2} S_{ij} \sigma_i \sigma_j + \sigma_i e_i \tag{2.11}$$

where S_{ij} is the compliance matrix and e_i represent the hygrothermal free-expansion (non-mechanical) strain components.

Pagano applied Reissner's theorem to various types of problems including the stress analysis in the composite plate [23] and in the involute bodies of revolution [24]. Note that in the original paper by Reissner, transverse bending of plates was analyzed as an application example. In a later work, Pagano [25] modified Reissner's theorem for the widely-used concentric cylindrical composite model in which damage modes include fiber breaks, annular cracks in the coatings or matrix, and debond cracks at the interface, with the boundary conditions being either applied stresses or displacements (see Fig. 2.4). Based on the new variational theorem, the Axisymmetric Damage Model (ADM) was developed to predict the stress and displacement distributions in composite constituents as well as the strain energy and energy release rates for cracked composites.

In the ADM, concentric cylindrical/annular elements are used to model the representative volume element (RVE) where the innermost cylinder may be a fiber, the next ring can be considered as coating or interphase region while the outermost ring can represent matrix material. Additional concentric annuli (radii r_1, r_2, …) can be introduced, as well as longitudinal sections (z_1, z_2, …), if necessary for computational purpose. This discretization forms regions bounded by r_i and r_{i+1} and sections z_j and z_{j+1}. The annuli, or layers, and sections are chosen so that cracks introduced into the geometry always lie along the boundaries of sections (for transverse cracks) or annuli (for longitudinal cracks) and span one or more complete sections/layers. The cracks then simply define a particular boundary condition along the surface of any region. The elasticity problem

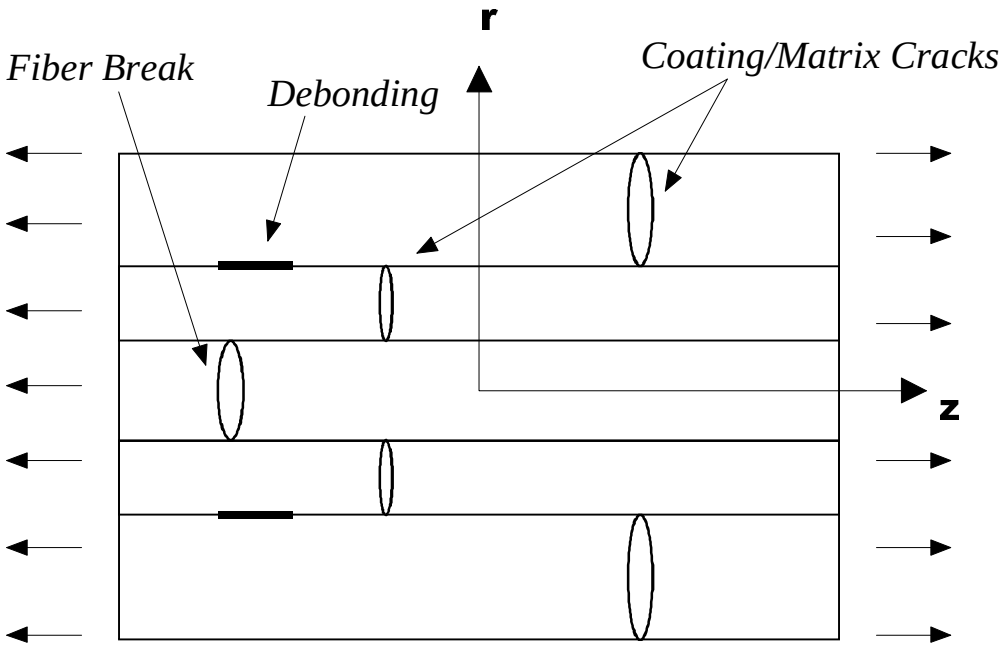

Figure 2.4: Typical damage modes in a unidirectional fiber-reinforced composite.

within each region subject to appropriate boundary conditions is solved using Reissner's variational equation. At the coarsest level, regions can be chosen to fully span existing cracks and interfaces. However, as mentioned above, in order to improve the accuracy of the solution for the stress fields and energy release rates, it is possible to introduce additional annular layers in the neighborhood of interfaces, crack tips, and the other forms of stress concentrations. Although similar to mesh refinement in finite element analysis, the refinement here is primarily only in the radial coordinate; refinement in the axial coordinate is only necessary for computational tractability in the solution and not for accuracy.

The validation of the accuracy of the ADM model in the calculation of stress fields and energy release rates is given by Pagano and his colleagues [25-27] for several different problems. In his work on the axisymmetric micromechanical stress fields in composites [25], Pagano used a simple microcomposite which consists of an isotropic fiber surrounded by isotropic matrix with traction-free boundary condition under a uniform temperature change, and examined the microstresses in the composite. The results show good agreement with an existing elasticity solution. The accuracy has also been confirmed for the energy release rates of an interfacial debond crack by comparison to elasticity solutions by Kasano *et al.* [28,29]. Pagano and Brown [26] developed a "full-cell cracking model" and considered the issues associated with predicting the initiation of matrix cracking within a unidirectional brittle matrix composite. The stress analysis in the constituents as well as at the interface was performed to predict the stress field and energy release rates. The work includes a study of crack deflection at the interface using the energy release rates, and comments are made regarding the perceived need for poor bonding in these materials. Recently, Pagano [30,31] has summarized his recent works on the micromechanical failure modes in the ideal brittle matrix composites, which covers the damage of uncoated-fiber composites and coated-fiber composites under axial tension loading. Numerical and experimental results to support the viability of the ADM model are provided.

While the ADM has been shown to provide accurate representations of micromechanical stress fields and energy release rates, it cannot be ignored that the model was designed to analyze the elastic composites. The model is equally applicable to polymer or metal matrix composites, provided the constituents are in the elastic range, even if damage is present. Other main limitations are that the form of micromechanical damage is axisymmetric and the cracks are either in the axial direction or radial direction; oblique cracks are not allowed. However, we often observe manifestation of fracture mode that has axisymmetric appearance and the importance of oblique cracks has not been established, and thus the assumptions are believed to be reasonable approximations [30].

2.2.2. Solution Development

In the ADM, the stress field in each annular region is assumed to be one where σ_θ and σ_z are linear in the radial coordinate r, while the forms of σ_r and τ_{rz} are chosen to satisfy the axisymmetric equilibrium equations. Then, all of the stress components depend on r through known shape functions as discussed below.

We begin by considering an arbitrary region, say the k^{th} region where k=0,1,…,N, within the body defined by the inner and outer radii $r_1(z)$ and $r_2(z)$ with the planes at z_1 and z_2 (see Fig. 2.5). Assuming torsionless axisymmetric traction and/or displacement boundary conditions on the outermost cylinder surface as well as on the end planes so that $\tau_{r\theta}$ and $\tau_{z\theta}$ vanish, we deal with only four stress components. Letting σ_1, σ_2, σ_3, σ_5 represent σ_z, σ_θ, σ_r, τ_{rz}, respectively, we assume the form of the stress components within the region $r_1<r<r_2$,

$$\sigma_i = p_{iJ} f_J^{(i)}, \; i=1,2,3,5; \; J=1,2,\ldots 5 \tag{2.12}$$

where the stress-related functions p_{iJ} are the functions of z only and $f_J^{(i)}$ are known shape functions of r defined by

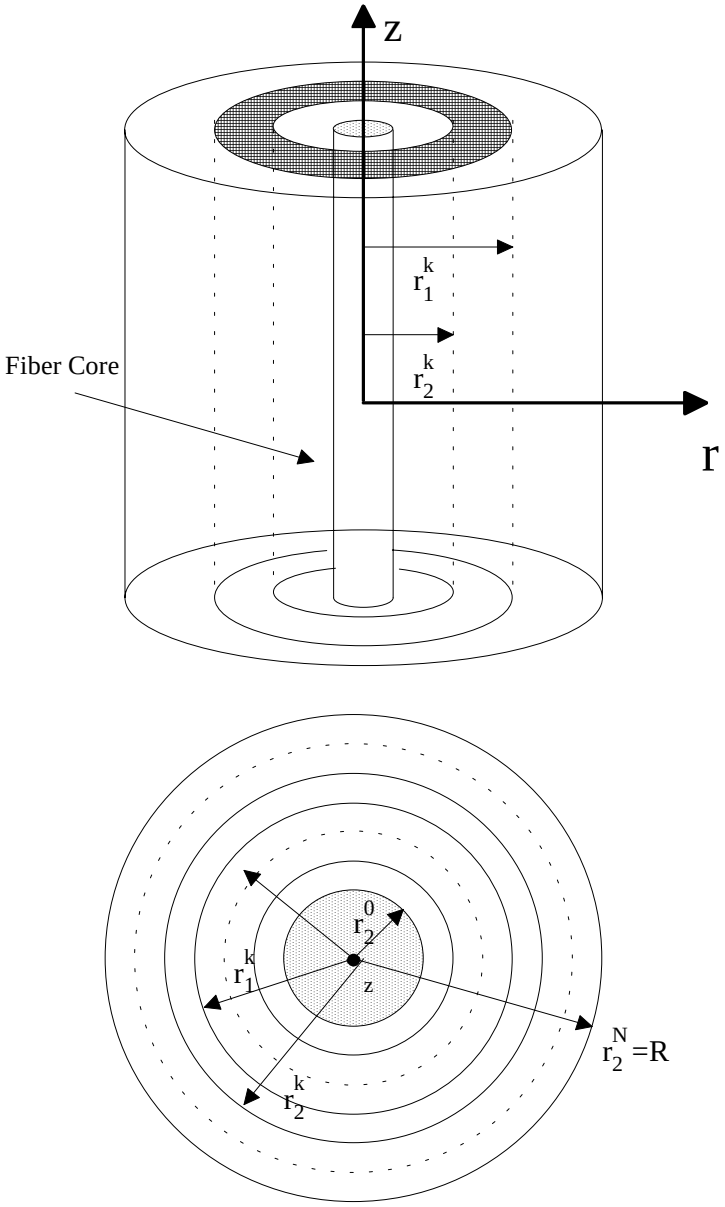

Figure 2.5: Axisymmetric element showing a typical layer.

$$f_1^{(1)} = f_1^{(2)} = f_1^{(3)} = \frac{r_2 - r}{r_2 - r_1}$$

$$f_2^{(1)} = f_2^{(2)} = f_2^{(3)} = \frac{r - r_1}{r_2 - r_1}$$

$$f_1^{(5)} = \frac{r}{r_2} f_1^{(1)}, \; f_2^{(5)} = \frac{r}{r_2} f_2^{(1)}$$

$$f_3^{(3)} = r^3 - (r_1^2 + r_1 r_2 + r_2^2) r + r_1 r_2 (r_1 + r_2) \qquad (r_1 \neq 0) \qquad (2.13)$$

$$f_4^{(3)} = r^2 - (r_1 + r_2) r + r_1 r_2$$

$$f_5^{(3)} = \frac{1}{r_1 r_2 r} f_4^{(3)}$$

$$f_3^{(5)} = \frac{(r_1 + r_2) r^2 - (r_1^2 + r_1 r_2 + r_2^2) r}{r_1^2 r_2^2} + \frac{1}{r}$$

with

$$p_{iJ} = f_J^{(i)} = 0 \quad (r_1 \neq 0;\ i=1,2 \text{ and } J=3,4,5 \text{ or } i=5 \text{ and } J=4,5) \quad . \qquad (2.14)$$

For $r_1 = 0$ (innermost cylinder region), instead of Eq. (2.13), we have

$$f_1^{(1)} = f_1^{(2)} = f_1^{(3)} = \frac{r_2 - r}{r_2}$$

$$f_2^{(1)} = f_2^{(2)} = f_2^{(3)} = f_2^{(5)} = \frac{r}{r_2} \qquad (r_1 = 0) \qquad (2.15)$$

$$f_3^{(3)} = (r^2 - r_2^2) r$$

$$f_4^{(3)} = f_3^{(5)} = (r - r_2) r$$

with

$$p_{iJ} = f_J^{(i)} = 0 \quad (r_1 = 0;\ i=1,2 \text{ and } J=3,4 \text{ or } i=5 \text{ and } J=1,4 \text{ or } J=5) \quad . \qquad (2.16)$$

Note that the relations in Eqs. (2.13) – (2.16) arise by assuming that σ_1 and σ_2 are linear functions of r in the region and determining the form of the remaining stress components from the equations of equilibrium of axisymmetric elasticity subjected to the following conditions such that the p functions are equal to the actual stresses at $r=r_1, r_2$.

$$p_{i\alpha}(z)=\sigma_i(r_\alpha,z)\ ,\ \ i=1,2,3,5;\ \ \alpha=1,2 \quad . \tag{2.17}$$

In the subsequent derivation of the governing equations, the integrations will give rise to the remaining dependent variables, the so-called "weighted displacements", without further assumptions. They are

$$(\bar{u},\hat{u},\breve{u},\widehat{u})=\int_{r_1}^{r_2} u(1,r,r^2,r^3)dr \qquad ; \qquad (\hat{w},\breve{w})=\int_{r_1}^{r_2} w(r,r^2)dr \tag{2.18}$$

where u is the radial displacement and w is the axial displacement. The interfacial displacements u_α, w_α (α=1,2), or displacements on the radial boundaries $r=r_1, r_2$, enter the formulation only if they are prescribed, thus they are not treated as dependent variables.

We now substitute Eqs. (2.10) – (2.18) into Eq. (2.9) and use the Leibnitz theorem to give the final form of δJ for each region. Specifically, we perform the integration with respect to r after taking the first variation and obtain $\delta J/2\pi$ given by

$$\begin{aligned}\frac{\delta J_k}{2\pi}=\int_{z_1}^{z_2}\Big[&(\mu_{iJ}+\chi_{iJ})\delta p_{iJ}+r_2(p_{32}\delta u_2+p_{52}\delta w_2)-r_1(p_{32}\delta u_1+p_{51}\delta w_1)\\ &-r_1(p_{32}\delta u_1+p_{51}\delta w_1)-(F_1\delta\bar{u}+F_2\delta\hat{u}+F_3\delta\breve{u}+F_4\delta\widehat{u}+F_7\delta\hat{w}+F_8\delta\breve{w})\Big]^k dz\\ &+\Big[(H_1\delta\bar{u}+H_3\delta\breve{u}+H_4\delta\widehat{u}+H_7\delta\hat{w}+H_8\delta\breve{w})^k\Big]_{z=z_1}^{z=z_2}-\int_{L_k'}(\tilde{T}_r\delta u+\tilde{T}_z\delta w)rdL_k \quad .\end{aligned} \tag{2.19}$$

The detailed expressions for μ_{iJ}, χ_{iJ}, F and H are given in the Appendix A.

Now, Eq. (2.19) may be used to determine δJ of the entire medium. Since we need to solve the variational equation in each one of the annular regions, the following conditions must be then satisfied

$$\delta J = \sum_{k=0}^{N} \delta J_k = 0 \quad . \tag{2.20}$$

In order to satisfy Eq. (2.20), the integrand of the first integral in Eq. (2.19) must vanish for $z_1 < z < z_2$. Since the variations of the weighted displacements, $\delta\overline{u}_k \ldots \delta\breve{w}_k$, are all arbitrary in this region, we may immediately write the following field equations,

$$F_1^k = F_2^k = F_3^k = F_4^k = F_7^k = F_8^k = 0 \qquad (k = 0,1,\ldots, N) \ . \tag{2.21}$$

Aside from $\delta p_{31}^k, \delta p_{32}^k, \delta p_{51}^k, \delta p_{52}^k$ which may enter the boundary conditions and/or interface conditions, the remaining δp_{iJ}^k are arbitrary in $z_1 < z < z_2$. Therefore, we get

$$\chi_{11}^k = \chi_{12}^k = \chi_{21}^k = \chi_{22}^k = \chi_{33}^k = \chi_{34}^k = \chi_{53}^k = 0 \qquad (k = 0,1,\ldots, N) \tag{2.22}$$

as well as

$$\chi_{35}^k = 0 \qquad\qquad (k = 1,2,...\mathrm{N}) \quad , \tag{2.23}$$

and

$$\chi_{31}^0 = 0 \quad . \tag{2.24}$$

Equations (2.21) are the equilibrium equations and Eqs. (2.22) - (2.24) represent the constitutive relations.

2.2.3. Boundary Conditions

Regarding boundary conditions, the Reissner's variational principle can handle mixed boundary problems so that both displacements and stresses can be specified. However, note that arbitrary variation of stresses along the radial boundary is not allowed. In general, the stresses are defined by specifying their values at two locations, the end points of the layer, and for the case of τ_{rz} at a third intermediate location. General boundary conditions, for an axisymmetric model composite consisting of a fiber and matrix, are discussed below. The fiber/matrix interface may be imperfect due to an intrinsic flaw or a deflected crack, and in this case a "debond zone" (or slip zone) is defined. Figure 2.5, Figure 2.6 and Figure 3.1 of the next Chapter may be helpful to understand the following explanation.

Recall that since the ADM is for an axisymmetric RVE, no θ-related variation appears. Furthermore, enforcing the same boundary conditions at both ends of the model composite results in two planes of symmetry; along r=0 (z-axis) and along z=0 (r-axis) where the intersection of the axes, or the origin of the cylindrical coordinate, is located at the center of the axisymmetric RVE. Therefore, we practically have the representative element defined by two end planes (z=0 and z=L) and two annuli (r=r_1^0=0 and r=r_2^N=r_m). Along the r=0 symmetry plane the radial displacement and shear stress vanish (u=τ_{rz}=0), and along the z=0 plane the axial displacement and shear stress should be zero (w=τ_{rz}=0).

On the outer surface of the composite (r=r_m), there are two possible boundary conditions: (i) traction-free boundary conditions (σ_{rr}=τ_{rz}=0); or (ii) zero shear stress and nonzero constant radial displacement (τ_{rz}=0 and u=const.). In this study we use the former boundary conditions for simplicity, but we also consider the latter boundary conditions on a limited basis, for illustrative purposes. To obtain the proper displacement boundary conditions, we proceed as follows: (i) assume a crack-free uniaxially tensile loaded composite with perfectly bonded interface and a stress-free outer surface boundary;

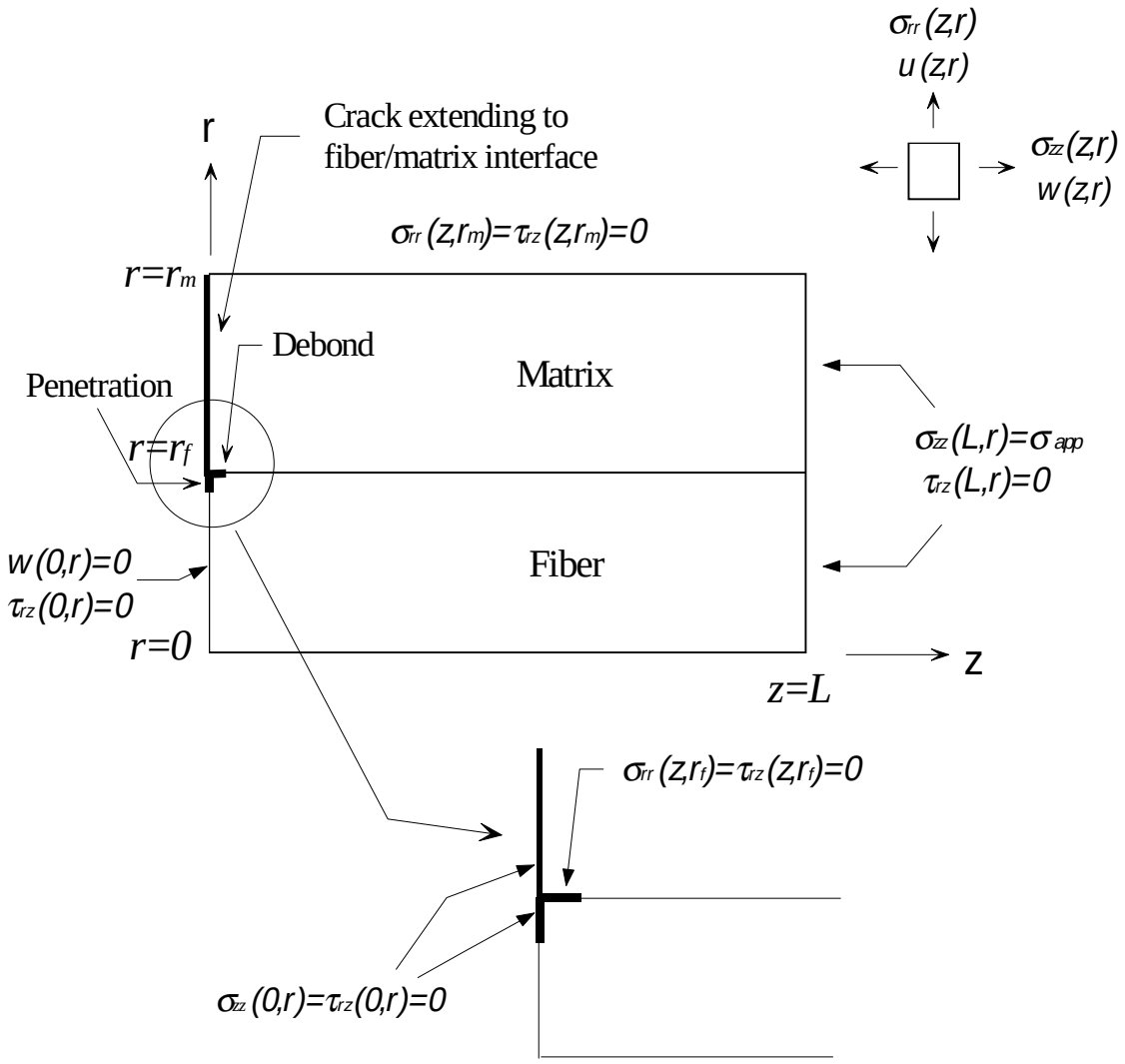

Figure 2.6: Debond and penetration at fiber/matrix interface in axisymmetric geometry.

(ii) obtain the constant radial displacement perpendicular to the cylinder outer surface in the composite using the ADM; (iii) use the radial displacement as a boundary condition in a matrix-cracked composite with an imperfect interface. The difference in strain energy release rates from the two boundary conditions will be discussed in Section 2.4.

If there is a cracked-boundary, the aforementioned traction-free boundary conditions may be applied on the crack surface. Otherwise, a constant or linearly-varying stress component can be used to model a pressurized crack. Along the fiber/matrix interface, there are some boundary conditions which should be satisfied at all times. The radial stresses and the shear stresses in neighboring constituents are continuous. In addition, in the debond slip region at the interface the radial displacements should be continuous, while in the elastic zone (stick zone or perfectly bonded zone) both of the radial and the axial displacements are continuous. However, applying the proper boundary conditions at the locations near the matrix crack or debond crack tip is not simple because of the stress and displacement singularities. Here, we simply note that if a debond crack takes place at an interface, one may choose between maintaining continuity of the shear stress or of a certain weighted displacement at the crack tip. Selecting shear stress continuity has been shown to lead to energy consistency, and this condition is used throughout this study.

2.2.4. ADM Code

From the general solution presented above with appropriate boundary/continuity conditions across element boundaries, we can obtain a set of algebraic equations and linear ordinary differential equations in z only for the unknown coefficients of the stress fields. For a body composed of a core cylinder and N annuli, there are $18N+16$ equations to solve [25,30]. Since the field equations within each cylinder reduce to a system of algebraic equations and linear ordinary differential equations with constant coefficients, the general form of the solution for any of the dependent variables $F(z)$ is expressed by

$$F(z) = \sum_i A_i e^{\lambda_i z} + F_p(z) \tag{2.25}$$

within each cylinder, where A_i are constants, λ_i are eigenvalues of a determinant, and $F_p(z)$ is a particular solution which is taken to be a simple polynomial. The ADM code was developed to solve these series of equations.

The computed eigenvalues, eigenvectors and homogeneous and particular solutions for each unique region are substituted back into the original system of equations to verify the calculated values. If any equation is not satisfied identically, it is listed in the file "axisym.eig". The file "axisym.bcs" contains the tractions and displacements, calculated by ADM, at the external boundary locations. This file thus helps to verify the prescribed external boundary conditions for the problem being solved. File "axisym.debug" gives a listing of all the dependent variables for all layers in the model evaluated at the left end, center, and at the right end of each section. The information contained in this file can be used to examine all the boundary conditions for the problem including interface conditions between layers and sections [32].

2.3. Problem Description: Fiber/Matrix Interface Model

In order to predict the crack path at the fiber/matrix interface, an axisymmetric microcomposite consisting of isotropic, elastic fiber and matrix is considered. Fig.2.6 shows the fiber/matrix interface model with the appropriate boundary conditions. The main matrix crack lies in a plane perpendicular to the fiber and extending to the interface, where it may subsequently deflect along the interface or penetrate into the fiber. Strain energy release rates for deflection (G_d) and penetration (G_p) are calculated and the ratio of G_d/G_p as a function of Dundurs' parameters α and β is determined.

Formally, the strain energy release rate is composed of the difference in potential energy and the work done by the applied forces at the boundaries of the body per unit area, when the crack is advanced. However, since the work done by the applied forces is twice the elastic potential energy change in linear elastic materials, one thus obtains the strain energy as the negative of the potential energy by subtracting the work from the potential energy. In this study, we are mainly interested in the ratios of strain energy releases for a deflected crack and a penetrating crack, which must be the same as the ratios of potential energies. Hence, the potential energies we directly obtain from the ADM model can be used for strain energy release calculations as discussed below.

To obtain strain energy release rates requires three calculations. First, with only the initial matrix crack, we calculate the elastic potential energy in the system at a fixed remote applied load. This gives the initial reference potential energy W_r. Second, we advance the crack into the fiber by an amount a_p and calculate the potential energy for this longer, penetrated crack, W_p. Third, we advance the initial crack at a right angle along the interface by an equal amount a_d to form the incipient deflected crack, and calculate the potential energy for the deflected crack, W_d. The strain energy release rates are then calculated from the energy differences and the area of crack growth as

$$G_p = (W_p - W_r) \Big/ (\pi r_f^{\,2} - \pi (r_f - a_p)^2) \quad ; \quad G_d = (W_d - W_r) \Big/ (2\pi r_f a_d) \tag{2.26}$$

where r_f is the fiber radius. Note that G_d and G_p are total energy release rates and do not recognize the "mode mix". The dependence of G_d/G_p versus α and β is then used as the deflection criterion with $a_d=a_p$. The crack extension is taken to be $0.002r_f$, $0.01r_f$ and $0.025r_f$. To investigate the effect of different crack extensions in two types of cracks, we also fix a_p at $0.01r_f$ and adopt various a_d of $0.025r_f$, $0.01r_f$ and $0.002r_f$. We use a 1% fiber volume fraction to approach the semi-infinite matrix crack limit, and a 40% volume fraction to model a realistic composite. For the pre-existing crack problem, we calculate G_d/G_p in a composite having two small branch cracks from the main matrix crack (one

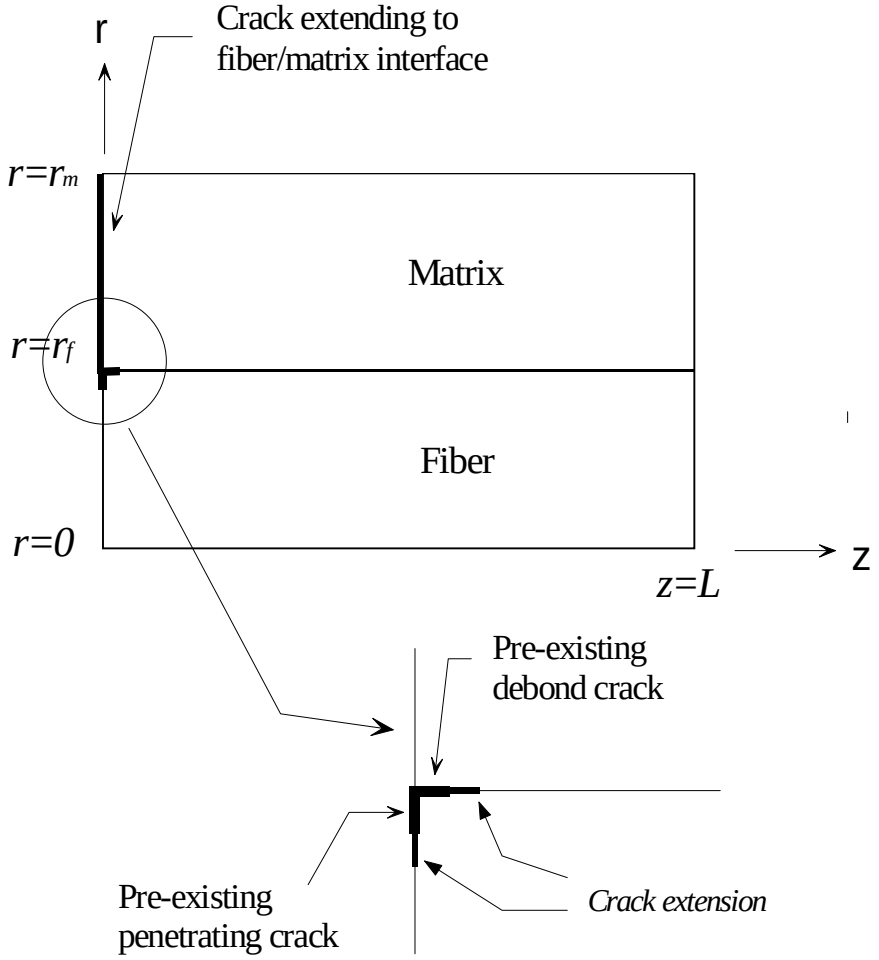

Figure 2.7: Pre-existing debond/penetrating cracks and crack extensions.

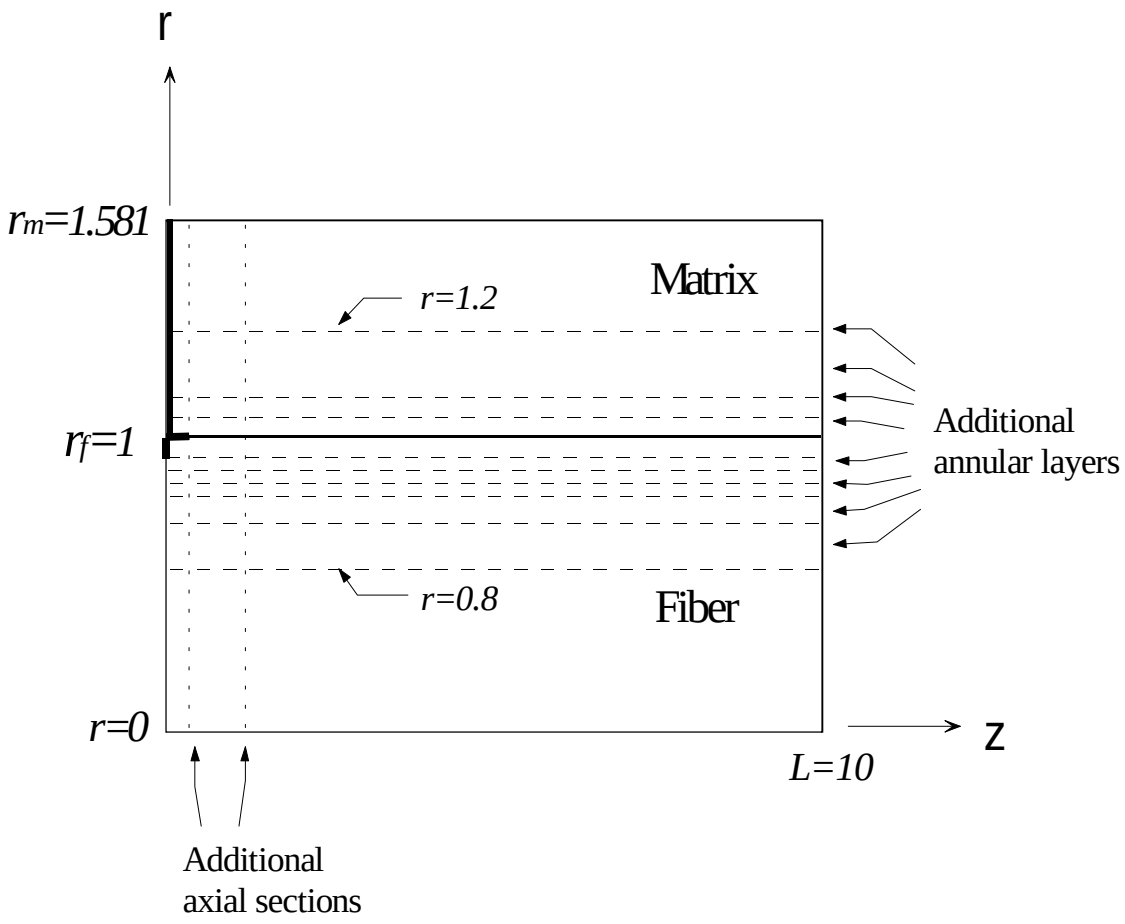

Figure 2.8: General mesh structure used in the ADM model.

deflected crack and one penetration crack) with the same sizes of $0.025r_f$, $0.01r_f$ and $0.002r_f$ (see Fig. 2.7).

As discussed in the previous Section, the accuracy of the ADM calculation depends on the number and the location of the boundaries of these elements. We show in Fig. 2.8 the general mesh structure used for the three calculations of matrix crack only, penetrated crack, and deflected crack, which we performed to determine the various strain energy release rates. Fig. 2.8 represents a model composite with a 40% fiber volume fraction and a length of $L=10r_f$. A schematic of the additional layers and sections used for the $a_d=a_p=0.002r_f$ case is illustrated. In addition to the physical material boundary at $r/r_f=1$, we employ 10 additional annular layers at $r/r_f=0.8$, 0.9, 0.93, 0.96, 0.99, 0.998, 1.03, 1.07, 1.1 and 1.2.

2.4. Results

2.4.1. Crack Deflection/Penetration

To validate our numerical solutions, we first investigate the small V_f, small $a_d=a_p$ limit and compare our results to the well-known analytical solution given by He and Hutchinson [17]. Since the original work by He and Hutchinson (HH) has been corrected by Martinez and Gupta (MG) [18] and He, Evans and Hutchinson (HEH) [19], we compare to the result from HEH. Figure 2.9 shows our results for the strain energy release rate ratio, G_d/G_p, as a function of Dundurs' elastic mismatch parameter α along with the HEH result. In our calculations, we have fixed the fiber and matrix Poisson's ratios at 0.2, and hence $\beta=0.375\alpha$, rather than fixing $\beta=0$ as in HH; we will discuss the effects of β below. To simulate semi-infinite crack size, or equivalently zero fiber volume fraction, and the infinitesimal crack extension which are assumed in HEH, the results in Fig. 2.9 correspond to V_f =1% and $a_d=a_p=a=0.002r_f$. The latter is the smallest value permitted by the current ADM code. The agreement between our calculations and

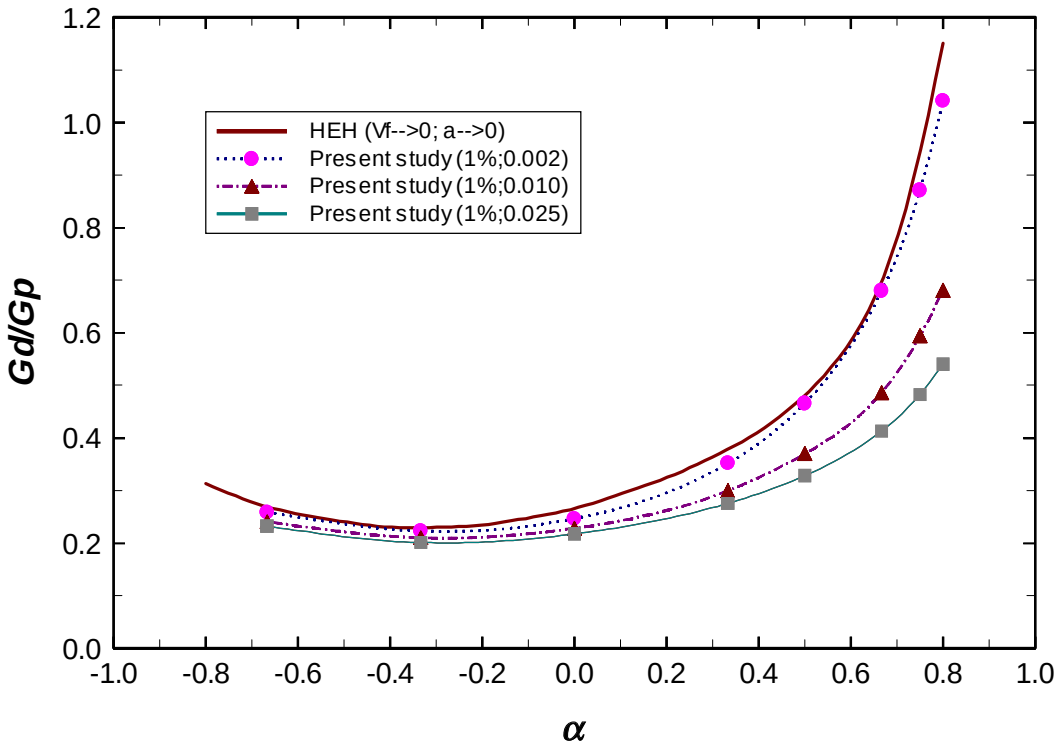

Figure 2.9: G_d/G_p versus α with various crack extensions for V_f=1%.

the HEH analytic result is excellent over the full range of α. This validates the use of the ADM code for this particular problem, and also shows the equivalence of the plane-strain/planar-interface and the axisymmetric versions of this problem.

Figure 2.9 also shows G_d/G_p vs. α for V_f=1% but for increased values of the crack extension $a_d=a_p=a$. For modest increases in the crack extension, G_d/G_p drops substantially at higher α. At α=0.8 and $a=0.025r_f$, G_d/G_p is only about 50% of the value at $a=0.002r_f$. This result explicitly demonstrates the sensitivity of the deflection criterion to the presumed crack extension, and moreover indicates that deflection is, in general, more difficult than predicted by the HEH criterion.

Figure 2.10 shows results for G_d/G_p at V_f=40% and finite crack extensions $a_d=a_p=a$ as used in Fig. 2.9. Here, even at the smallest crack extension of $0.002r_f$ there is a reasonable difference (45% at α=0.8) when compared with the very low volume fraction result and again the ratio of G_d/G_p decreases relative to the HEH result. For larger crack extensions, G_d/G_p decreases even further. At α=0.8, G_d/G_p for $a=0.025r_f$ is only 19% of HEH result and 35% of the result for $a=0.002r_f$. In fact, for the larger crack extensions the ratio is nearly constant over a wide range of α. While we expect that in the limit of $a\rightarrow 0$ the ratio G_d/G_p would eventually increase up to the HEH result, the crack extension must be much smaller than $0.002r_f$. In Fig. 2.10, the results using the displacement boundary condition are shown to compare the results using the traction-free boundary condition (see Section 2.2.3), and the difference by the two boundary conditions appears negligible. Regarding the loading conditions, far-field stress in the axial direction is applied at the end of the composite ($z=L$), but equivalent results for G_d/G_p are obtained using a pressure load on the matrix crack surface.

At this point, it is relevant to point out that the minimum crack extension of $0.002r_f$ used here can be physically quite small. For the largest commonly used fibers, Textron SCS-6 SiC fibers, the radius is $r_f=70\mu m$ and our minimum crack extension is $0.14\mu m$. Fibers more typically used in most CMCs with commercial potential have a much smaller

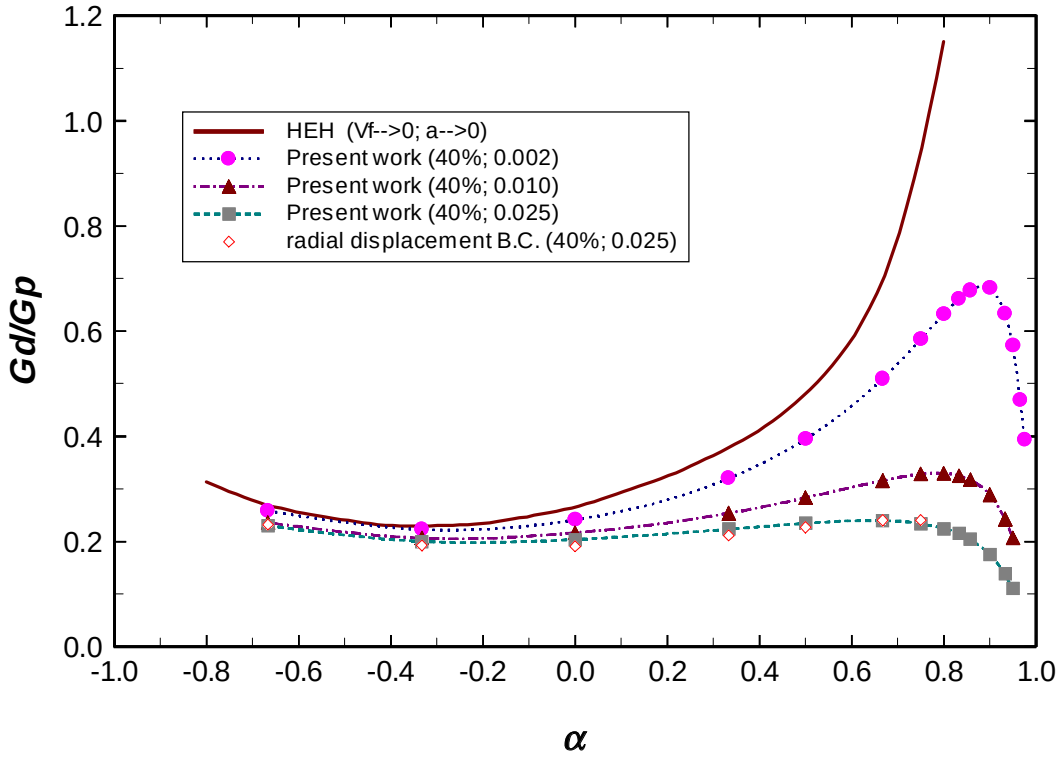

Figure 2.10: G_d/G_p versus α with various crack extensions for V_f=40%.

diameter. The widely-used Nicalon SiC fiber has a radius of about 7.5μm so that our minimum crack extension is 0.015μm or 15nm. Nextel Alumina fibers are slightly smaller still, and many graphite fibers have radii around 3.5μm. The crack extensions used here are thus approaching the atomic scale. Furthermore, the minimum crack extensions used here are certainly much smaller than the typical flaw sizes in the fibers. Flaws in the interface are not expected to be much smaller. Thus, if the crack extension a is interpreted as a flaw size in the fiber or interface to which the matrix crack can connect and propagate, then the range of a used in this study (a= 0.002r_f ~ 0.025r_f) is well within the range of flaws in typical CMC systems. For example, the average surface flaw size measured from the fracture surfaces of the SCS-0 fibers by Gambone [33] was 1.06 μm which results in an a of 0.0158r_f . Since in many CMCs, the range of elastic mismatch α lies between +0.3 ~ +0.8, the deviations from the HH result for G_d/G_p shown here can be significant in real material systems.

Figure 2.10 also shows that G_d/G_p is actually *non-monotonic* in α for finite crack extension and volume fraction. At sufficiently high α, G_d/G_p begins to decrease rapidly. Furthermore, G_d/G_p appears to drop to zero in the limit α=1.0 for all cases considered. This differs significantly from the HH result, for which G_d/G_p appears to become infinite as α approaches unity. The decrease in G_d/G_p at very high α can be understood physically within the framework of our calculations as follows. With the same Poisson's ratios for both fiber and matrix, α is simply defined as $(E_f-E_m)/(E_f+E_m)$ under plane strain assumptions. As α increases toward unity, the fiber become infinitely stiff relative to the matrix, i.e. $E_f/E_m \rightarrow \infty$. Thus, all of the applied load is carried by the fiber and all of the strain energy is stored in the fiber; there is no strain energy in the matrix. For a crack which deflects along the interface, there is essentially no energy released due to relaxation of the tensile fiber stress and no energy released by the matrix. For a penetrating crack, there is certainly energy released in the fiber. Therefore, G_d should approach zero while G_p is still finite, and hence G_d/G_p approaches zero. Another way to consider this limit is that at α=1 there is no real matrix material and so the "interface" is already essentially a

free boundary and so a "crack" along this boundary makes no change to the stress field and no change to the energy. The behavior for $\alpha \rightarrow 1$ is easier to observe in a composite of a large fiber volume fraction (small matrix volume fraction) because the total strain energy in the matrix is smaller than for a larger matrix volume fraction. Although this limit is not generally attained in CMCs it could have implications for matrix crack growth in polymer matrix composites, for which α can approach unity.

We now return to consider the effect of the Dundurs' parameter β. As noted earlier, the HH work [17] corresponds to β=0 and Martinez and Gupta [19] showed relatively small changes for $\beta \neq 0$ over a narrow range. However, recalling that the singularity exponent λ, which affects the energy release rates, also depends on β, we need to explicitly consider these differences within our computational model. To fix β=0 requires choosing certain special combinations of the Poisson's ratios of the fiber and matrix. To demonstrate the β effect we studied several values of α : α=0.333, 0.5 ,0.667 and 0.75, and fixed E_m. By varying E_f, ν_f and ν_m at the same time using MathCad ^{TM}, we found sets of underlying material parameters for which β=0, as shown in Table 2.I. Note that to obtain β=0 requires that one of the Poisson's ratios must become rather large, and in the limit of α=1 one must have ν_m=0.5. Although the values in Table 2.I are not unique, we have found that the results for G_d/G_p at fixed α and β=0 as obtained from different sets of the remaining material properties E_f, ν_f and ν_m are very close. The values in Table 2.I thus suffice for investigating some effects of β. Figure 2.11a shows our results for G_d/G_p with V_f=1%. At the smallest crack extension of $a_d=a_p=a=0.002r_f$, our predictions with β=0 are now in extremely good agreement with the HEH results over the full range of α, although the differences with our previous results are quite small. At larger crack extensions, the difference between β=0 and $\beta \neq 0$ (fixed ν_f and ν_m) increases slightly with increasing a, with the ratio G_d/G_p increasing for the β=0 case. Thus, deflection is slightly more difficult under the realistic conditions of fixed Poisson's ratios rather than fixed β=0. Figure 2.11b shows our results for V_f=40%, and it appears that with the high fiber

Table 2.I Combinations of material properties used to obtain β=0.

α	E_f/E_m	ν_f	ν_m
0.333	2.27	0.111	0.360
0.500	3.54	0.179	0.425
0.667	5.81	0.311	0.471
0.750	8.60	0.220	0.473

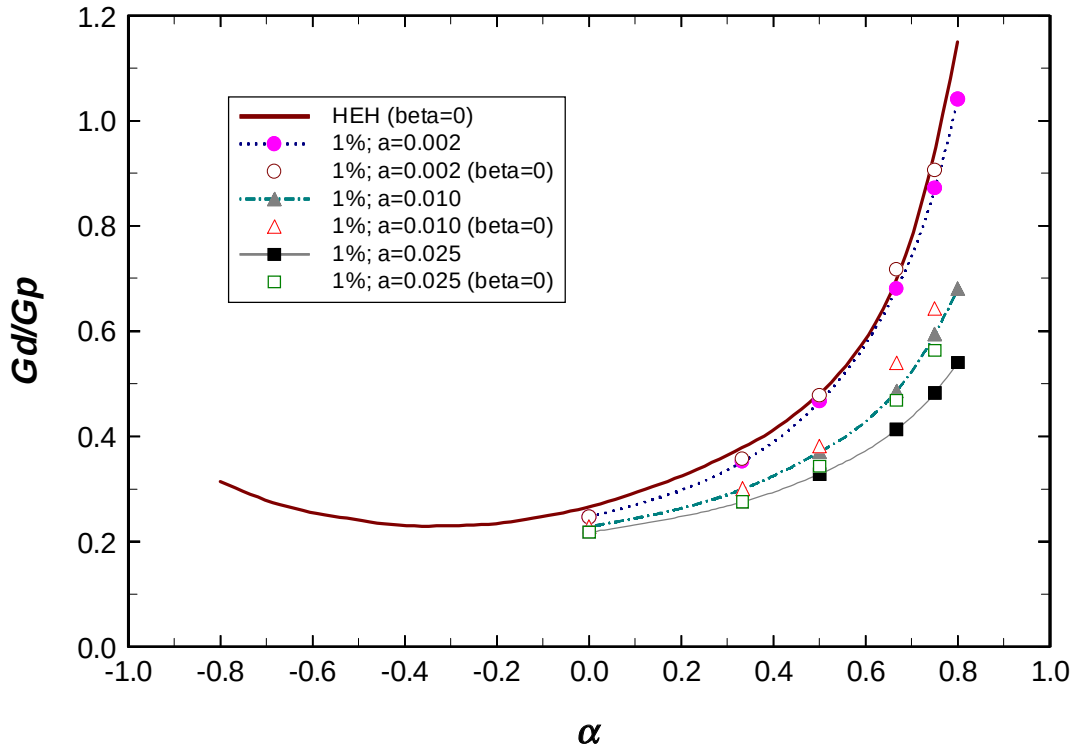

Figure 2.11(a): G_d/G_p versus α with β=0 assumption for V_f=1%.

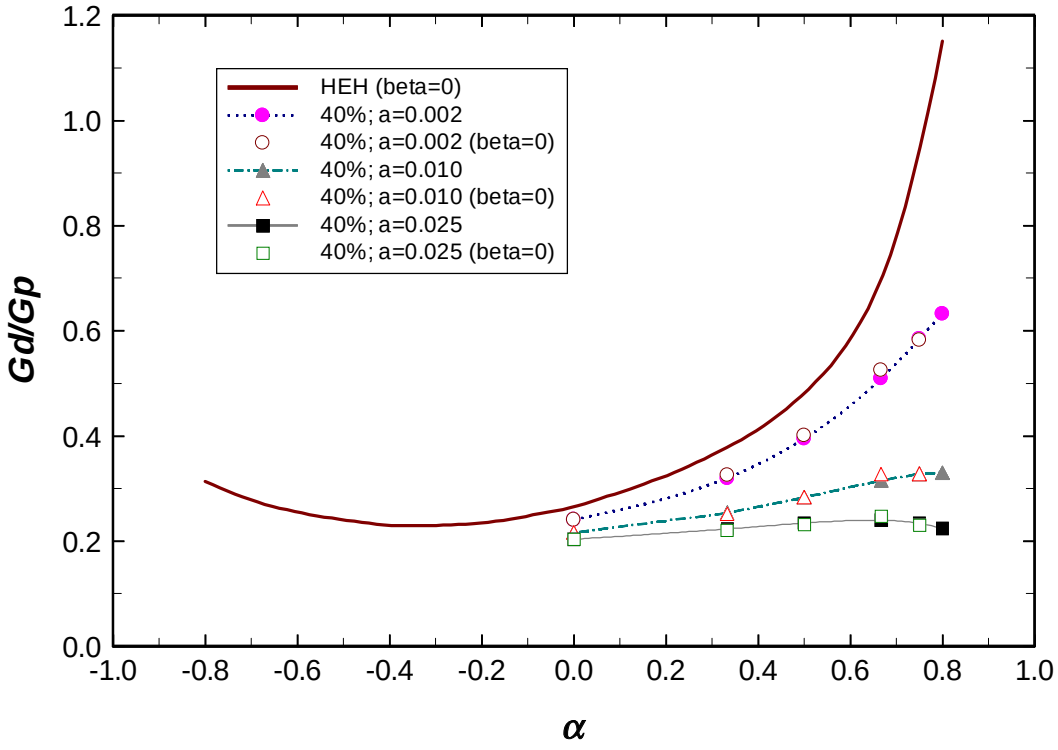

Figure 2.11(b): G_d/G_p versus α with β=0 assumption for V_f=40%.

volume fraction the effect of β becomes essentially negligible. These results are in keeping with the general results of the previous work [17-19].

Since we have all of the individual values for G_d and G_p at the various crack extension lengths, we can consider (to a limited extent) the variations in G_d/G_p for the situation $a_d \neq a_p$. Figure 2.12a shows the ratio G_d/G_p versus α for V_f=1% and a_p=0.01r_f with variable a_d=0.002r_f, 0.01r_f and 0.025r_f. The variations in G_d/G_p are generally as expected from the analytic results of Eq. (2.7): as a_d increases, the ratio and hence the tendency for deflection increase for λ<1/2 but they decrease for λ>1/2. In fact, the analytic dependence of $G_d/G_p \propto (a_d/a_p)^{1-2\lambda}$ closely describes the variations found here over the modest range of a_d/a_p studied (λ vs. α, β is given in Fig. 2.2). For instance, at α=0.8, with a_d/a_p=2.5 G_d/G_p from the analytic relations is 116% of that for a_d/a_p=1.0, while our results show G_d/G_p for a_d/a_p=2.5 is 119% of that for a_d/a_p=1.0. Figure 2.12b shows the ratio G_d/G_p versus α for V_f=40% and a_p=0.01r_f with variable a_d=0.002r_f, 0.01r_f and 0.025r_f. In this case, the dependence on a_d/a_p is rather smaller than at the lower volume fraction and the variations at larger α are somewhat weaker than the asymptotic behavior $(a_d/a_p)^{1-2\lambda}$. In general, for the higher volume fractions, the equal case $a_d=a_p$ can be used with reasonable accuracy to approximate modest variations in a_d/a_p.

Finally, we consider the effect of pre-existing flaws/cracks on the present crack deflection/penetration criterion. Two cracks of the same lengths are assumed in the composite as shown in Fig. 2.7; one is along the interface and the other is through the fiber. Four different crack extensions are considered in Fig. 2.13 and it is shown that the pre-existing cracks tend to decrease the tendency to deflection of a matrix crack. The dotted line with solid circles represent the "no pre-existing crack" case with the crack extension of $a_d=a_p$=0.002r_f. For the other calculations, the sizes of pre-existing cracks are 0.002r_f, 0.010r_f, 0.015r_f and 0.025r_f, respectively, and very small crack extensions of 0.0001r_f are used for all the cases since the crack sizes are already as small as our crack extensions in the other results. Note that in order to advance the crack tip across the fiber/matrix interface, employing a very thin additional layer at the penetrating crack tip is

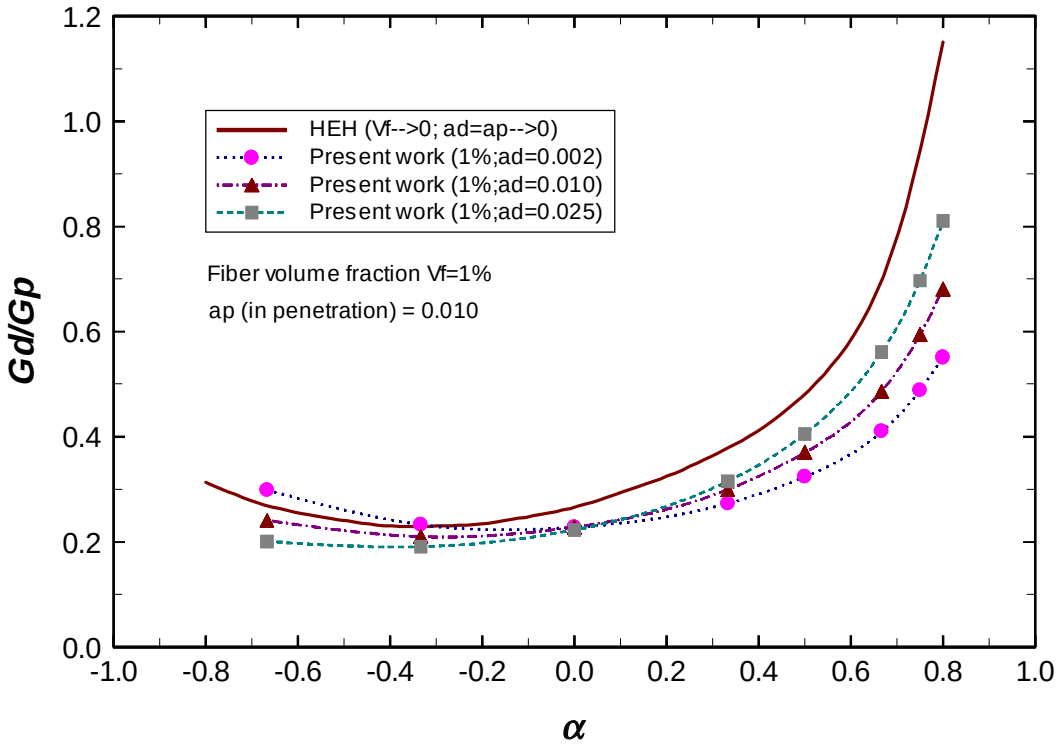

Figure 2.12(a): G_d/G_p versus α with $a_d \neq a_p$ assumption for V_f=1%.

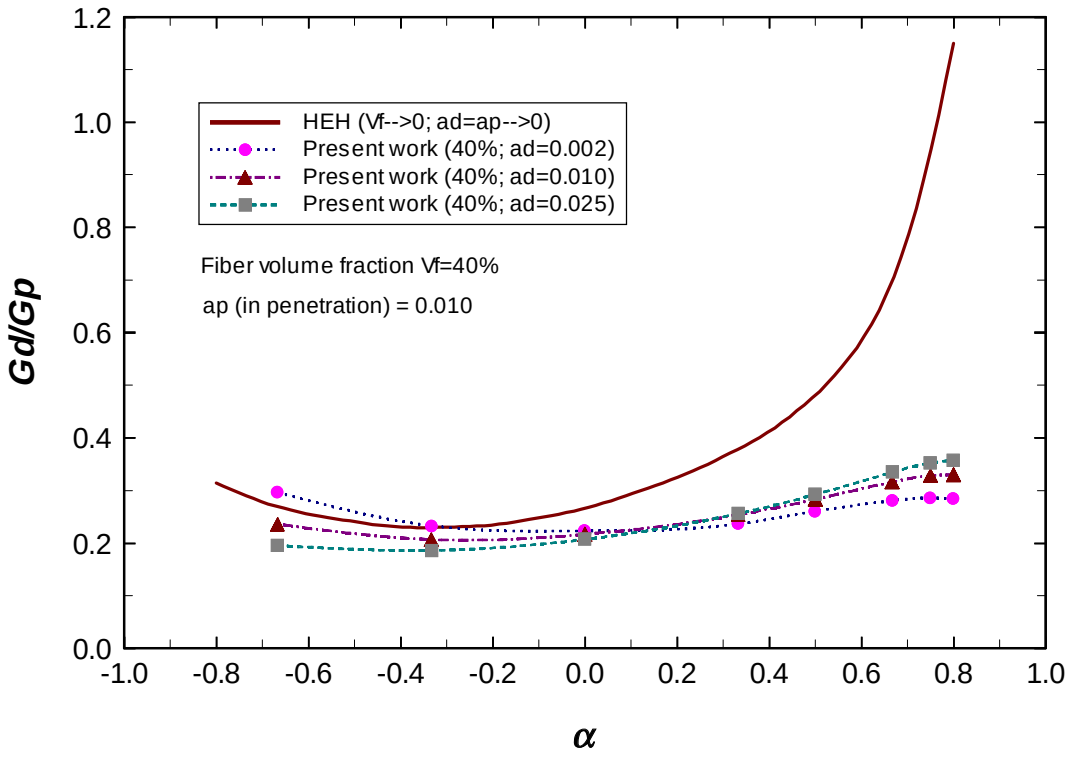

Figure 2.12(b): G_d/G_p versus α with $a_d \neq a_p$ assumption for V_f=40%.

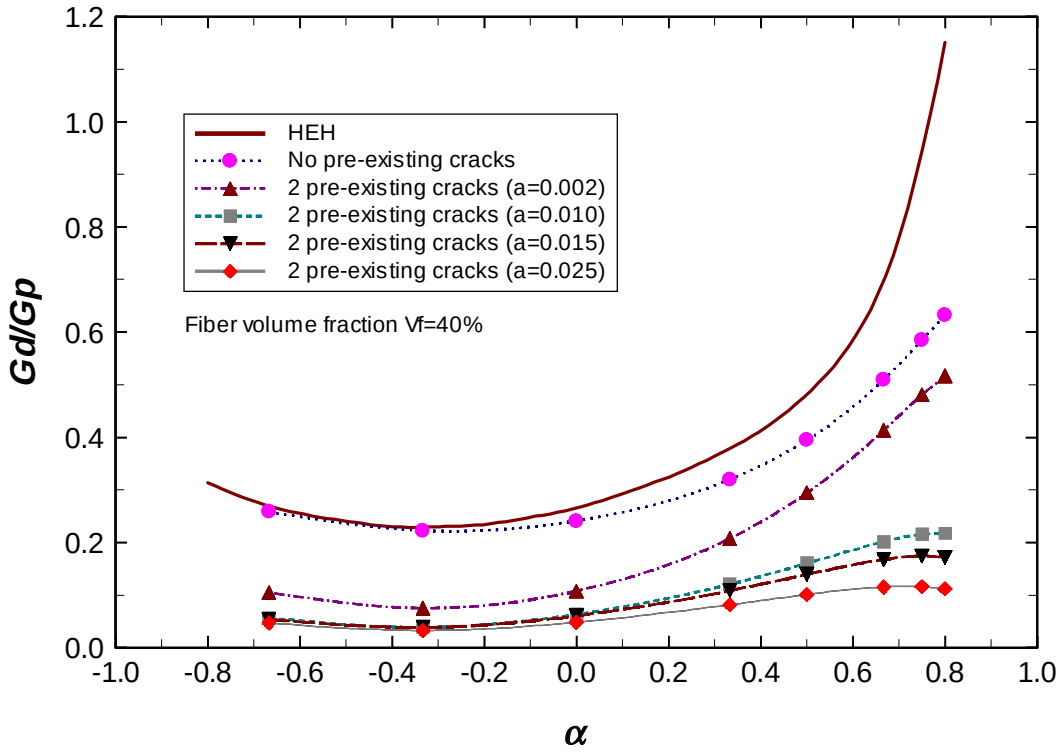

Figure 2.13: G_d/G_p versus α in a composite with two pre-existing cracks.

unavoidable, however due to computational limit in the ADM model adding the layer of $0.0001r_f$ from the material interface is not possible. Crack advance by the same small amount inside the material region is possible by moving the additional layer at the crack tip without adding another layer for the advanced crack. Comparing the uppermost curve ($a=0.002r_f$) and the other curves ($a=0.0001r_f$) in Fig. 2.13 may not look quite appropriate because they used different crack extensions, but considering that the $a=0.002r_f$ gives a very good agreement between our numerical criterion and HEH's analytical solution (which assumes "zero" crack extension), we believe the comparison is valuable. With the long crack extensions such as $a=0.025r_f$, G_d/G_p drops considerably over all range of α, and to ensure the deflection of a matrix crack, the surface energy of interface should be smaller than 5 ~ 10% of fiber surface energy. Even with the small size of the pre-existing cracks ($0.002r_f$), the prospects for crack deflection drops by ~50% (at low α) to ~20% (at high α).

2.4.2. Comparison to Experiment

We have shown various predicted results for G_d/G_p versus fiber volume fraction V_f and crack extension a. Here, we compare those predictions to careful experiments on model composites.

Two glass matrix/SiC fiber model composites have been fabricated at the Wright-Patterson Air Force Base Laboratory, as described in Ref. [34]. The glass matrices are a borosilicate 7040 glass and a home-made "F-glass". The reinforcing fibers are Textron SCS-0 SiC fibers, which are $67\mu m$ in radius and have no coatings. The elastic and toughness properties of these materials are shown in Table 2.II. The critical strain energy release rate or surface energy is calculated from the toughness K_{Ic} via $\Gamma=K_{Ic}^2(1-\nu^2)/E$ in each case. These constituents were combined to form a unidirectional composite with 35% volume fraction of fibers. The coefficients of thermal expansion of the fibers and matrix materials are essentially equal (F-glass) or very close (7040 glass) so that there

Table 2.II Material properties for F-glass, 7040 glass matrix and SCS-0 fiber.

	E (GPa)	ν	α (°C)$^{-1}$	K_{IC} (MPa$\sqrt{}$m)	Γ (J/m^2)
F-glass	59	0.20	4.25	0.79	10.155
7040 glass	50	0.20	5.40	0.77	11.384
SCS-0	423	0.15	4.23	2.60	15.622

are no significant thermal residual stresses present in the as-fabricated composites. These model composites are thus well-suited for direct comparison against the predictions of the present work and the HEH results [19] because of the absence of the complicating issue of residual stresses and the absence of intermediary fiber coatings. Uniaxial tension tests were performed on these materials and the fracture surfaces were examined for evidence of interfacial crack deflection.

From the constituent property data shown in Table 2.II, it is straightforward to determine that the elastic mismatch in the F-glass is α=0.751 and in the 7040 glass is α=0.785. The only uncertain parameter is the value of Γ_i. Here, we assume that the interface toughness is the same as the matrix toughness, $\Gamma_i=\Gamma_m$, since there is reasonable bonding between the SiC and the glass; this is expected to be an *upper bound* on the true Γ_i. With these values, the ratio of Γ_i/Γ_f can be formed and can be appropriately overlaid on the G_d/G_p vs. α parameter space, as shown in Fig.2.14. Also shown in Fig. 2.14 are the HEH prediction for G_d/G_p, which lies above the experimental data points for Γ_i/Γ_f and hence predicts crack deflection. Our predictions for this specific system at the experimental volume fraction and various $a_d=a_p=a$ are also shown in Fig. 2.14; all of the curves lie below the experimental data points and hence predict crack penetration. The observed fracture mode is crack penetration, as shown by the micrograph of the composite fracture surface (Fig. 2.15). Although there is some structure to the fracture surface indicating that the fibers do affect the overall propagation of the propagating matrix crack, there is absolutely no evidence of any crack deflection at any of the fiber/matrix interfaces across the entire composite. The HEH criterion thus appears to overestimate the tendency for crack deflection while the present results for finite crack extensions are consistent with the experimentally observed deflection. Again, because of the uncertainty in the physical meaning and values of a_d and a_p, the present predictions are not definitive but merely illustrative of the deleterious effects associated with finite crack extensions.

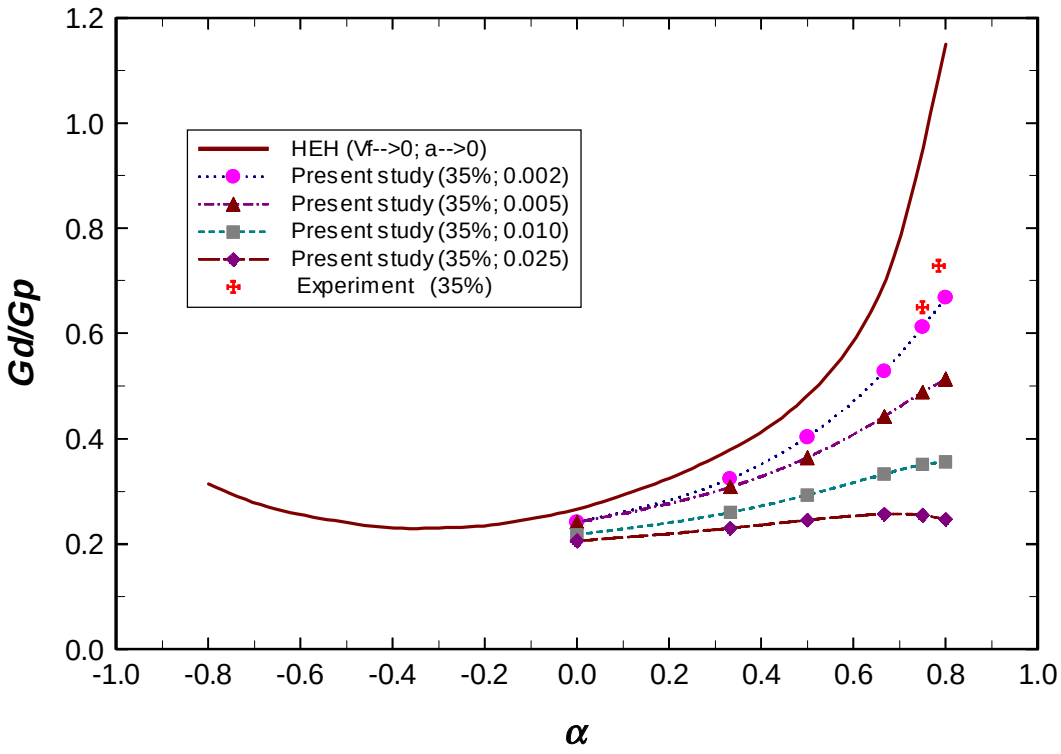

Figure 2.14: Comparison of the present study with experiment data on SCS-0/glass composites.

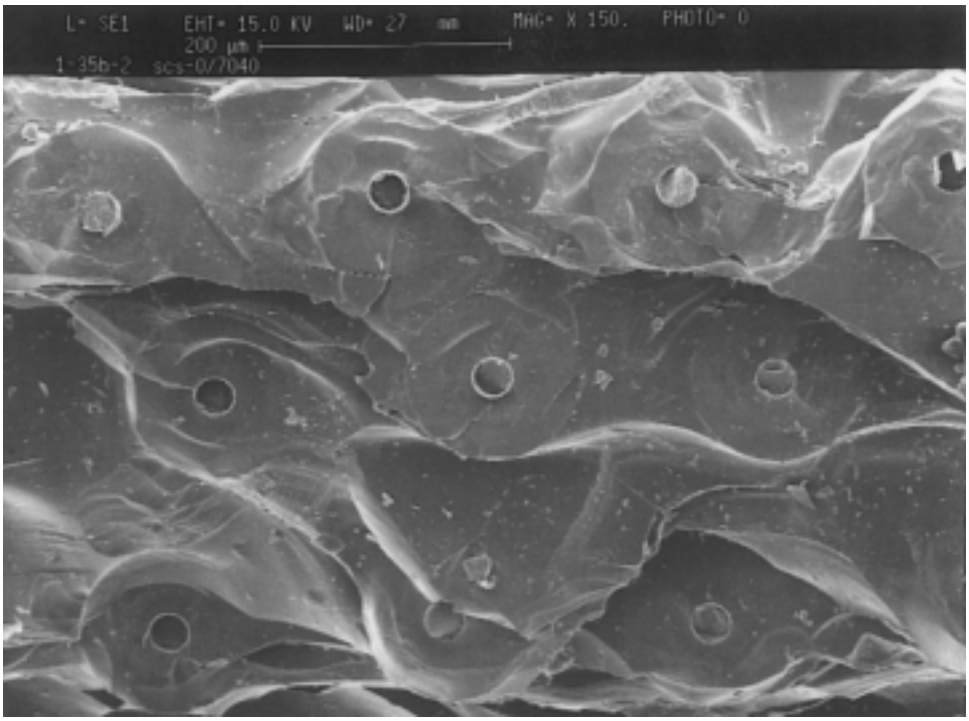

Figure 2.15: Fracture surface of an SCS-0/7040 composite.

2.5. Summary/Discussion

We have developed an energy-based criterion for predicting crack deflection versus penetration as a function of the fiber and matrix elastic mismatch, fiber volume fraction, and crack extension length for an axisymmetric geometry. Using a new numerical technique, we have reproduced quite accurately the analytic HEH results which apply in the limit of both V_f and a_d=a_p approaching zero. For finite volume fractions and finite, but small, crack extension lengths, we find that the tendency for crack penetration is enhanced, i.e. the ratio G_d/G_p decreases as V_f and a_d and a_p increase. In the limit of $\alpha \rightarrow 1$ we predict G_d/G_p=0 so that deflection becomes impossible. We also find a weak dependence on the Dundurs' parameter β and a weak dependence on the ratio a_d/a_p at realistic volume fractions. Experiments on model composite systems with convenient intermediate ratios of Γ_i/Γ_f show crack penetration, consistent with the present predictions over a range of crack extensions and in contrast to the prediction of deflection using the HEH criterion. Finite values of V_f and a_d, a_p can thus play an important role in determining the tendency for interfacial crack deflection, which in turn then controls the toughness of the entire composite. The present results provide a guideline for estimating deflection versus penetration for various elastic parameters, interface toughness, volume fraction, and crack extension.

The major unsolved issue in this entire field remains the interpretation of the crack extension lengths a_d, a_p. Taken separately, the energy release rates are unphysical in the limit of a_d, $a_p \rightarrow 0$ and so there must be some intrinsic length scales at which the continuum limits apply. These length scales could be atomic, in the case of perfect interfaces, in which case a_d, $a_p << r_f$ and the HEH criterion would be expected to hold after explicit accounting for the marginally different lengths a_d, a_p at the atomic scale. While perhaps an appealing approach, the experimental data presented here would not be consistent with the HEH criterion. The length scales could be larger, and controlled by characteristic structural defects at larger length scales such as misfit dislocations or grain boundary

orientation. The apparently obvious candidates for a_d, a_p are pre-existing crack-like flaws along the interface and in the fibers. Even if true, however, such flaw sizes could not be determined experimentally. Although "typical" flaw sizes in the constituent fibers can be assessed by measuring fiber strength, such flaws are the largest flaws existing along a macroscopic length of fiber; they do not reflect the typical flaws present in the fiber at much smaller length scales. Measuring flaw sizes in the interface is even more difficult and suffers from similar interpretation problems. Furthermore, as a matrix crack approaches a flawed fiber and/or interface, the problem to solve is quite different than the approach in previous work [17-19], where there is only one crack. As a first approach we have studied the energy release rates for each of two coexisting crack tips branching off from the main matrix crack, with one branch along the interface and one along the fiber, assuming the crack tips have the same lengths. However, the solution of such a problem still does not complete the space of possible cracking modes. For instance, macroscopic evidence of interfacial crack growth ahead of an impinging matrix crack has been presented recently by Lee *et al.* [35] and analogous behavior could occur at the fiber/matrix interface on scales orders of magnitude smaller. This would suggest the applicability of a strength-based criterion using the stress field due to the matrix crack acting on pre-existing flaws a_d, a_p, although still presuming the existence of flaws.

The issue of the physical nature of a_d, a_p is clearly critical, and the prospects for general engineering design rules which involve only macroscopic constitutive properties, such as moduli and toughness, hinges on this issue. If a_d and a_p are flaw-related, then composite performance will ultimately be controlled by processing details rather than constitutive material properties, which does not bode well for the application of general design guidelines. The present results begin to demonstrate, within the existing energy-based framework of deflection versus penetration, the sensitivity of the engineering design curve (G_d/G_p vs. α) to the incipient or notional crack extension lengths a_d, a_p in realistic (axisymmetric and high volume fraction) fiber-reinforced ceramics.

Chapter 3. STRESS STATES AROUND A SLIDING INTERFACE

When a matrix crack reaches the fiber/matrix interface in a CMC, deflecting the crack is a key condition to increase the fracture toughness and damage tolerance. Once the crack is deflected, then the interface may open or slip. Besides, the pre-existing interfacial flaws may grow and develop into crack-like imperfections. In fact, the real interface may consist of complex combinations of those imperfections as well as the perfectly bonded zone [36,37]. The stress-free open crack (total debonding) and the debonding with slip due to friction are typical failure modes at the interface, and both may be defined in the composite model by the adequate boundary conditions at the crack surfaces and tips. Our goal of this Chapter is to examine the role of a frictional interface on the microstress fields in the composite. An open interface crack is not considered because roughness at the interface generally induces substantial friction. In addition, we postulate the clamping stress at the interface by the thermomechanical mismatch of neighboring constituents is big enough not to allow open cracks at the interface when debonding occurs. Note that the interfacial friction was neglected without conflict in the previous Chapter since we assumed the crack extension along the interface was only incipient and of a microscopic size. To model the slip zone along the interface, a prescribed constant shear stress is assumed. With the aid of the ADM, the effects of the extent of slip on the microstress fields around the sliding interface are investigated. We then assess the effects of increasing load on the matrix stresses, which are responsible for driving matrix cracks, to understand the cracking evolution phenomenon. The results are compared to the commonly-used shear-lag model solutions in which a constant τ is assumed. Finally, the microstress distributions near the interface are analyzed to understand the possibility of fiber failure. It appears that the radial variation in the fiber axial stresses tend to increase the probability of fiber failure, which is not expected from the simple shear-lag model. We conclude that the shear-lag model is accurate enough to calculate the stress distributions in the matrix, but it may underestimate the possibility of fiber failure. Nevertheless, the radial variation of the fiber axial stress is not expected to

change the overall stress/strain relations since the strain calculation is not radial location-dependent, but a function of the average axial stress in the fiber.

3.1. Introduction

In general, the interfacial shear stress in the friction zone (sliding zone) is modeled either as a prescribed material constant [38-44] or by Coulomb friction law [45-51]. The prescribed shear stress can be regarded as a characteristic critical stress at the interface that should be overcome in order for debonding to propagate [42,43]. It is recognized that the model may be more appropriate when interface roughness is such that shear yielding must occur before relative slip between fiber and matrix can take place [41,46]. The main drawback of this model is that the interfacial frictional stress after debonding is generally lower than the aforementioned critical stress and, moreover, may not be constant. According to Coulomb friction law, the interfacial friction stress depends on the normal stress and at any instant in the loading history, either sticking (perfect bonding), slipping or opening occurs at a generic point along the interface [49]. In an axisymmetric concentric cylinders composite, the Coulomb friction law can be written as

$$\tau = -\mu\sigma_{rr} \; ; \; \sigma_{rr} < 0 \tag{3.1}$$

where μ is the friction coefficient and σ_{rr} is the stress acting normal to the interface. This approach may be a more realistic assumption, but whether the friction coefficient is constant all along the slip zone is another unsolved issue; if μ is not constant, estimating pointwise μ will be hardly possible. It is now obvious that the difference between the predictions of the two approaches stems from the presence of thermal residual and Poisson effects. Both the constant τ and Coulomb friction assumptions have been widely used for the analysis of strength and toughness of fiber-reinforced composites, but it is hard to say which approach is more applicable in real systems.

In the present study, we choose the interface condition as follows. We assume a constant shear stress, τ, in the slip zone such that the prescribed τ implicitly includes the Poisson effect and the thermal stress effect. Since we are mainly interested in the "qualitative" assessment of the effects of slip and increasing loading on the stress distributions rather than in the quantitative evaluation on the stress transfer from broken matrix to the adjoining intact fibers, the above assumption should be acceptable. Furthermore, since one of the main goals of this Chapter is to provide insight into the validity of the shear-lag model and the shear-lag model-based approaches assuming a constant τ, which we will use in Chapter 4, we accept the constant τ assumption as reasonable.

Before proceeding with the present work, we review some of the previous work related to the sliding interface problems. Since the importance of the interface region was acknowledged to determine the ultimate properties of a given composite [38,39], many authors have focused on modeling the imperfect interface, or imperfectly bonded interface to fully understand the mechanics of interface as a function of material and geometrical parameters. Dollar and Steif [48] considered the two-dimensional broken fiber problem where the interface is subjected to a Coulomb friction law. They found that the stress near the fiber break was nonsingular and the stress concentration depends on τ and the applied load. More importantly, Dollar and Steif showed that the rate at which load is transferred back to the fiber is significantly slower than the transfer rate assuming perfect bonding, more consistent with simplified shear-lag model. A later work by Dollar and Steif [49] included semi-infinite cracks as well as the finite cracks within the framework of integral equation technique. Steif and Dollar [44] have provided a similar model by prescribing constant shear stress once a maximum value has been reached in a ductile composite. Schwietert and Steif [50] developed an integral equation method to solve the problem of a crack impinging on a frictional, bimaterial interface, where an infinitely long cracked fiber in an infinite plane is subjected to tensile loading. Coulomb friction is assumed in the sliding zone, and the compressive residual stress normal to the interface is acting as a clamping stress. It appears that the length of slip zone and the shear stress along the slip zone are significantly dependent on the elastic mismatch as well as the friction coefficient.

Pagano and Tandon [52] developed a new approximation approach called NDSANDS which evaluates the effective thermoelastic moduli of continuous fiber-reinforced CMC in which debonding and slipping occurs at the interface. The model involves the calculation of composite stress and strain defined as volume-averaged quantities. Solving the boundary value problem in which interfacial displacement continuity is not satisfied, Pagano and Tandon provided the upper and lower bounds on composite moduli by considering two extreme cases of interface; perfectly bonded interface and completely separated interface. They also pointed out that under imperfect interface conditions, the mathematical (volume average) and physical (surface measurements) definitions of composite strains are not necessarily the same and therefore lead to different values of the composite effective moduli.

Wijeyewickrema and Keer [42] presented a linear elastic analysis of interfacial slip under longitudinal tensile loading in a fiber-reinforced brittle matrix composite with matrix cracks terminating and blunting at the interface. A prescribed constant shear stress distribution was taken in the slip region. They noted that maximum slip occurs away from the crack plane and that the peak decreased with increasing slip length. They were among the first to investigate the effects of fiber volume ratio and slip length on the interfacial adhesive stress and the stress fields in the brittle matrix. However, their assumptions did not satisfy one of the basic equilibrium equations and did not agree with results by the other authors including Tandon and Pagano [55].

Kaw and Pagano [53] used the same geometry as Wijeyewickrema and Keer [42], and included an imperfect interface but by approximating the interface by distributed shear springs of constant stiffness. They relaxed the assumption of dilute volume fraction and a through annular crack made in Schwietert and Steif's model [50], and solved for an annular crack in a concentric cylinder under a remote uniform axial strain and constant temperature change. A later work by Kaw *et al.* [54] extended the previous work to the problem of frictional interface, where the Coulomb friction law was assumed. The

effects of friction constant, temperature change and remote axial strain on the extent of the interfacial damage and the stress fields in the fiber and matrix were studied.

Recently, Tandon and Pagano [55] have examined the stress and displacement fields in the vicinity of matrix cracks approaching a frictionally constrained interface. A modified version of the variational theorem, originally based on the Reissner's theorem [22], was used for an axisymmetric concentric cylinder model. The configuration has an annular crack in the axial plane of matrix while the fiber/matrix interface is made to obey the Coulomb friction law. Their results were compared, for an identical geometry and loading, to numerical elasticity solution by Kaw *et al.* [54], and showed good agreement.

In this Chapter, our main goal is to model the sliding interface and analyze the stresses around the sliding interface. This is the classic problem solved by simple shear-lag analysis; we desire more improved and more detailed solution in order to assess the accuracy of shear-lag solution. To this end, we first investigate the effects of the extent of debond slip on the microstress such as the shear stress and radial stress at the fiber/matrix interface, and the axial stress in the matrix on the recognition that the extent of slip determines non-linear inelastic strains which are responsible for considerable damage tolerance in the material [50,56]. To do so requires establishing the necessary boundary conditions across the cracked interface and at the tip of the debond. Results show that the longer slip length causes a smaller τ, and the constant τ in the slip zone decays gradually within a distance of fiber diameter from the debond crack tip. The relative interfacial slip is shown to be influenced by the magnitude of slip length. The comparison of the results with a shear-lag model in which interfacial slip is included will be given.

Secondly, we characterize the relationship between the increasing applied loads and the axial stresses in the matrix which are responsible for driving matrix cracks. This time we fix the interfacial sliding resistance and find the appropriate slip length, at each load step, to satisfy the given boundary conditions. Through this modeling, we can see how the matrix stress profile changes during the evolution of matrix cracking under increasing

load. Results show that the increasing the applied load does increase the slip length, but does not increase the matrix stresses in the debond region. The shear-lag model used for the first problem is again used for comparison. Physical interpretation of the results in conjunction with the multiple matrix cracking phenomenon will be also given.

Finally, we seek to relate the fiber axial stresses to the possibility of fiber failure. Noting that the fiber failure is controlled by a statistical distribution of microstructural surface flaws [57,58], we are interested in the stress distributions in the fiber near the fiber/matrix interface. It is shown that the axial stresses reach very large values at the matrix crack plane, and particularly near the fiber/matrix interface stress concentration is critically high. We also show the radial variation of the axial stresses in the fiber is significantly dependent on the magnitude of interfacial sliding resistance and consequently on the slip length. These suggest that the widely-used simple shear-lag models, which assume the axial stresses in the composite constituents are uniform, may not be accurate enough to relate the matrix cracking and interfacial debonding to probability of the fiber failure.

The remainder of this Chapter is organized as follows. In Section 3.2, we briefly review the basic ideas of shear-lag models. In Section 3.3, we discuss the effect of the slip length on the microstress field. We first define and model the problem of imperfect interface, and use the ADM model to investigate the effect of slip length on the microstress distributions and crack opening displacement. In Section 3.4, we examine the relations between the applied loads and the matrix axial stresses. Section 3.5 contains the study of the stress concentration (enhancement) near fiber surface along the matrix crack plane. Finally in Section 3.6, summary and discussion are given.

3.2. Shear-Lag Model

Shear-lag model is the most frequently-used approach to analyze the stress field in a composite, when the interface is either perfectly bonded or subjected to a friction. The original shear-lag model was suggested by Cox [59] to calculate the load transfer between fibers and the matrix in the neighborhood of either a fiber break or a matrix crack where there is perfect interface bonding. Aveston and Kelly [60] developed a model for load transfer in a matrix-cracked composite and derived concise expressions for the matrix cracking strain energy balance principles. Aveston *et al.* [38] presented a micro-mechanical model that accounts for frictional load transfer, assuming that the interfacial shear stress is a constant for a particular composite material system. Among others which assume the constant τ are the work by Marshall *et al.* [39], Budiansky *et al.* [40] and McCartney [41]. On the Coulomb friction problem, Piggot [61] and Steif [47] have developed models to predict stiffness loss resulting from fiber fracture. Gao *et al.* [45] and Sigl and Evans [62] have used a shear-lag model to study stress transfer in fiber pull-out and matrix cracking problem; the latter included the residual thermal stress in their model. Note that some works such as the ones by Hutchinson and Jensen [63] and Hsueh [64,65] considered both of the constant τ and Coulomb friction assumptions. Regarding the experimental approach to obtain the interfacial shear stress, Marshall [66] first proposed the push-out test, assuming the interface is characterized by a constant τ, while Takaku and Arridge [67] and Shetty [68] explored the possibility of non-constant τ. The more details of the above works will be discussed in Chapter 4.

Before we introduce some basic equations derived from the shear-lag model including constant interfacial friction, it is worth noting the differences between shear-lag model for polymer matrix composites (PMCs) and that for CMCs. In a compliant matrix reinforced by stiff fibers such as PMCs, the model well explains the load transfer from a broken fiber to the intact neighboring fibers through matrix. The matrix is assumed to carry only shear load while all the axial load is sustained by the fibers. In other words, the axial stiffness of the matrix is too small, compared to that of the fibers, to carry the axial load and the matrix plays a simple role of load transferring. In CMCs, however,

since the matrix is stiff enough to be able to sustain the axial load, the role of matrix is not merely load transferring. Furthermore, the first crack mode is not a fiber break in this case, but a matrix crack. Hence, the basic shear-lag model for CMCs relates the stress field in a broken matrix to that in the adjoining fibers.

In a matrix-cracked CMC, the axial stress on the matrix crack plane is obviously zero, and thus all the load on that plane should be carried by the fibers. The matrix axial stress will recover from zero to a pre-cracked value in some distance, and on the other hand, the fiber axial stress will decrease from a peak value at the matrix crack plane and reach a steady-state value in the same distance from the crack plane. In a CMC whose interface is under constant shear stress, the stress recovery/decay is expected to be linear, and the constant shear stress assumed in the debond/slip zone is often referred to as the "interfacial sliding resistance" or simply "sliding resistance".

In an axisymmetric composite, the average axial stresses in the fiber and matrix are governed by the following relations

$$\sigma_f(z) = \frac{\sigma}{V_f} - \frac{2}{r_f}\int_0^z \tau\, dz \tag{3.2}$$

$$\sigma_f(z) V_f + \sigma_m(z) V_m = \sigma(z) \tag{3.3}$$

where the origin of the z axis is at the matrix crack plane. In the above equations, r_f is the fiber radius, V_f and V_m are the volume fractions of fiber and matrix, respectively. σ is the applied remote stress and τ is the interfacial sliding resistance, while $\sigma(z)$ is the average stress at z in the composite determined by the stress equilibrium equation called the rule of mixtures (Eq. (3.3)). Note that the stress component, $\sigma_f(z)$, in the above equations is a function of z only. The dependence on the radial locations, which is possibly critical in the evaluation of the fiber stress field and in the prediction of fiber failure, is not considered.

Providing that the applied loads are not sufficient to cause fiber failure, the strain associated with any section of the composite is precisely the strain in the fibers because the fibers are deforming elastically with modulus E_f in response to the axial stress field, while the matrix experiences the unrecoverable permanent deformation once it starts to crack. The stress/strain relations can then be obtained from applying Eq. (3.2) to the whole composite length, L_T, as

$$\varepsilon_c = \frac{1}{L_T E_f} \int_0^{L_T} \sigma_f(z) \quad . \tag{3.4}$$

If the fiber stress is radial location dependent, the above equation for composite strain turns out to involve the fiber surface-averaged axial stress.

One of the main objectives in this study is the validation of the shear-lag model in the stress/strain relations. Since the axial stresses in the fiber and matrix are assumed uniform across the respective surfaces in the shear-lag model, we desire to investigate how accurately the model predicts the stress distributions in both fiber and matrix. For the analysis we employ the ADM model whose validation on the energy release rate calculations was already performed in the previous Chapter. Detailed usage of the ADM model for the present problem will be discussed in the next Section.

3.3. Slip length Effects

3.3.1. Problem Description

In order to investigate the slip length effects, we use an axisymmetric model composite in which a matrix crack extends to the fiber/matrix interface, with a debond slip zone along the interface (see Fig. 3.1). This configuration can be viewed as the representative volume element (RVE) when a hexagonal array of fibers in a matrix is considered. Each material is assumed to be isotropic and linearly-elastic, and composite

length is assumed infinite. The radii of fiber and matrix are $a(=r_f)$ and $b(=r_m)$, respectively, and the volume fraction of fibers, V_f, is calculated from $V_f=(a/b)^2$. The interfacial slip zone is assumed to be subjected to a constant τ and a far-field uniform longitudinal tensile strain ε_0 is applied to the body.

For the stress analysis, we use the ADM model which was introduced in the previous Chapter. In these stress calculations, we assume that the shear stress is continuous at the debond crack tip; singularity or jump in the shear stress at the crack tip is not allowed. To obtain τ, we fix the debond length and determine the shear stress needed to satisfy all of the given boundary conditions and the applied load. Specifically, a guessed initial value of τ is first chosen into the ADM, and is adjusted iteratively, with corresponding values of τ, until the shear stress continuity condition is satisfied within a desired accuracy. In this Section, we particularly investigate the effect of the extent of slip on the shear and radial stresses and relative slip at the interface, and on the axial stress in the matrix along the outer boundary. In addition to the crack tip boundary conditions, there are more general boundary conditions which should be satisfied on the boundaries such as interface, cylinder surfaces and cylinder ends. They will be discussed in the next Section.

The additional annular layers needed to increase the accuracy of ADM results are located at r/a=0.8, 0.9, 0.95, 0.975, 1.025, 1.05, 1.1, 1.2. Unlike the strain energy calculations, stress calculations do not require very thin layers near the matrix crack tip except for some particular cases we will show in Section 3.4. For the calculations we use SiC/CAS composite, and the material properties are given below (from [42]). Note that the Poisson's ratios of the fiber and matrix are assumed identical so that the Poisson contraction effect can be neglected. Fiber volume fraction is fixed at 40%.

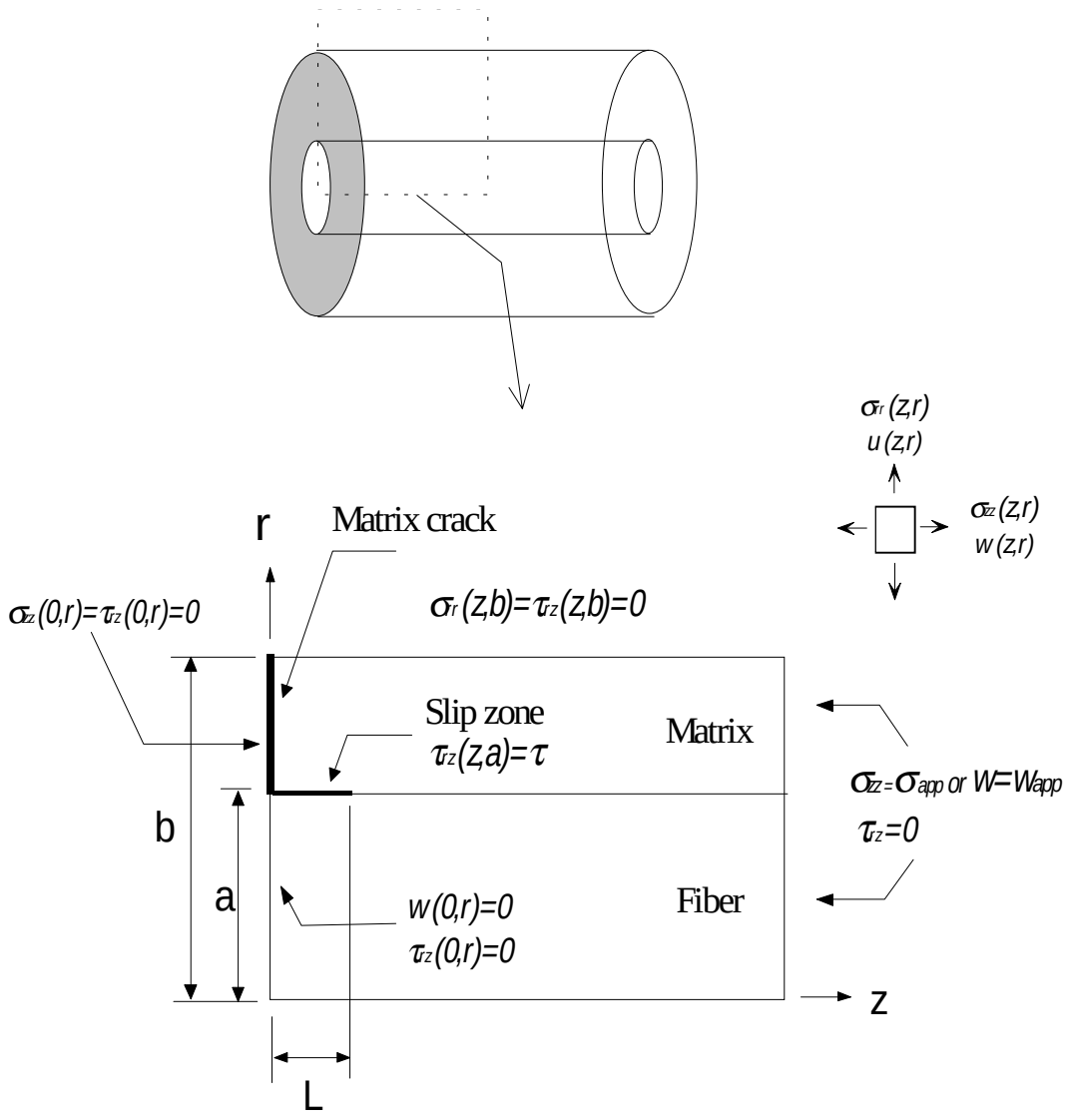

Figure 3.1: Axisymmetric model composite with a slip zone at the fiber/matrix interface.

SiC fiber : E_f = 207 GPa , ν_f = 0.25

CAS : E_m = 98 GPa , ν_m = 0.25

Fiber radius = 1 (nondimensional) ; Matrix radius = 1.581 ; V_f = 40%

3.3.2. Boundary Conditions

The boundary conditions on the outer surfaces of the composite cylinder and the interface conditions at the fiber/matrix interface are not simple at the locations near the matrix crack or slip region. At the interface, we consider two different conditions; one is slip zone with a constant sliding resistance, and the other is elastic zone (stick zone or perfectly bonded region) in which the radial stress and displacement are continuous. In any of these cases, however, the interface should satisfy the following continuity conditions.

$$\sigma^{f}{}_{rr}(a,z) = \sigma^{m}{}_{rr}(a,z) \tag{3.5}$$

$$\tau^{f}{}_{rz}(a,z) = \tau^{m}{}_{rz}(a,z) \tag{3.6}$$

where the superscripts f and m refer to the fiber and matrix, respectively, and the cylindrical coordinates r, z are introduced in Fig. 3.1. For the slip and elastic zones of interface, additional conditions are needed as follows:

Slip Zone ; $u^{f}(a,z) = u^{m}(a,z)$ (3.7)

Elastic Zone; $u^{f}(a,z) = u^{m}(a,z)$ and $w^{f}(a,z) = w^{m}(a,z)$ (3.8)

where u, w are the r, z components of displacements, respectively.

On the external cylinder surface ($r=b$), we can impose two sets of elasticity boundary conditions as

$$\sigma^m{}_{rr}(b,z) = \tau^m{}_{rz}(b,z) = 0 \tag{3.9}$$

or

$$u^m(b,z) = u^T(b,z) + u^M(b,z) \quad \text{and} \quad \tau^m{}_{rz}(b,z) = 0 \quad . \tag{3.10}$$

In the latter equations, u^T is the radial displacement field in the uncracked composite due to a temperature change, ΔT, and u^M results from the mechanical loading. Equation (3.9) minimize the constraint within the class of problems having zero stress on the boundary, and are motivated by the single fiber microcomposite, and Eq. (3.10) maximize the constraint and are motivated by concentric cylinder simulation of hexagonal array of fibers [26,55].

Finally, the elasticity boundary conditions at the crack plane are given by

$$w^f(r,0) = \tau^f{}_{rz}(r,0) = 0 \qquad r \le a \tag{3.11}$$

$$\sigma^m{}_{zz}(r,0) = \tau^m{}_{rz}(r,0) = 0 \qquad a \le r \le b \quad . \tag{3.12}$$

3.3.3. Results/Discussion

We have modeled the problem of a matrix crack extending to the fiber interface, with a debonded zone along the fiber where there is a constant shear stress τ between the fiber and matrix. We investigated these using the ADM model. We attempted to compare our results to analytic results of Keer and Wijeyewickrema (KW) [42] obtained from complex integral equation techniques, and found poor agreement. However, this turns out to occur because of severe errors in the KW work, such that their results do not satisfy simple physically-required limits. Hence, we will focus on the qualitative assessment on the effects of the extent of slip on the microstress distributions.

We have concentrated on situations of relative high τ, and hence short debond lengths, as relevant to SiC/SiC materials and the most difficult case for shear-lag models to study accurately. Fig. 3.2 shows τ, normalized by the applied far-field matrix stress, along the interface for various slip lengths L normalized by the outer radius b of the concentric cylinders shells. The case of zero slip length (elastic case) is also shown. As shown with the L/b=0 case, within the slip zone the shear stress is seen to increase from zero at the matrix crack plane to a large value within a small region adjacent to the plane. For the various slip lengths investigated, this effect is seen to occur within approximately one-tenth of matrix radius. The various shear-lag models available in the literature neglects this "boundary layer effect" observed in this study. At the debond crack tip, the smooth transition from a constant shear to zero shear occurs within about one matrix radius independent of the debond length, as generally expected from elasticity approaches using integral equations [42, 48-51, 54].

Figure 3.3 shows the different τ's obtained from the two different boundary conditions on the outer surface of composite cylinders. As expected, the results from traction-free boundary conditions and constant radial displacement/zero shear stress boundary conditions are in good agreement regardless of the debond length. The radial stress across the interface is also shown in Fig. 3.4, and it is of interest to note that the radial stress is rather small and neither uniformly compressive nor tensile. The results also show that the radial stress rapidly approaches the remote radial stress at the end of the slip zone. There is also a small cusp in the radial stress at the debond tip where formally there should be a small singularity.

In Fig. 3.5, we show the axial stress in the matrix at the outer radius $r=b$. Unlike the shear-lag solution, in which the axial stresses vary linearly with distance z from the matrix crack, the results show a slightly non-linear stress recovery. The far-field stress is,

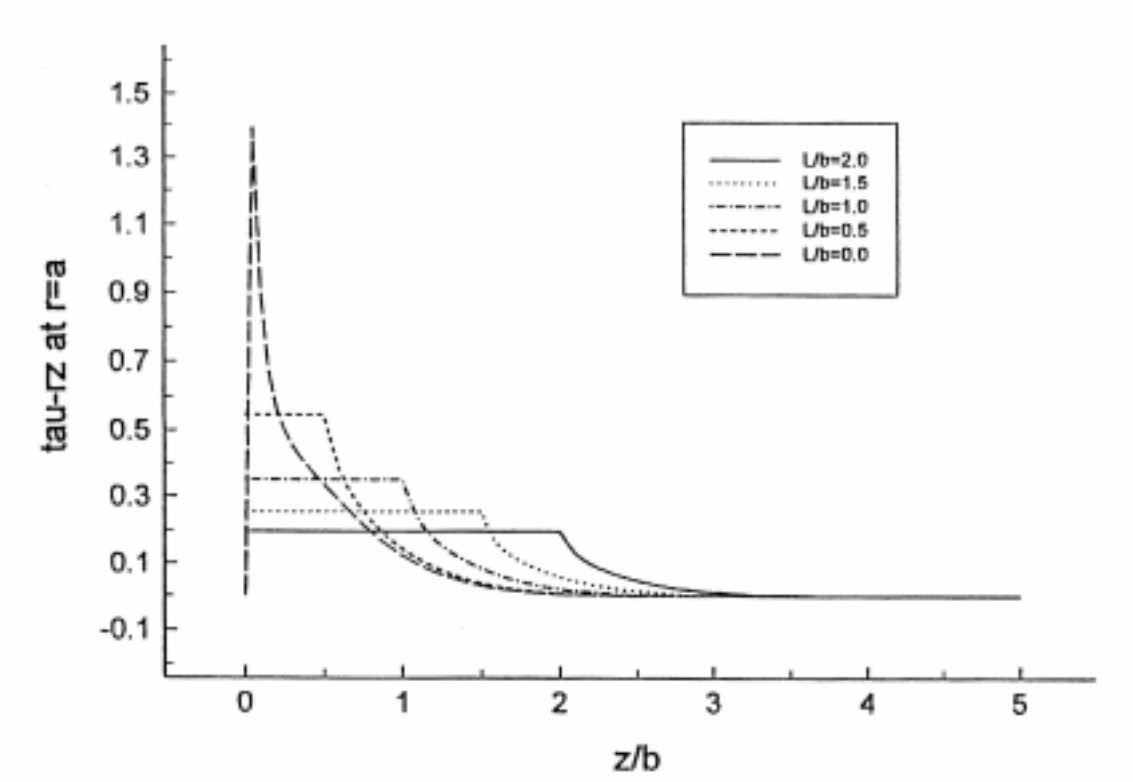

Figure 3.2: Interfacial shear stress versus axial displacement with various slip lengths. The stress is normalized by the remote axial stress in the matrix and the displacement is normalized by the outer radius *b* of the composite cylinder.

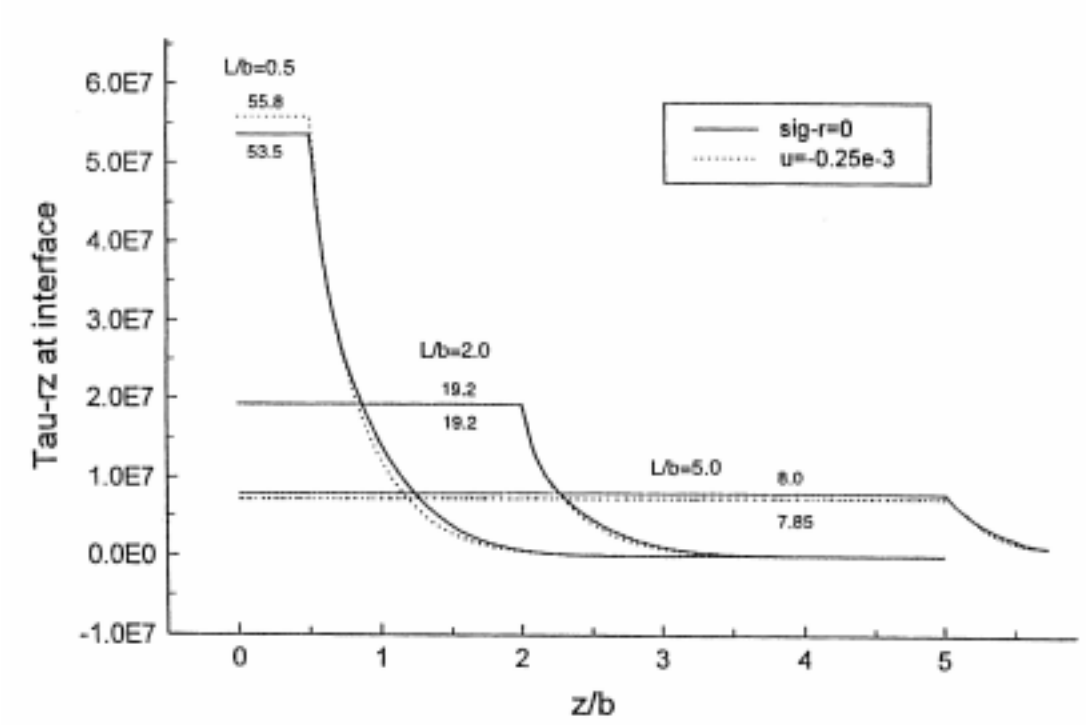

Figure 3.3: Interfacial shear stress vs. *z/b* from two different boundary conditions at *r=b*; traction-free b.c. (solid line), constant radial displacement and zero shear stress b.c. (dotted line).

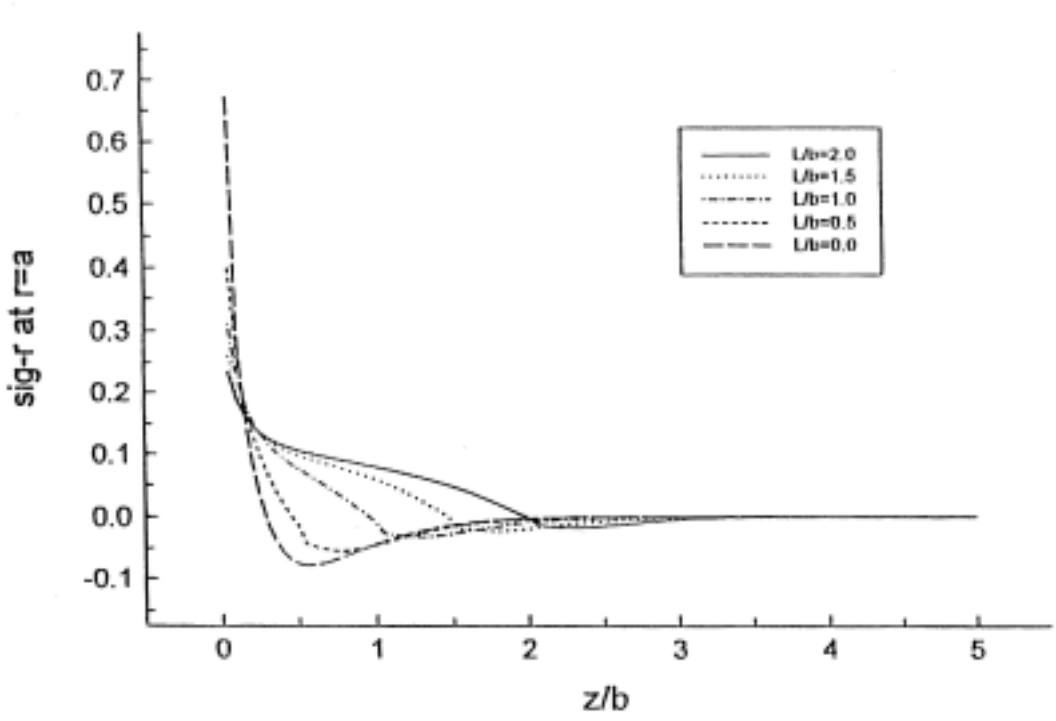

Figure 3.4: Interfacial radial stress vs. *z/b* with various slip lengths.

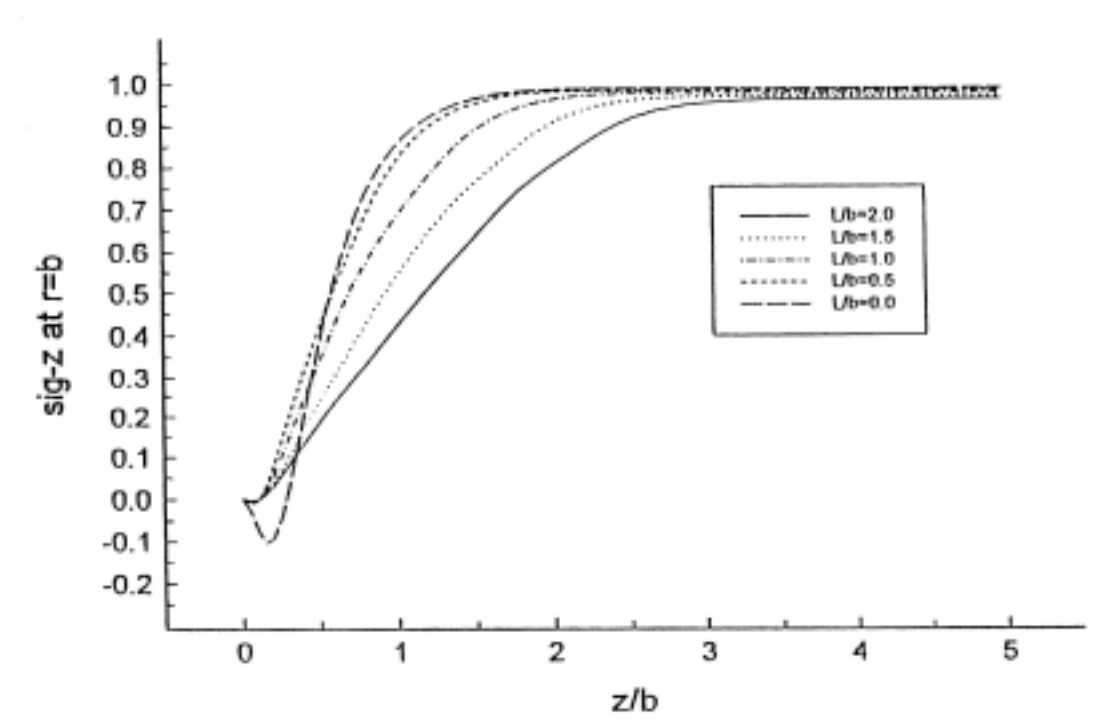

Figure 3.5: Axial stress in the matrix at $r=b$ vs. z/b with various slip lengths.

however, reached at essentially the point where the shear stress has decayed to near zero, as expected physically. Figure 3.6 shows the interfacial slip or the relative difference in displacement between the matrix and the fiber at the interface. The shear-lag solutions are also shown, for the corresponding L/b's, by dotted lines. For the shear-lag solutions, instead of fixing L/b, we used the same τ's as used for the ADM calculations to assess the change in the relative slip by the two different models. It appears that, for all L/b's, the relative slips by the shear-lag model are larger than the ADM results in the entire slip region and the difference in the slip by the two methods are rather constant in all cases studied. Both solutions predict a quadratic variation in the relative slip, which is well observed at large debond lengths. Wijeyewickrema and Keer [42] noted that the maximum slip occurs away from the crack plane and that peak decreased with increasing slip length. Unlike their stated observation, the maximum slip is seen to occur at the crack plane for all values of slip lengths investigated in this work and is seen to increase with increasing value of *L/b*. Related works by Kaw *et al.* [54] and Tandon and Pagano [55] show the same tendency as in the present study.

From the above results, we conclude as follows. The larger slip length results in lower shear stress in the slip zone, implying weaker bonding. In other words, the weaker bonding induces larger slip zone. Except for the boundary layer effect at the matrix crack plane and the nonlinear transition at the debond crack tip, which are confined to a very small region, the interface shear stress results are as expected from shear-lag model. The matrix axial stress results show the non-linear stress distribution, which the shear-lag does not include, but this effect also occurs within a small region comparable to a matrix radius. Therefore, the general idea of the shear-lag model regarding the interfacial shear stress and the axial stress in the matrix are considered to be acceptable.

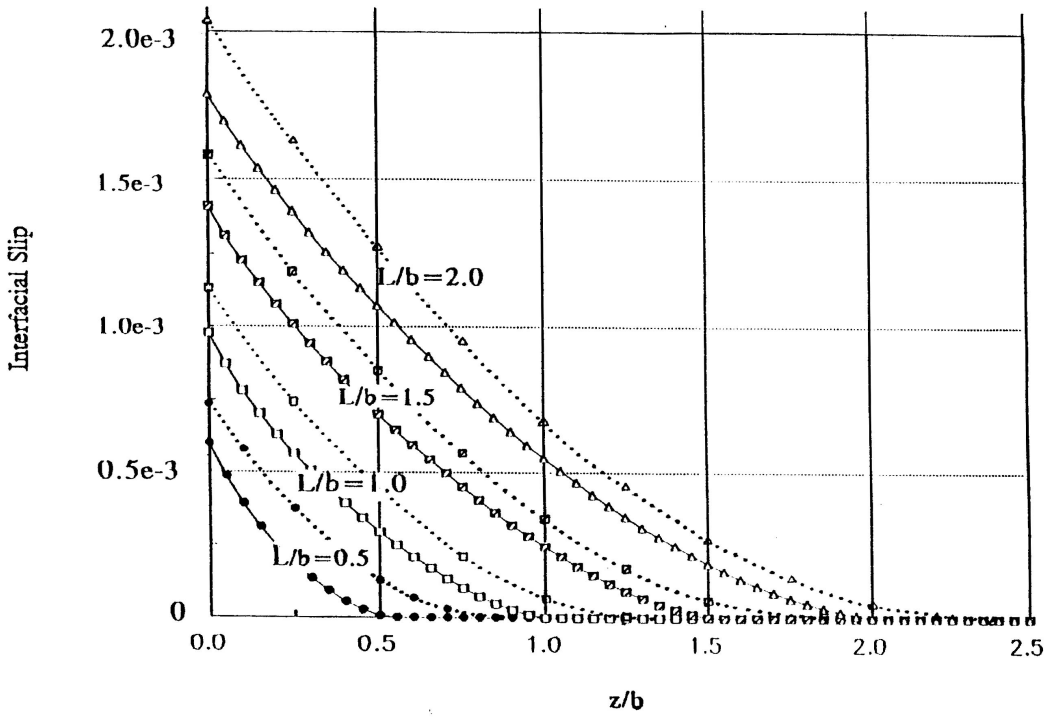

Figure 3.6: Relative slip at the interface vs. *z/b* with various slip lengths. (Solid lines - ADM results; Dotted lines - shear-lag solutions)

3.4. Matrix Stresses vs. Applied Loads

3.4.1. Problem Description

The second problem we are interested in is the relationship between the increasing applied loads and the axial stresses in the matrix. More specifically, we want to examine if the stresses in the slip zone would ever be sufficient to cause further matrix cracking in the slip zone. To this end, we obtain the matrix axial stress distributions using the ADM model, in particular, as a function of radial distance away from the fiber interface. Since the simple but widely-used shear-lag model we utilize in this study is not capable of handling the radial variation in the axial stress profiles, we are also interested in the degree of radial variation in this case.

The geometry for the problem is same as shown in Fig. 3.1. It consists of a matrix crack penetrating to the fiber surface and a debond crack along the interface. The constant sliding resistance has been chosen as 40MPa. Then, a guessed initial value of debond length L is chosen, and is adjusted to satisfy the boundary conditions including the shear stress continuity condition. This time, the constant radial displacement and zero shear stress boundary conditions (Eq. (3.10)) are used. The remote stresses applied on the composite ends are 100, 120 and 140MPa. Nicalon fiber and CVI-SiC matrix are used for the model composite, and the material properties used in the calculations are as follows.

Nicalon fiber : E_f=193 GPa, ν_f=0.15, α_f=3.11e-6/°C

CVI-SiC matrix : E_m=386 GPa, ν_m=0.147, α_m=4.5e-6/°C

3.4.2. Results/Discussion

We have examined the matrix axial stresses that are responsible for driving matrix cracks. Results for the matrix axial stress $\sigma_{zz}(z,r)$ are shown as a function of z at various radial locations r/a, measured in units of the fiber radius a, in Fig. 3.7a,b,c at remote applied stress levels of 100, 120 and 140 MPa. These results show that the axial stress is very nearly independent of the radial position over most of the debond slip length, which is in fact one of the main assumptions in shear-lag models. The stresses nearest to the fiber are slightly higher at the beginning and the end, due to the nearby presence of the matrix and debond crack tips, respectively. Comparing Fig. 3.7, it is evident that stresses in the slip region are essentially constant with increasing load. That is, increasing the slip length does not increase the matrix stresses in the slip region. Instead, as the applied stress increases, the slip length increases also: a longer distance is required for the axial stress to go from zero stress at the crack to the larger far-field stress.

In Fig. 3.7, the solid lines perpendicular to the z/a axis represent the slip length calculated from the shear-lag model with no thermal residual stresses or debond crack tip toughness involved. By setting the far-field stress in the fiber at $\sigma E_f/E_c$ when the axial distance z reaches the slip length δ in Eqs. (3.2) and (3.3), we obtain the following relations.

$$\delta = \frac{a\sigma}{2\tau}\frac{V_m E_m}{V_f E_c} \quad ; \quad E_c = V_f E_f + V_m E_m \tag{3.13}$$

where σ is the far-field applied stress. The linear solid lines, representing the stress profiles from the shear-lag model, can then be readily obtained from Eqs. (3.2) and (3.3). The simple shear-lag results appear to be around the average of the r-variant ADM results.

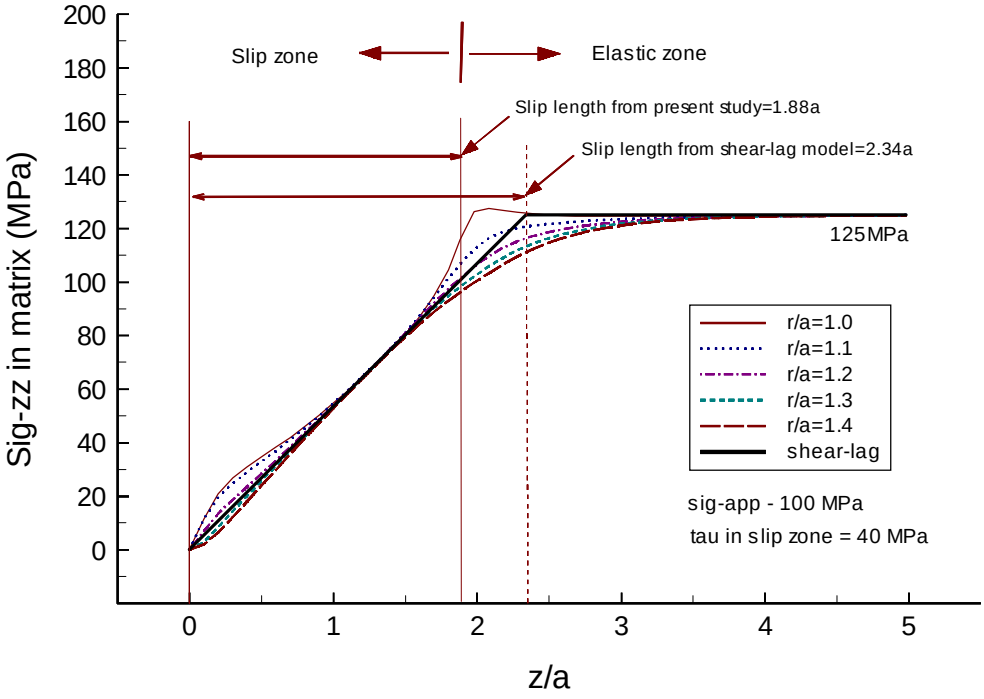

(a)

Figure 3.7: Axial stress profiles in the matrix vs. axial displacement (z/a) at various radial locations under increasing applied load; (a) σ_{app}=100MPa, (b) σ_{app}=120MPa, (c) σ_{app}=140MPa. The shear-lag solutions are denoted by solid lines and the slip lengths calculated from the shear-lag model are shown.

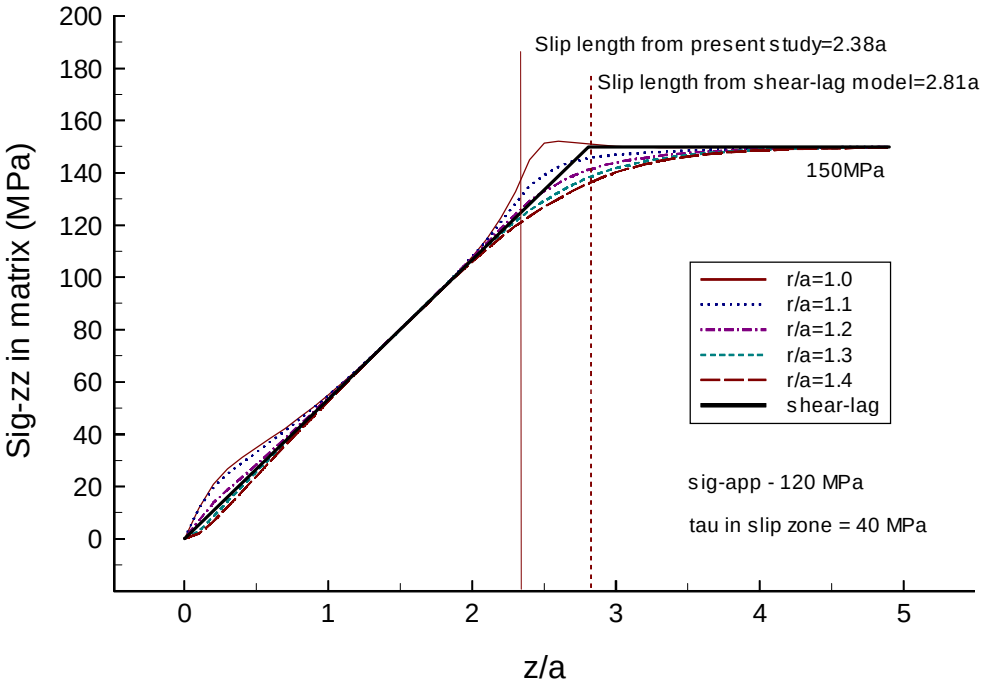

(b)

Figure 3.7 – *Continued.*

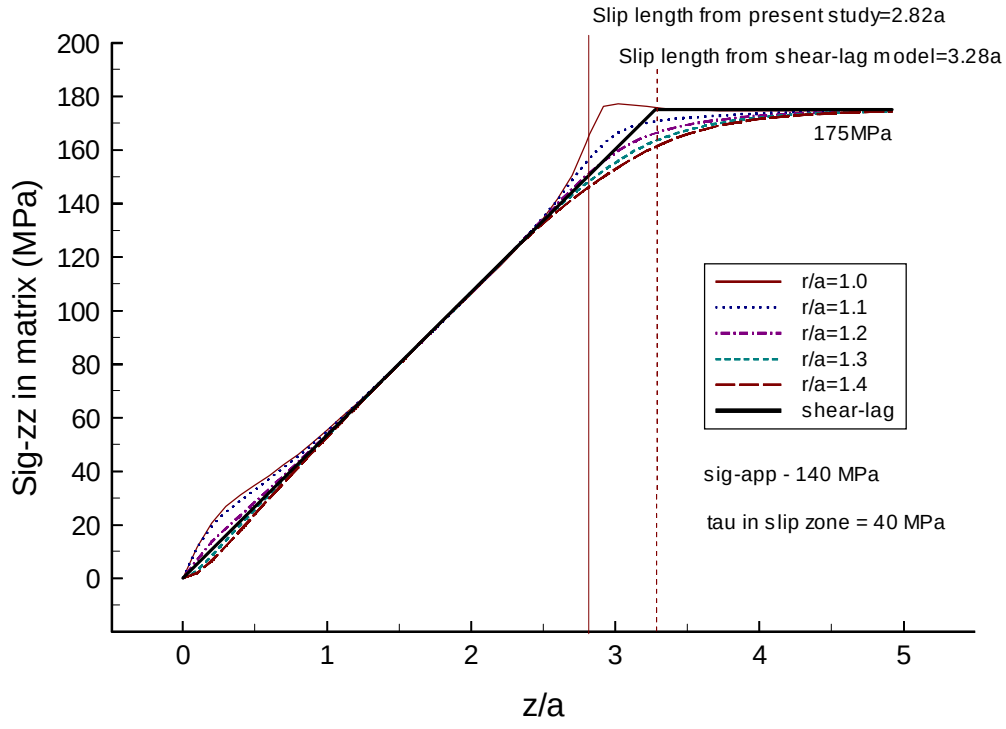

(c)

Figure 3.7 – *Continued.*

In general, the simplest shear-lag model neglects the elastic response just at the debond tip and so predicts a simple linear dependence of stress on distance from crack. The more accurate results presented here show that there is a small region ahead of the debond where the shear stress decays to zero which leads to a non-linear increase in the axial stress as the far-field value is approached. These results have actually been reported in the work in which the integral equation method is used, but the method requires solving complex boundary value problems and are not applicable to the mixed interface conditions such as the combinations of open zone and slip zone [42,49,50,54]. Aside from some minor variations, which could be approximately built into a more complete shear-lag analysis [43,64,65], most of the results for this problem are similar to those one would obtain from the simplest shear-lag analysis which we will use in the next Chapter. That is, our methodology using the ACK and BHE models to analyze the multiple matrix cracking phenomenon is believed to be acceptable.

Finally, we briefly mention another important fact regarding the issue of multiple matrix cracking, which we will need in the next Chapter. As shown in Fig. 3.7a,b,c, the matrix axial stresses are always below the far-field stress level, aside from a tiny elevation in stress just at the end of the debond for r/a=1.0. Since the matrix stresses are always below the far-field stress levels, the matrix will never crack again once it is within the slip/debond length of an already-existing crack. All of the cracks that occur must be out in the region of the far-filed stress. Multiple matrix cracking is thus driven by the far-field loading and not by the presence of prior cracks. In fact, the prior cracks exclude regions of the matrix from failing, and that is why the matrix cracking eventually stops at higher loads: the entire matrix is within a slip length of some crack and so cannot be loaded to the “far-field” level.

3.5. Stress Concentration in the Fiber

3.5.1. Problem Description

In a matrix-cracked composite with a debond crack along the interface, the next possible failure mode is either further matrix cracking or fiber breakage. In most CMCs, fibers are strong enough and/or interfaces are weak enough such that the fiber failure starts after matrix cracking comes to a saturation, but in some CMCs such as Nicalon/CAS composite it is observed that the fiber failure precedes further extensive matrix cracking. The particular phenomena may occur if the stress transferred into the fiber from the broken matrix exceeds the fiber strength. Considering the fiber flaws appear to occur more readily near the outer surface of the fiber, it is thus of interest to observe the stress distributions in the fiber.

In this Section, we are mainly interested in the axial fiber stresses in a composite having a matrix crack and a debond crack at the interface. Various values from 20MPa to 100MPa are assumed for the interfacial sliding resistance. Appropriate debond lengths are then determined by the procedure mentioned earlier, and the basic geometry of the problem is same as Fig. 3.1. Even though the detailed research in conjunction with the Weibull statistics of fiber strength is necessary to draw a conclusion on the fiber failure, the present study is expected to give an insight into the significance of the radial variations in the fiber stresses which may be responsible for the further cracking into the fiber in a matrix-cracked composite. Since the accuracy of the ADM results depend on the numbers and locations of the mesh-like layer elements, as discussed in the previous Chapter, several different layering sequences are considered. As usual in the stress analysis near crack tips, we add very thin layer elements in the vicinity of matrix crack tip to increase the accuracy of results.

3.5.2. Results/Discussion

Now we desire to investigate the details of the axial stress distribution within the "fiber". Various values are assumed for the interfacial sliding resistance in the debond zone. In particular, our results contain specific details of the stress distribution $\sigma_{zz}^{f}(r,z)$ in the fiber regions, which are required for predicting the ensuring fiber failure process. Results show that the fiber axial stresses become significantly large at the cross section of the matrix crack plane (z=0) and the interface (r/a=1.0) for all interface conditions studied. As mentioned earlier, this aspect is very important since the fiber flaws appear to occur more readily near the outer surface of the fiber.

In the ADM model, we fix the applied stresses at 100MPa, and studied three different τ's; 20MPa, 40MPa and 100MPa. Using the continuity of shear stress at the debond crack tip, the debond lengths are carefully determined at each of the applied stress level, to satisfy the given boundary conditions. The stresses are then examined at several radial locations, i.e. at the fiber center, at the fiber/matrix interface and several more locations in between. With a relatively small τ, as shown in Fig. 3.8a, the stresses are very linear and nearly independent of the radial locations for most of the debond region, and show stress concentration at z=0. In other words, unlike the axial stress profiles in the matrix, the stresses in the fiber do not converge onto a specific value at z=0. Note that the simple shear-lag model expects σ/V_f at z=0 (250MPa in the present problem) irrespective of the slip length. To assess the accuracy of the shear-lag model, the results from the model are shown with the linear solid lines; they are in very good agreement with an ADM result with r/a=0.8. It is also shown that, around the debond crack tip, there is slight difference in the ways for the stresses recover to the far-field stress at various radial locations.

The stress concentration at a specific location seems more critical at the higher τ as shown in Fig. 3.8b and c. In Fig. 3.8b, the fiber axial stress at (z=0, r/a=1.0) is around 390MPa which is 140MPa larger than the "average" fiber stress calculated by the shear-lag model. In Fig. 3.8c, the corresponding stress increases up to 590MPa. This stress concentration aspect was described in detail by Weitsman and Zhu [69] on the

recognition that the fiber may be easier to break than expected from the shear-lag model. In Fig. 3.8b,c, it is also notable that the slip lengths substantially decrease compared to the previous case of τ=20MPa in Fig. 3.8a and the linear portions of the slip zones become considerably small.

It is still unclear, however, the maximum stress obtained here is the real maximum. Considering the accuracy of the ADM model depends on the additional layer elements near stress concentration-related locations, we should be careful to select the proper layering sequences. For the results shown in the Fig. 3.8a,b,c, the layers used are at r/a=0.1, 0.2, 0.3,.0.4, 0.5, 0.6, 0.7, 0.8, 0.9, 1.0, 1.1, 1.2,.1.3, 1.4, and 1.5. This configuration should be good enough to obtain the general stress profiles away from the interface, but near the interface some more thin layers are needed to obtain accurate solutions. Thus, we have added more layers in addition to the layers shown above: (i) at r/a=0.85, 0.95; (ii) at r/a=0.85, 0.94, 0.97; (iii) and at r/a=0.85, 0.94, 0.97, 0.99, and 0.998. Generally speaking, the best choice of the minimum layer thickness would be the flaw size in the fiber, and here we provide the attainable results using the random layers.

Note that the thinnest layer used in (iii), 0.002a, is the smallest possible layer thickness without computational problem in the ADM model.

The stress results using (iii) layers are shown, for comparison, by dots in Fig. 3.8a,b,c. The results show that the differences in the observed stresses are measurable only near the interface and at the matrix crack plane. In the other region, the stresses are not essentially dependent on the mesh refinement. From strength perspective, these results imply that when a matrix crack is followed by a debond crack at the interface, the fiber most likely breaks near the interface and along the matrix crack plane. It should be noted, however, that in the present study, we enforce the shear stress continuity at the debond crack tip to solve the boundary value problem. Provided that the stress continuity is not satisfied at

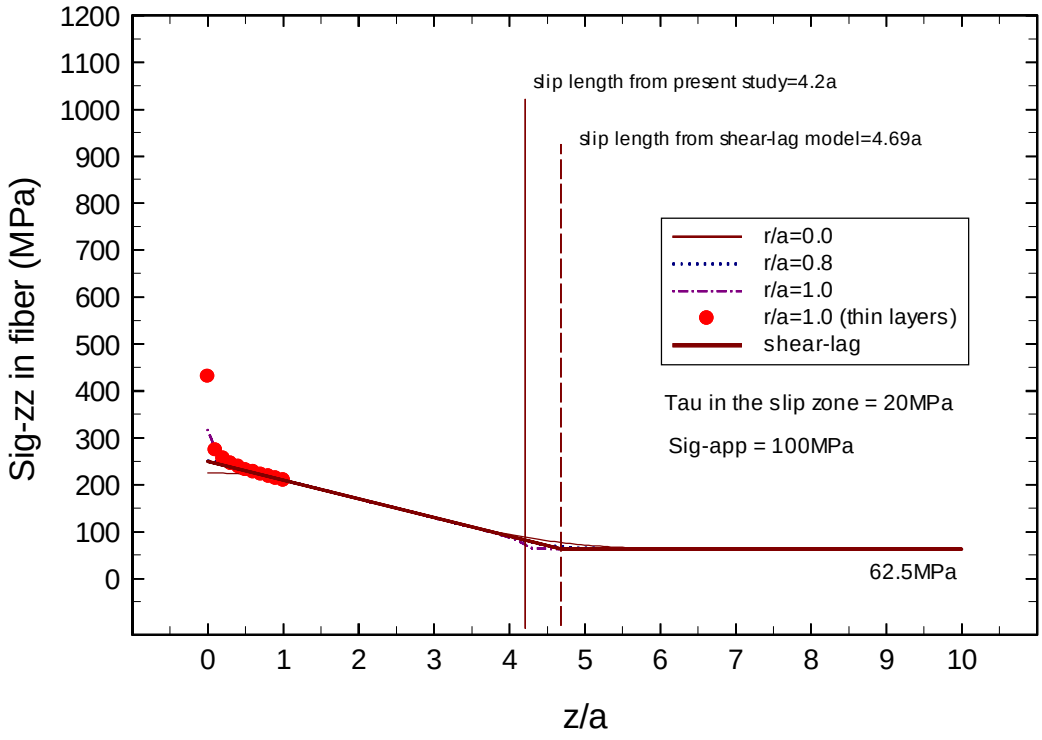

(a)

Figure 3.8: Axial stress profiles in the fiber vs. *z/a* at various radial locations with various sliding resistance; (a) τ=20MPa, (b) τ=40MPa, (c) τ=100MPa. Shear-lag solutions are shown with solid lines.

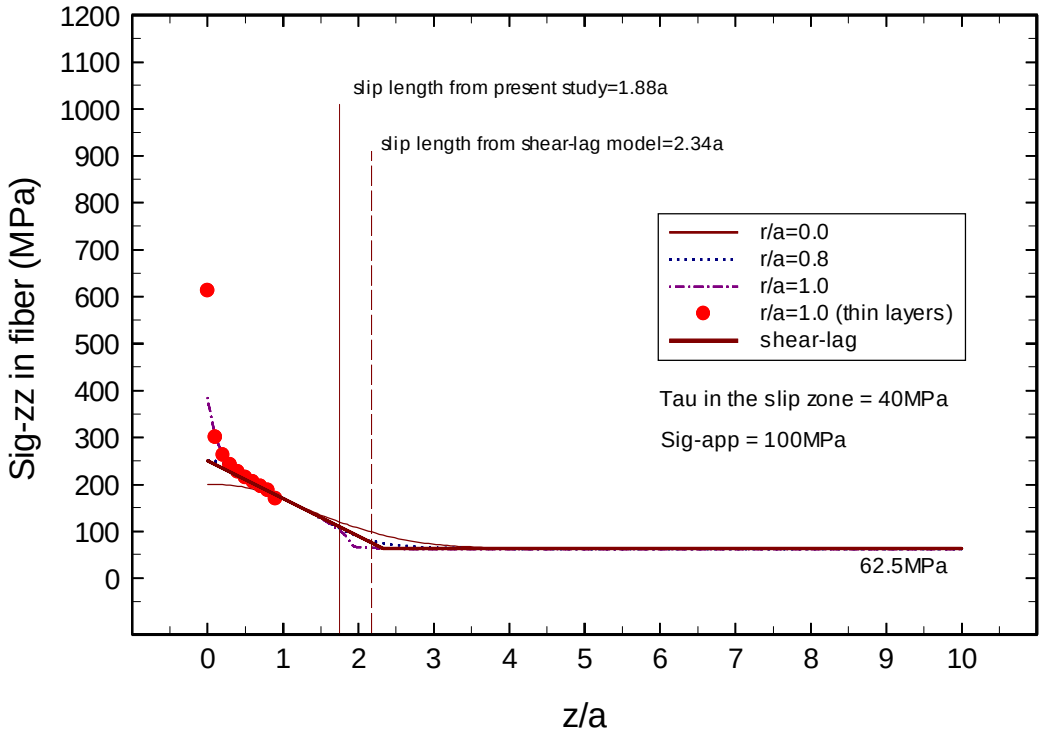

(b)

Figure 3.8 – *Continued.*

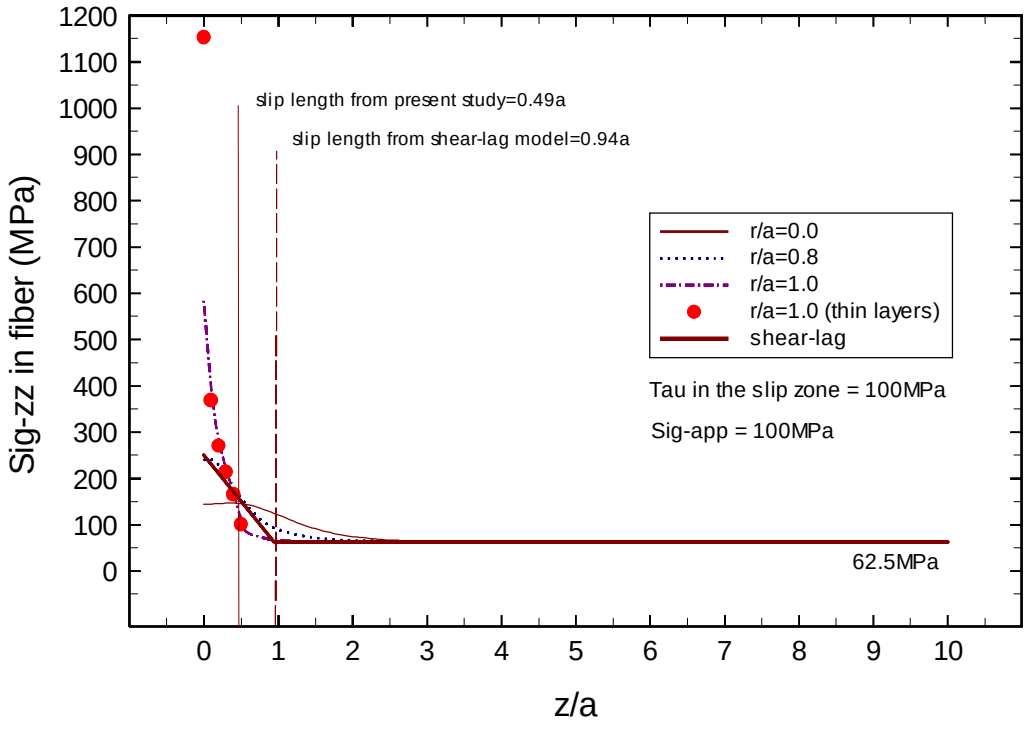

(c)

Figure 3.8 – *Continued.*

the debond crack tip, then another feasible location for fiber break might be somewhere else such as near the debond crack tip and along the interface. This issue is left for future study.

We have shown that in any of the possible layering configurations, the stress concentration occurs within a very small region compared to the composite length. We thus believe that the enhanced fiber stress along the matrix crack plane will not affect the overall stress/strain relations of the composite. Along with the conclusion of the previous Chapter, we then conclude the shear-lag model is accurate enough to evaluate the stress/strain behavior in a CMC in which matrix cracking with an interfacial slip occurs.

3.6. Summary

We have discussed the microstress distribution in a composite which has an annular matrix crack and a debond crack along the interface.

Comparison of our results to the shear-lag solutions shows that the accuracy of the shear-lag approximation is acceptable to calculate the interfacial shear stress and matrix axial stress even though the model ignores the radial variation in the axial stress. Another important assumption in the simple shear-lag model is that the shear stress in the slip zone drops to zero linearly at the debond crack tip. Our results show the shear stress decays nonlinearly as shown in Fig. 3.2, but the decay zone is within the length of fiber diameter; this should not invalidate the accuracy of the shear-lag model. Furthermore, the modified shear-lag model considering the adhesion effect confirms the non-linear behavior in the stress distributions [43].

However, the validity of the shear-lag model is somewhat uncertain when the fiber stress becomes a problem issue. The axial fiber stress seems to diverge and the stress is enhanced/concentrated on the fiber surface along the matrix crack plane. The most likely place for fracture would be at the matrix crack line but the statistical distribution of flaws

in the fiber could induce fiber fracture to occur elsewhere. It should be noted again, however, that the stress concentration does not affect the total stress/strain relations of the composite. We have not discussed here, but for the purpose of protecting the fibers, fiber coatings have been known to play an important role to redistribute the stress into the fibers as well as the coating itself [70-73]. A stiff coating carries big load and reduces the stress concentration in the fibers while soft coating would have an opposite effect. Thus, the choice of the coating materials should be made in connection with fiber materials and interfacial condition. However, it should not be neglected that the coating materials also may fail at some load level and again the stress may concentrate on the fiber surface. As one of the promising ways to minimize the fiber failure by the concentrated load (or by chemical reaction at the interface exposed to the environment through the matrix cracks), employing the multi-layer coatings have been brought to attention [74, 75].

As a future plan, we will investigate the detailed stress distributions in the constituents and at the interface of composite in which "multiple" fiber coatings are incorporated. The fiber is assumed to slip at the fiber/inner coating interface with a constant slip resistance, τ. The effect of the slip length and the effect of the magnitude of τ on the stresses will be of interest. These studies will be necessary because a quantitative determination of crack evolution in multilayer coating systems must be as accurate and realistic as possible. Another important issue is of the interface toughness which causes the corresponding jump in the axial stresses at the debond crack tip. Considering this problem will be necessary for more complete understanding of the interface with slip.

Chapter 4. MULTIPLE MATRIX CRACKING

In the previous Chapter, we studied the stress distributions around a sliding interface. An annular main matrix crack was assumed to deflect into the fiber/matrix interface and develop a slip zone in which a constant slip resistance was prescribed. Under increasing tensile loading, this slip zone grows and other additional matrix cracks can propagate. The extensive further matrix cracking, or multiple matrix cracking, is known to be the first nonlinear event which occurs prior to the failure of fibers in most CMCs. In this Chapter, we develop a theory to predict the stress/strain relations and unload/reload hysteresis behavior during the evolution of multiple matrix cracking. The theory is based on the similarity between multiple matrix cracking and fiber fragmentation in a single fiber composite, and determines the crack and strain evolution as a function of the statistical distribution of initial flaws in the material, the interfacial sliding resistance τ, and the thermal residual stresses in the composite. The model properly includes matrix fragments of all lengths, from lengths smaller than the current slip length $\delta(\sigma)$ to larger than $2\delta(\sigma)$, at applied stress σ, and accounts for their respective and differing contributions to the overall strain and hysteresis behavior of the composite. To derive the fiber-controlled strain behavior from the stress distributions in the cracked-matrix, we use the shear-lag model whose usefulness for the present problem was already confirmed in Chapter 3. We also present a procedure for obtaining the interfacial sliding resistance, thermal stresses and intrinsic flaw distribution from the experimental stress/strain and hysteresis data. This approach is very convenient and simple for high temperature applications since the actual physical crack spacing needs to be determined at one load level such as post-fracture. Several detailed examples are presented, and the results compared with a widely-used approach in which the crack spacing is assumed constant and equal to the average spacing obtained directly from experiment. The discrepancy between the previous and present theories is manifest in an incorrect estimate for the interfacial sliding, but only by approximately 10%. The effect of changing temperature, and hence residual stresses, without changing either matrix flaws or interfacial sliding resistance, is studied.

4.1. Introduction

It is now well established that the extensive multiple matrix cracking in ceramic matrix composites is a dominant event in the performance of these materials. The beneficial effect occurs because the cracks cause the inelastic strain behavior in unidirectional fiber-reinforced CMCs and the nonlinear strains are responsible for the toughness and damage tolerance in these materials [78] as well as the notch insensitivity [79].

As briefly discussed in the Introduction with Fig. 1.2, the onset of matrix cracking is well understood since the study of Aveston *et al.* (ACK) [38]. The matrix cracking first occurs at the stress σ^*-σ_{th}, where σ^* is the "ACK stress" which will be shown in the next Section, and σ_{th} is the thermal residual stress in the composite due to the thermal mismatch of the fiber and matrix. Before the onset stress is reached, the composite shows linear elastic stress/strain relations. In the intermediate stress range between the onset stress and matrix cracking saturation stress, σ_s, numerous matrix cracks are formed, leading to substantial reduction in composite tangent modulus. At higher stress than σ_s, fiber failure becomes appreciable, culminating in composite failure when sufficient fiber damage has accumulated such that the damaged composite cannot sustain any further load.

Aveston, Cooper and Kelly [38] were the first to consider the onset stress of matrix cracking at which first matrix crack appears in a unidirectional fiber-reinforced CMCs. They made an energy balance analysis of a composite consisting of unidirectionally aligned, continuous fibers, in a matrix whose failure strain is less than that of the fibers. The ACK analysis shows that the matrix failure strain is enhanced by the presence of fibers and that the matrix will be traversed by a series of more or less parallel cracks and perpendicular to the fibers. Later, Aveston and Kelly [60] modified the original ACK model by considering the imperfect interface in which case partially and fully bonded interfaces are included. Budiansky, Hutchinson and Evans (BHE) [40] analyzed the

steady state cracking in CMCs including friction and residual stresses. The BHE model considers two types of interfaces: (i) unbonded fibers, held in the matrix under thermoelastic mismatches, but subject to frictional sliding; (ii) a weak fiber/matrix interface which becomes debonded under the action of stresses at the crack tip in a matrix. Like the ACK model, the BHE model predicts that the matrix cracking strain will be higher than that of the unreinforced material above a certain volume fraction of fibers. Marshall, Cox and Evans (MCE) [41] subsequently determined the crack growth conditions for smaller size cracks using a bridging approach.

Understanding of matrix cracking phenomenon is also a valuable means for determining the in-situ fiber/matrix interfacial quantities which are directly relevant to composite strength and work-of-fracture. To measure the interfacial properties experiments such as the push-in or indentation test [66,68] and pull-out test [67] have been devised. Marshall [66] used a specimen which was very thick compared to the fiber radius, and proposed a test method to calculate the "constant" frictional stress at the fiber/matrix interface from the measured fiber load and relative slip. Takaku and Arridge [67] explored the possibility of Coulomb type interface friction by using a pull-out test and a modified shear-lag model that accounts approximately for the alteration in the interfacial normal stress which accompanies Poisson contraction of the pulled fiber. This modified shear-lag analysis was adapted by Shetty [68] to the case of the fiber being pushed instead of pulled. However, all these methods test individual fibers, whereas average values over many fibers are relevant to the overall composite behavior. Moreover, the approaches require special sample preparation, and can be difficult to perform at elevated temperatures.

The limitations mentioned above have motivated more recent works on determining τ from the composite stress/strain behavior, hysteresis on unloading and reloading, and the measured crack spacing as matrix cracking evolves. Pryce and Smith (PS) [80] used the ACK analysis and presented a micromechanics model to obtain τ and the thermal residual stress from the stress/strain relations and hysteresis of a cracked composite under quasi-static loading and fatigue cycling. Experimental data including crack density and

residual strain were associated with the development of matrix cracks in unidirectional continuous SiC fiber/CAS matrix laminates. Pryce and Smith accounted for the crack interactions by defining the stress at which the crack spacing becomes equal to the slip length. However, the model assumed that the crack spacings are equal and uniform at a given stress level, which is widely accepted but not true. Vagaggini *et al.* [81] developed a similar methodology for assessing τ, thermal stress and interfacial debond energy Γ_i, from stress/strain curves and hysteresis loops. While the work by Vagaggini *et al.* presented a theoretical model, the companion paper by the same authors showed the experimental results for two composite material systems, SiC/SiC and SiC/CAS [82]. They compared their results to those from the pull-out and push-in tests and showed a relatively good agreement in SiC/CAS composite. The main drawback of these works was that they did not consider the crack interactions or the overlaps of the neighboring sliding zones.

The method using a single fiber microcomposite suggested by Morscher *et al.* [83] provided a useful test for understanding the mechanical properties of fiber/matrix interfaces, without fabricating large composites, for a number of stress/temperature conditions. They used load/displacement hysteresis data and acoustic emission (AE) test to determine the interfacial shear properties of thin carbon and boron nitride (BN) coatings in SiC-CVD/SiC-CVD composites. Optical and electron microscopy were also performed to confirm the extent and nature of the matrix cracking and to analyze the microcomposite microstructure. Lamon *et al.* [84] used a similar technique to evaluate the interfacial sliding resistance of various interphase coatings containing carbon and BN in Nicalon/SiC-CVD matrix composite systems. They adopted the analysis of fiber debonding and sliding by Marshall [85], which was based on the work of Hutchinson and Jensen [63], to determine the interfacial properties for microcomposites where a compliance change was noticeable as a result of matrix cracks.

Although there have been many reported works regarding the methodology of obtaining the interfacial properties of CMCs with a matrix crack or multiple matrix cracks, most of them do not properly account for the two very important aspects of multiple matrix

cracking: mechanics aspects and stochastic aspects; the former aspect refers to the interactions between cracks while the latter pertains to the role of the distribution of matrix flaws which ultimately governs the spatial distribution of matrix crack. In other words, most studies have ignored the actual spacing distribution and the interference between cracks, or have focused on arrays of equal-spaced matrix cracks. However, since matrix cracking ceases only when the density of matrix cracks is sufficiently high that the slip of fibers relative to the matrix occurs over a distance comparable to the matrix crack spacing, interference between crack slip zones is clearly important. The spatial distribution of cracks then also implies that interference occurs prior to the end of matrix cracking as well.

Zok and Spearing [86] were one of a few who made efforts to assess the stochastic aspects of matrix cracking. Yang and Knowles [88] and Curtin [77,78] are among others. Zok and Spearing calculated the strain energy release rates for matrix crack growth with interference from neighboring crack slip zones, and performed numerical simulations of the crack evolution from their results, combined with an assumed initial flaw distribution. The model seems to be the proper one when all the initial defects are larger than the characteristic initial crack size, but is not completed for small cracks which may exist when the range of cracking stress is rather broad. Spearing and Zok [87] incorporated the effect of bridging fibers on the stress required for matrix cracking and conducted a computer simulation of multiple cracking with emphasis on the role of the matrix flaw distribution and the crack interactions. Yang and Knowles [88] also simulated stochastic crack evolution using a 3-parameter Weibull flaw distribution. They applied the car parking problem to the matrix crack spacings and showed that there is a distribution of matrix crack spacings within a unidirectional brittle matrix composite, rather than just a single average value. Curtin [77] verified that there is a strong similarity between fiber fragmentation in the single fiber composite (s.f.c) and multiple matrix cracking, and solved the full statistical problem of multiple matrix cracking within the context of the s.f.c. fragmentation. In a later work, Curtin [78] used the extremely accurate solution to predict the evolution of multiple matrix cracking in brittle matrix composites, and analyzed data on Nicalon/CAS CMCs to evaluate τ from experimental measures of the

fraction of breaks vs. stress and the final crack spacing. However, none of these workers predicted the stress/strain or hysteresis behavior, and they have not correlated their predictions with other measurements of interfacial sliding resistance in CMCs; this has motivated our present study.

In this Chapter we extend the analysis of Curtin [78,79] to determine the detailed stress/strain behavior and hysteretic unload/reload behavior caused by the presence of stochastically distributed matrix cracks. The behavior is completely described by the thermal residual stress and three other parameters associated with the underlying strength of the fiber-bridged matrix flaws: the minimum cracking stress σ^*; a characteristic stress σ_R around which cracking occurs; and the Weibull modulus ρ describing the statistical distribution of matrix flaw strengths around the stress σ_R. The analysis of crack evolution does not assume equally-spaced matrix cracks, and is inherently statistical, but the determination of the deformation characteristics follows from straightforward application of shear-lag solutions for the matrix and fiber stresses around the matrix cracks. The validity of the shear-lag model for the present problem was proved in the previous Chapter. We also emphasize the inverse procedure of measuring the deformation behavior and then utilizing the theory to back-out values for the critical parameters in the theory, and subsequently the interfacial sliding resistance.

The remainder of this Chapter is organized as follows. In Section 4.2, we discuss in more detail the theories which will be used in the present analysis. In Section 4.2.1, we first describe the basic mechanics important to the matrix cracking phenomenon. In Section 4.2.2, we determine the composite strain for a given arbitrary distribution of matrix cracks at some applied composite stress, by explicitly considering the stress profiles in fibers adjacent to the cracked matrix for all possible matrix crack spacings. In Section 4.2.3, we similarly analyze unloading and reloading to obtain a complete hysteresis loop. A popular previous analysis, first described by Pryce and Smith (PS), is also introduced. In Section 4.2.4, we then discuss the underlying statistical parameters that will drive matrix cracking and provide the scale parameters for the actual crack spacing distributions obtained in materials. In Section 4.3, we apply the present theory and the

PS theory to several cases and compare the results of the two approaches to assess the discrepancies in derived τ from the use of the simpler PS model. In Section 4.4, we demonstrate the detail steps to obtain τ using the statistical parameters σ_R and ρ, the ACK stress σ^*, and the composite thermal stress σ_{th}. Section 4.5 contains further discussion and comparison of the present theory to previous approaches. In the Appendix B, we present the details of the calculation of the evolution of the matrix crack spacing, as discussed previously by Curtin [78], Neumeister [89], and Curtin and Zhou [90] in a related context.

4.2. Theory

4.2.1. Mechanics of Matrix Cracking

Prior to any cracking, the ceramic matrix composite under tensile longitudinal load σ has equal strains in the matrix and fiber constituents, and the stress/strain behavior is purely linear elastic. The average axial stresses at longitudinal position z satisfy the equilibrium equation

$$\sigma_f(z)V_f + \sigma_m(z)V_m = \sigma(z) \tag{4.1}$$

and the individual fiber and matrix stresses are independent of z

$$\sigma_f = \sigma\frac{E_f}{E_c} + \sigma_f{}^T \quad ; \quad \sigma_m = \sigma\frac{E_m}{E_c} + \sigma_m{}^T \tag{4.2}$$

where E_f, V_f and E_m, V_m are the Young's moduli and volume fractions of fibers and matrix, respectively, and $E_c = V_f E_f + V_m E_m$ is the composite modulus. In Eq. (4.2), σ is the applied stress, while σ_f^T and $\sigma_m{}^T$ are the thermal stresses in the fiber and matrix, respectively [91].

$$\sigma_f^{\,T} = E_f E_m V_m (T_0 - T)\left(\alpha_f - \alpha_m\right)\Big/ E_c \quad , \tag{4.3}$$

$$\sigma_m^{\,T} = -E_f E_m V_f (T_0 - T)\left(\alpha_f - \alpha_m\right)\Big/ E_c \quad . \tag{4.4}$$

In Eqs. (4.3) and (4.4), T_0 is the stress-free temperature, T is the operating temperature, and α_f , α_m are the thermal expansion coefficients of fiber and matrix, respectively.

The growth of fiber-bridged matrix cracks in a unidirectional composite has been discussed in considerable detail by ACK and BHE for large initial flaws, and by MCE for smaller size cracks. The ACK and BHE results show that the onset stress is given by σ^*-σ_{th} where

$$\sigma^* = \left[\frac{6\tau \Gamma_m V_f^{\,2} E_f E_c^{\,2}}{V_m E_m^{\,2} r_f} \right]^{1/3} \tag{4.5}$$

and

$$\sigma_{th} = \sigma_m^{\,T} \frac{E_c}{E_m} = -\sigma_f^{\,T} \frac{V_f E_c}{V_m E_m} \quad . \tag{4.6}$$

In Eq. (4.5), r_f is the fiber radius, and Γ_m is the matrix fracture energy. We will focus here not on the conditions under which cracks can propagate but rather on the stresses around the matrix cracks after propagation.

The first matrix crack appears at an applied stress equal to or larger than the onset stress σ^*-σ_{th}, and is accompanied by debonding and interfacial slip along the fiber/matrix interface. In this work, we assume that the fiber/matrix interface has zero debond energy; this assumption can be relaxed after we understand the detailed influence of stochastic cracking on the deformation in the simpler case of zero debond energy. The basic equation of equilibrium for the fiber dictates that the average axial stress in the fiber a distance z from the matrix crack satisfies

$$\sigma_f(z) = \frac{\sigma}{V_f} - \frac{2}{r_f}\int_0^z dz\,\tau(z) \quad . \tag{4.7}$$

Taking the interfacial shear stress τ to be constant along the slipping portion of the fiber, slipping occurs over the length necessary for the fiber axial stress to recover to the far-field, pre-cracked value. The slip length δ at applied stress σ is then simply

$$\delta = \frac{r_f}{2\tau}\left[\sigma\frac{V_m E_m}{V_f E_c} - \sigma_f^T\right] = \frac{r_f}{2\tau}\alpha\left(\sigma + \sigma_{th}\right) \tag{4.8}$$

where

$$\alpha = \frac{V_m E_m}{V_f E_c} \tag{4.9}$$

and the fiber stress within the slip region is

$$\sigma_f(z) = \frac{\sigma}{V_f} - \frac{2\tau z}{r_f} \quad , \qquad z<\delta \quad . \tag{4.10}$$

At the crack plane, the fiber stress is σ/V_f because all the applied stress is carried by the fiber and the thermal stress σ_f^T is released at this location. δ is the slip length at which slippage no longer exists and the fiber and the matrix extend compatibly. For $z>\delta$, the far-field stress (Eq. (4.2)) obtains.

The average axial stress in the matrix $\sigma_m(z)$ is obtained by the equilibrium equation (Eq. (4.1)), and the slip length δ is the same as that for the fiber. The stress in the matrix thus recovers linearly from zero to the pre-cracked value $\sigma_m = \sigma E_m/E_c + \sigma_m^T$. Within $\pm\delta$ from the first matrix crack, the matrix stress is now no longer high enough to allow further matrix cracking to occur, and thus an "exclusion" zone forms around this crack. With increasing applied stress, further matrix cracks can occur initiating from "weak" flaws in the matrix, as long as those flaws are not in the exclusion zones established by the previous matrix cracks. A crack which occurs near previous cracks, but necessarily

outside their exclusion zones, can have slip zones which overlap with the slip zone around one or both of its neighbors. When this occurs, the stress in between the two matrix cracks can not build up to the far-field value and so future cracking in this region is then forbidden, forming a permanent, unchanging matrix fragment in the composite. The evolution of multiple matrix cracking with increasing σ finally approaches the saturation state when all the crack spacings are shorter than twice the slip length $2\delta(\sigma)$; the matrix stress cannot recover to the pre-cracked value anywhere. A schematic of the evolution of matrix stress is illustrated in Fig. 4.1. The evolution of matrix cracking is similar to that of fiber fragmentation in the single fiber composite, and the description of the evolution of fragments in these cases has been previously described in some detail.

Particularly pertinent to our discussion here is that during matrix crack evolution overlapping slip regions occur for "fragments" (crack spacings) which are smaller than $2\delta(\sigma)$. The stress profile in the fiber is, nonetheless, still determined by the equilibrium equation but the slip extends over the entire fragment with one half of the fragment having negative shear stress and the other half having positive shear stress. It turns out to be convenient both in the calculation of matrix crack evolution and in the assessment of unload/reload behavior to divide the matrix crack fragments into three distinct categories: "long" fragments, $x>2\delta(\sigma)$; "medium" fragments, $\delta(\sigma)<x<2\delta(\sigma)$; and "short" fragments, $x<\delta(\sigma)$. The spatial distributions of shear stress, fiber and matrix axial stresses on loading up to composite stress σ are shown in Fig. 4.2. The "long" fragment case corresponds precisely to the results of Eq. (4.2) above.

4.2.2. Strain Evolution on Loading

In the present study, our interest lies in the stress/strain behavior in the stress range of $[\sigma^*-\sigma_{th},\sigma_s]$. We assume these loads are not sufficient to cause fiber failure such that the fibers remain intact throughout matrix cracking. As a consequence, the strain associated with any section of composite is precisely the strain in the fibers, because the

fibers are deforming elastically with modulus E_f in response to the (spatially-varying) axial stress field.

Imagine now that loading has proceeded up to some level σ and that the matrix crack spacing distribution *P(x)* is given to us at this stress. We endeavor to calculate the strain associated with this configuration of cracks and at this load. As noted above, the strain in the composite is that of the fibers, and hence the composite strain is the average strain in the fibers,

$$\varepsilon_c = \frac{1}{L_T E_f} \int_0^{L_T} dz\, \sigma_f(z) \tag{4.11}$$

where L_T is the composite length. Strictly speaking, the axial stress in the fiber depends on the radial location, *r*, from the fiber center and shows stress enhancement along the matrix crack plane. However, as shown in the previous Chapter, the stress concentration is refined to a very small region and is negligible for the strain calculations here. Then, the stress in a fiber at point *z* depends only on the fragment size *x* in which *z* is contained. Given the fragment distribution *P(x)*, we can thus recast the above integral into an integral over all of the fragment lengths *x* as

$$\varepsilon_c = \frac{1}{L_T E_f} \int_0^{\infty} dx\, P(x) \int_0^{x} dz\, \sigma_f(z) \quad . \tag{4.12}$$

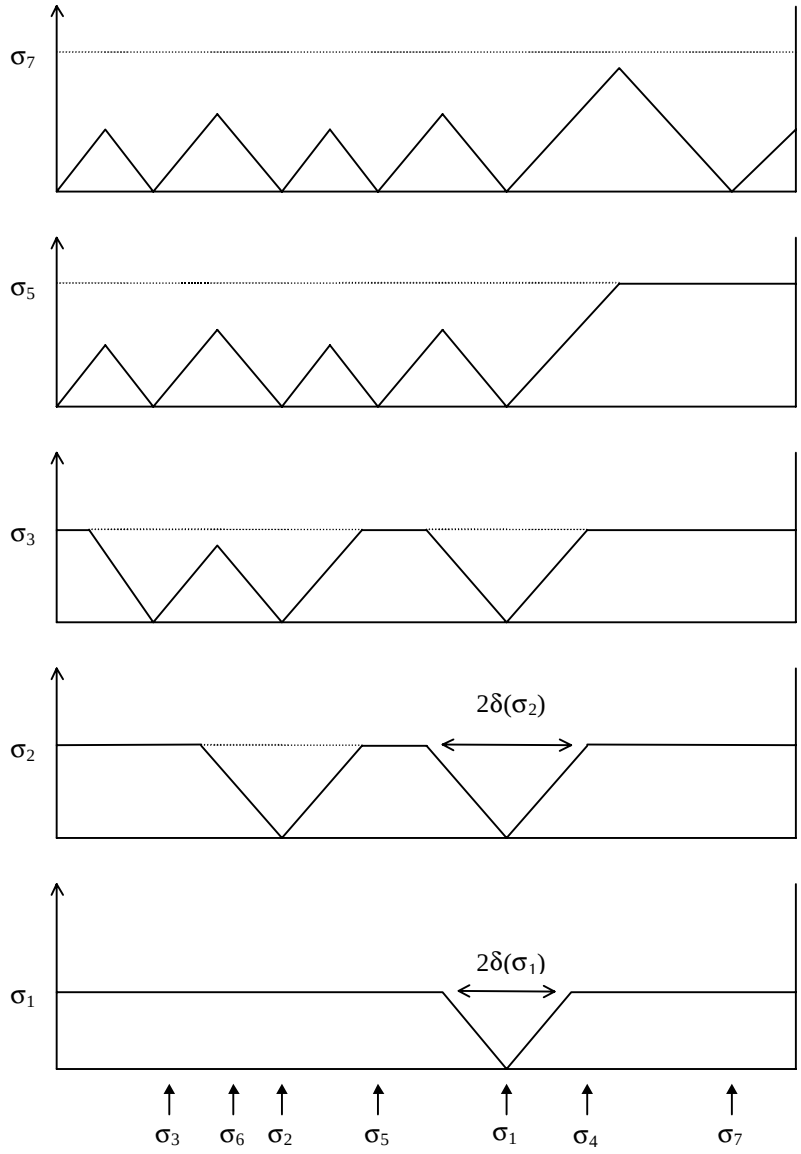

Figure 4.1: Schematic evolution of matrix stress during multiple matrix cracking with increasing applied matrix stress. The spatial location of the 7 weakest defects, of strengths $\sigma_1, \ldots, \sigma_7$, are shown.

The fragment distribution naturally divides into three parts associated with the long, medium, and short length fragments, $P(x)=P_S(x)+P_M(x)+P_L(x)$. Because the short, medium, and long fragments fall into distinctly different lengths, we can then write the strain as the sum of three separate contributions,

$$\varepsilon_c = \frac{1}{L_T E_f}\left[\int_0^{\delta} dx P_S(x)\int_0^{x} dz\sigma_f(z) \;+\int_{\delta}^{2\delta} dx P_M(x)\int_0^{x} dz\sigma_f(z) \;+\int_{2\delta}^{\infty} dx P_L(x)\int_0^{x} dz\sigma_f(z)\right] \quad . \qquad (4.13)$$

The stress within a fragment integrated over the fragment length x is easily determined in all three cases of fragment lengths. The results for all three fragment lengths are, with reference to Fig. 4.2,

Long ; $$\int_0^x dz\sigma(z) = \delta\alpha\left(\sigma+\sigma_{th}\right)+\left(\sigma\frac{E_f}{E_c}-\alpha\sigma_{th}\right)x \quad . \qquad (4.14)$$

Medium, Short ; $$\int_0^x dz\sigma(z) = \left(\frac{\sigma}{V_f}\right)x-\frac{\alpha}{4\delta}\left(\sigma+\sigma_{th}\right)x^2 \quad . \qquad (4.15)$$

Considering all cases, the integrated stresses contain terms that are either independent of the fragment length, proportional to fragment length x, or proportional to x^2. On substituting the integrated stresses into the appropriate integrals over fragment length x, we obtain the following three contributions to the integrated stress in the fibers

$$\sigma_{fL} = \delta\alpha\left(\sigma+\sigma_{th}\right)\cdot L_0+\left(\sigma\frac{E_f}{E_c}-\alpha\sigma_{th}\right)\cdot L_1 \quad , \qquad (4.16)$$

$$\sigma_{fM} = \left(\frac{\sigma}{V_f}\right)\cdot M_1-\frac{\alpha}{4\delta}\left(\sigma+\sigma_{th}\right)\cdot M_2 \quad , \qquad (4.17)$$

$$\sigma_{fS} = \left(\frac{\sigma}{V_f}\right) \cdot S_1 - \frac{\alpha}{4\delta}(\sigma + \sigma_{th}) \cdot S_2 \tag{4.18}$$

where the coefficients L_i , M_i , S_i are the i^{th} moments of the long, medium, and short fragment distributions, respectively:

$$L_0 = \int_{2\delta}^{\infty} dx\ P_L(x) \quad ; \quad L_1 = \int_{2\delta}^{\infty} dx\, x\, P_L(x) \quad , \tag{4.19}$$

$$M_1 = \int_{\delta}^{2\delta} dx\, x\, P_M(x) \quad ; \quad M_2 = \int_{\delta}^{2\delta} dx\, x^2\, P_M(x) \quad , \tag{4.20}$$

$$S_1 = \int_{0}^{\delta} dx\, x\, P_S(x) \quad ; \quad S_2 = \int_{0}^{\delta} dx\, x^2\, P_S(x) \quad . \tag{4.21}$$

Physically, L_0 is the number of long fragments and L_1 is the length of the long fragments. The composite strain is thus given by

$$\varepsilon_c = \frac{1}{L_T E_f}\left(\sigma_{fL} + \sigma_{fM} + \sigma_{fS}\right) \tag{4.22}$$

where the individual integrated stresses are given above.

Since the initially unloaded composite has thermal stress already, however, we must subtract the initial thermal strain to determine the measured strain. As mentioned in Section 4.1, the residual thermal stress comes from the temperature difference (stress-free temperature and operating temperature). In the above equations, we need to subtract $\sigma_f^T x$ from (or equivalently add $\alpha\sigma_{th}x$ to) the integrated stress over each fragment of length x;

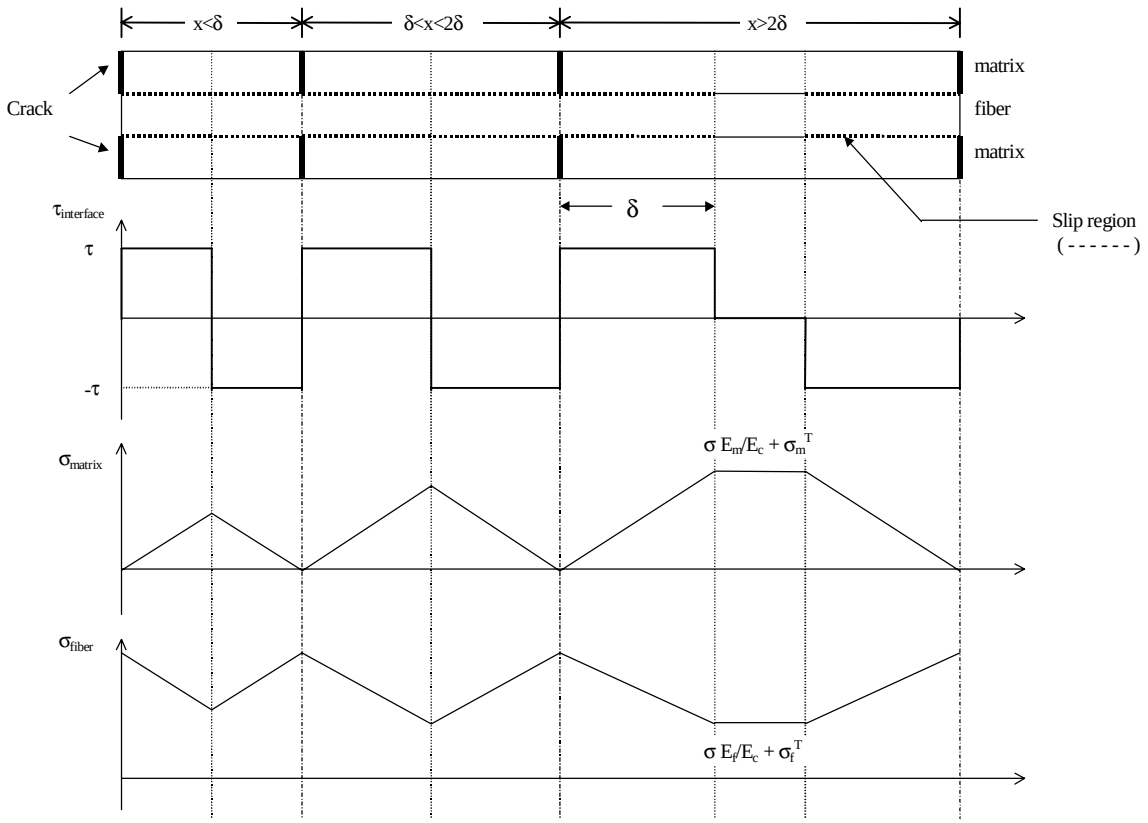

Figure 4.2: Axial stress profiles in the matrix and fibers, and the sliding resistance τ at the interface. Long, medium and short fragments are shown.

this leads to additional terms of $+\sigma_{th}L_1$, $+\sigma_{th}M_1$, and $+\sigma_{th}S_1$ in Eqs. (4.16) - (4.18), and yields the final result

$$\begin{aligned}\sigma_{fL}+\sigma_{fM}+\sigma_{fS} &= \delta\alpha(\sigma+\sigma_{th})\cdot L_0+\left(\sigma\frac{E_f}{E_c}\right)\cdot L_1 \\ &+\left(\frac{\sigma}{V_f}+\alpha\sigma_{th}\right)\cdot M_1-\frac{\alpha}{4\delta}(\sigma+\sigma_{th})\cdot M_2 \\ &+\left(\frac{\sigma}{V_f}+\alpha\sigma_{th}\right)\cdot S_1-\frac{\alpha}{4\delta}(\sigma+\sigma_{th})\cdot S_2 \quad .\end{aligned} \tag{4.23}$$

The strain then follows from Eq. (4.22). Determination of the fragment length distribution and the individual coefficients L_i , M_i , S_i as a function of applied stress σ follows from the single fiber fragmentation theory (see Curtin [78]), and is discussed in the Appendix B.

4.2.3. Unloading and Reloading

Once loaded to a certain level called the "peak stress", $\sigma=\sigma_p$, we can consider the effect of unloading the composite and then reloading back to the original peak load. Note that no additional matrix cracking occurs during the unloading and reloading process and thus the matrix crack spacing is fixed at the distribution $P(x;\sigma_p)$ prevailing at the highest loading stress reached. Unloading the composite can be thought of as superimposing a compressive stress onto the stress prevailing at the fully loaded level. Under unloading, the direction of interface shear stress or slip reverses, first at the matrix crack plane, and then the reverse slip propagates inward away from the matrix crack plane as the applied tensile load is decreased (or equivalently "additional" compressive load is applied). The matrix cracks thus tend to close up toward the uncracked position. Due to the inherent irreversibility of slip, and the associated dissipation of energy during the initial forward slip, the system cannot reverse-slip back to the fully unloaded state. There also exists a residual stress state in the fibers and the matrix, and an associated residual strain even at

complete unloading. The level of the residual strain is also affected by the relieved thermal stresses which are also irreversible. The residual strain is also referred to as the permanent offset and is like a plastic strain in the material.

To determine the strain during unloading requires that the stress distribution in the fibers be determined, just as during the loading process. We neglect any explicit fatigue or wear behavior of the interface during the reverse slip stage such that the slippage is still controlled by the same constant τ, but acting in the opposite direction during unloading. The extent of reverse slip as a function of the unloading stress $\sigma<\sigma_p$ is determined by satisfying the equilibrium relation between the axial stress and the interfacial shear stress τ as given by Eq. (4.7) with the proper boundary condition in order that the fiber stress can be σ/V_f at the matrix crack plane and $\sigma E_f/E_c+\sigma_f^T$ at $\delta(\sigma_p)$. This condition completely determines the reverse slip length, and thus the stress profile in any fragment. The unloading reverse slip length $\delta_{UL}(\sigma)$ is given by (see Fig. 4.3a)

$$\delta_{UL} = \frac{r_f \alpha}{4\tau}\left(\sigma_p - \sigma\right) \quad . \tag{4.24}$$

The evolution of shear stress and axial fiber stress in the long, medium, and short fragments is shown in Figs 4.3 a, b and c for unloading. For long fragments, the slip is only reversed along one half of the original slip length $\delta(\sigma_p)$ after full unloading. For the short fragments, the slip is completely reversed even before full unloading.

The integrated stresses over fragment length, and the subsequent summation of those stresses over the fragment lengths x can be obtained in the same way as for the initial loading in Section 4.2.1. The final result for the integrated stress in the long fiber fragments on unloading to stress σ is

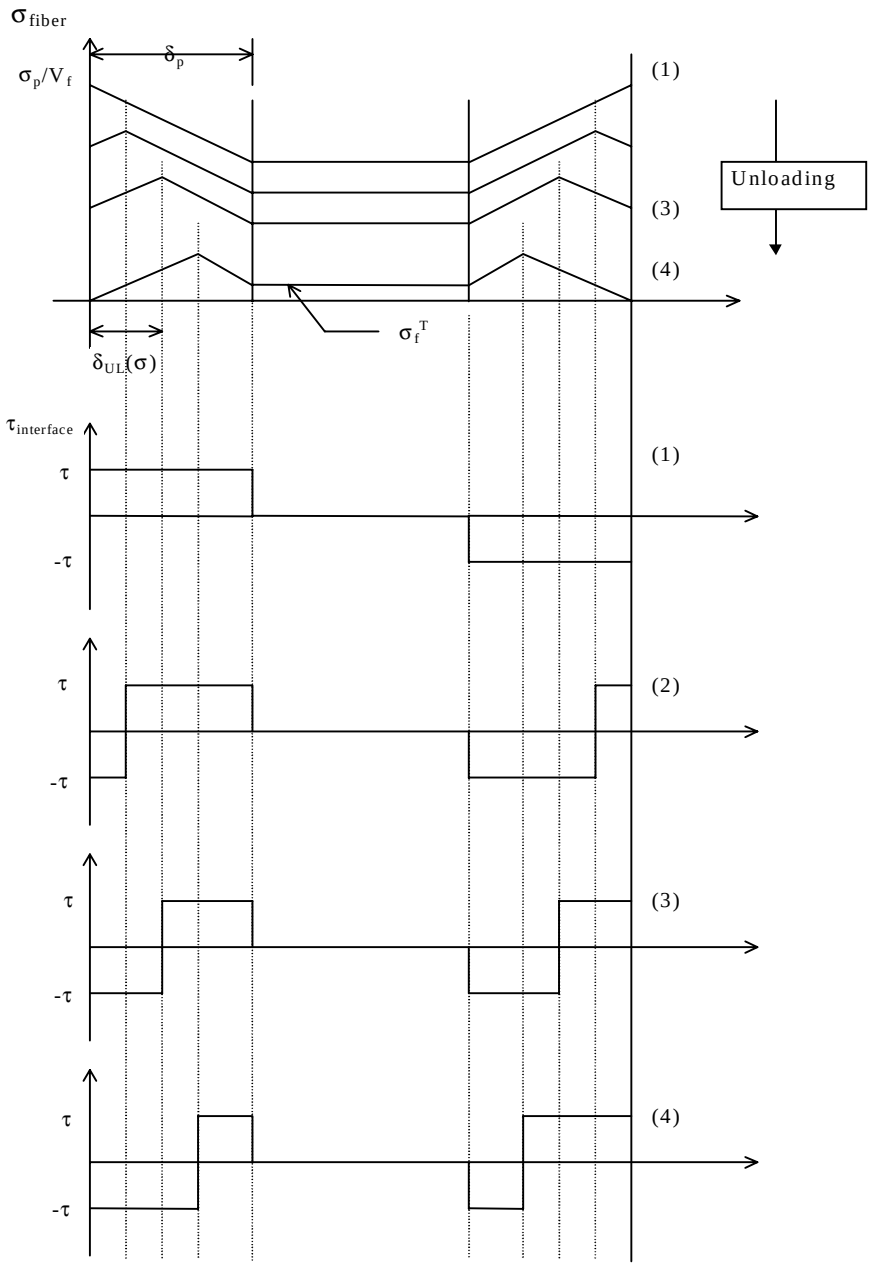

(a)

Figure 4.3: Axial stress profiles in the fibers and the corresponding interface sliding resistance during unloading from a peak stress σ_p; (a) long fragments, (b) medium fragments, (c) short fragments. At a stress σ' in Fig. 4 (c), reverse slip is complete, and the stress profile does not change on further unloading.

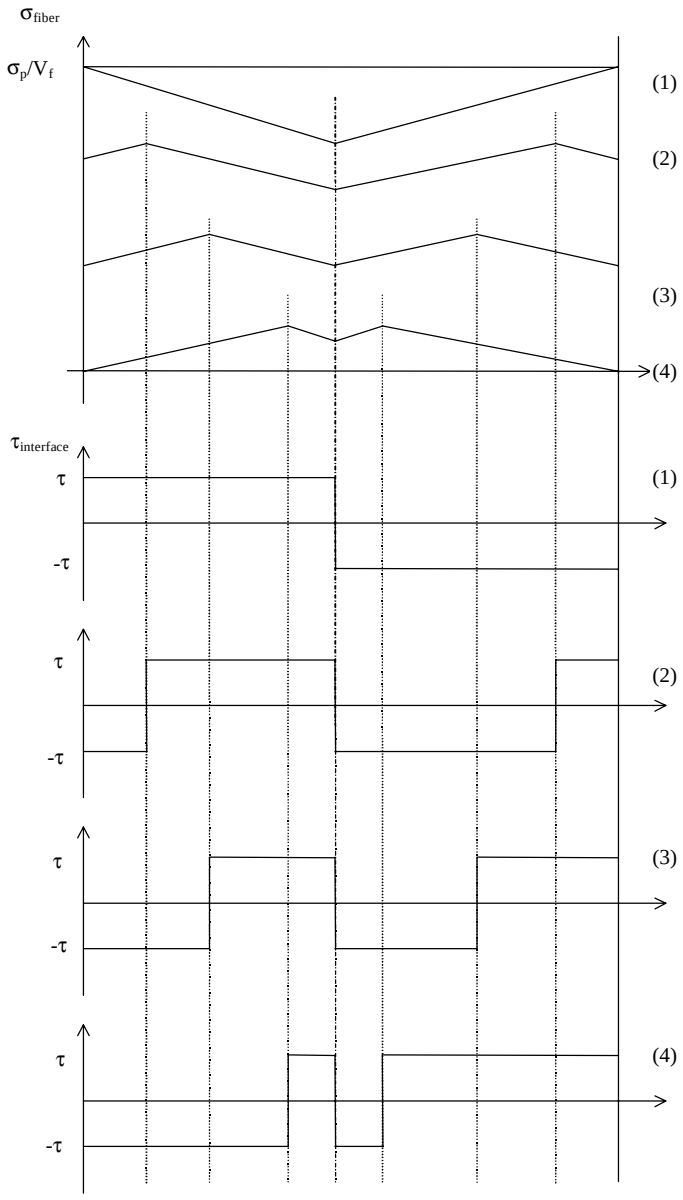

(b)

Figure 4.3 – *Continued.*

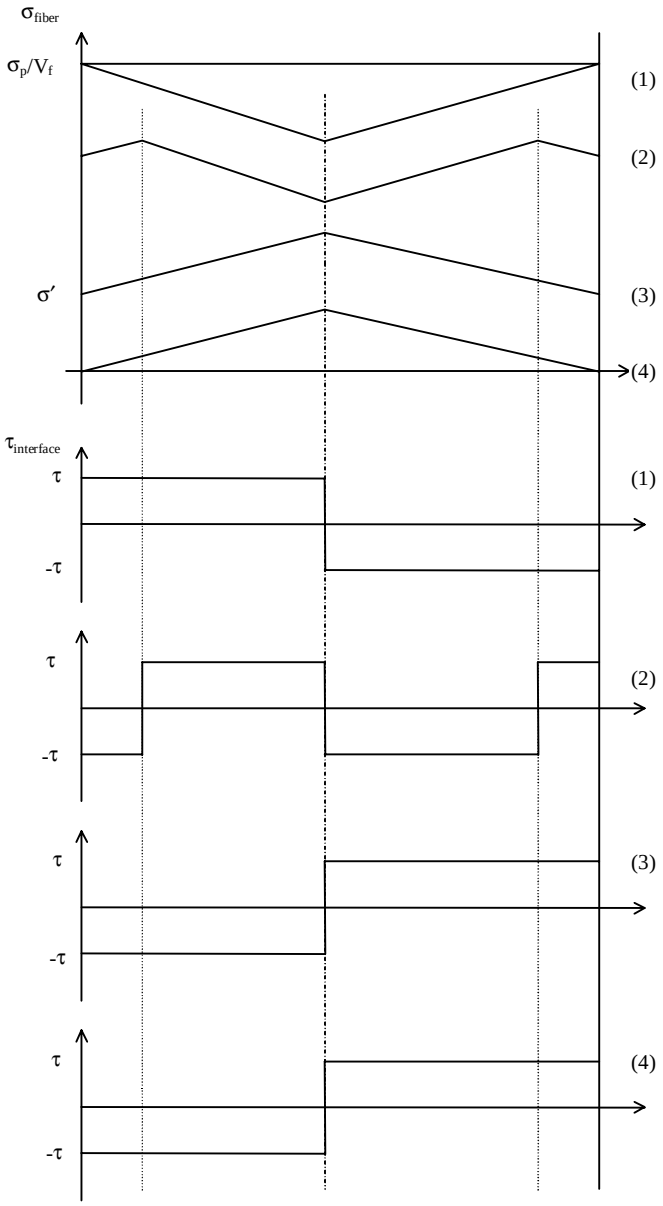

(c)

Figure 4.3 – *Continued.*

$$\sigma_{UL} = \delta_p \alpha \left[\left(\sigma_p + \sigma_{th} \right) - \frac{1}{2} \frac{\left(\sigma_p - \sigma \right)^2}{\left(\sigma_p + \sigma_{th} \right)} \right] \cdot L_0 + \left(\sigma \frac{E_f}{E_c} \right) \cdot L_1 \tag{4.25}$$

and δ_p is the slip length at the peak stress σ_p. For the medium fragments, the shear stress is still never completely reversed, and hence the stress profile does not have a peak at the center at zero applied stress (except for the smallest fragment of $x=\delta_p$). The integrated stress in the medium fragments is then

$$\sigma_{UM} = -\frac{\delta_p \alpha}{2} \cdot \left[\frac{\left(\sigma_p - \sigma \right)^2}{\left(\sigma_p + \sigma_{th} \right)} \right] \cdot M_0 + \left[\sigma \frac{E_f}{E_c} + \alpha \left(\sigma_p + \sigma_{th} \right) \right] \cdot M_1 - \frac{\alpha}{4\delta_p} \left(\sigma_p + \sigma_{th} \right) \cdot M_2 \quad . \tag{4.26}$$

For the shortest fragments, the slip is fully reversed prior to complete unloading. Upon further unloading, the shear stress remains unchanged and the fiber stress profile translates rigidly downward (see Fig. 4.3c). Therefore, we have to divide the evolving stress profile into two sections: that prevailing before full reversal and that after full reversal. We denote the applied stress at which full reversal occurs as $\sigma'(x)$, which depends on the particular fragment size x. At an unload stress σ, the short fragments can be divided into those which have experienced full reversal, $\sigma<\sigma'(x)$, and those which have not, $\sigma>\sigma'(x)$. The dividing line occurs at a fragment length equal to the slip length δ' at stress $\sigma'(x)$,

$$x = \delta' = \delta_p \left(\frac{\sigma_p - \sigma}{\sigma_p + \sigma_{th}} \right) \tag{4.27}$$

and the contributions to the composite strain from these size ranges must be considered separately. The result follows, after some algebra, as

$$\sigma_{US} = \left\{\frac{\sigma}{V_f} + \alpha\sigma_{th}\right\}\int_0^{\delta'} dx\, x\, P_s(x) + \left\{\frac{\alpha}{4\delta_p}\left(\sigma_p + \sigma_{th}\right)\right\}\int_0^{\delta'} dx\, x^2 P_s(x)$$
$$-\left\{\frac{\delta_p\alpha}{2}\frac{\left(\sigma_p - \sigma\right)^2}{\left(\sigma_p + \sigma_{th}\right)}\right\}\int_{\delta'}^{\delta_p} dx\, P_s(x) + \left\{\sigma\frac{E_f}{E_c} + \alpha\left(\sigma_p + \sigma_{th}\right)\right\}\int_{\delta'}^{\delta_p} dx\, x\, P_s(x) \qquad (4.28)$$
$$-\left\{\frac{\alpha}{4\delta_p}\left(\sigma_p + \sigma_{th}\right)\right\}\int_{\delta'}^{\delta_p} dx\, x^2\, P_s(x) \quad .$$

The integrands in the above equation are now partial moments of the short fragment distribution, and the upper and lower bounds of the integrands actually depend on the applied stress. Note also that the 0^{th} moment did not appear in the initial loading case,

$$S_0 = \int_0^{\delta} dx\, P_S(x) \quad . \qquad (4.29)$$

After complete unloading, we can consider reloading back up to the original peak stress σ_p again. During this process, reversed slip (now with the same sign as in the original loading process) again begins at the matrix crack plane and propagates inward and a new slip length for reloading δ_{RL} is formed, which is given by (see Fig. 4.4)

$$\delta_{RL} = \frac{r_f\sigma}{4\tau}\alpha \quad . \qquad (4.30)$$

This length is again obtained by satisfying the equilibrium equation (Eq. (4.7)) and the stress boundary conditions. The stress profiles during reloading for the long, medium, and short fragments are shown together in Fig. 4.4. For short fragments, the reversed slip again propagates across the entire fragment before reloading is complete, and once the slip extends across the fragment it does not change and the fiber stress profile translates rigidly upward with further increased load. The stress at which this shift in behavior occurs is denoted by $\sigma''(x)$, and it again depends on fragment length, but is straightforward to identify.

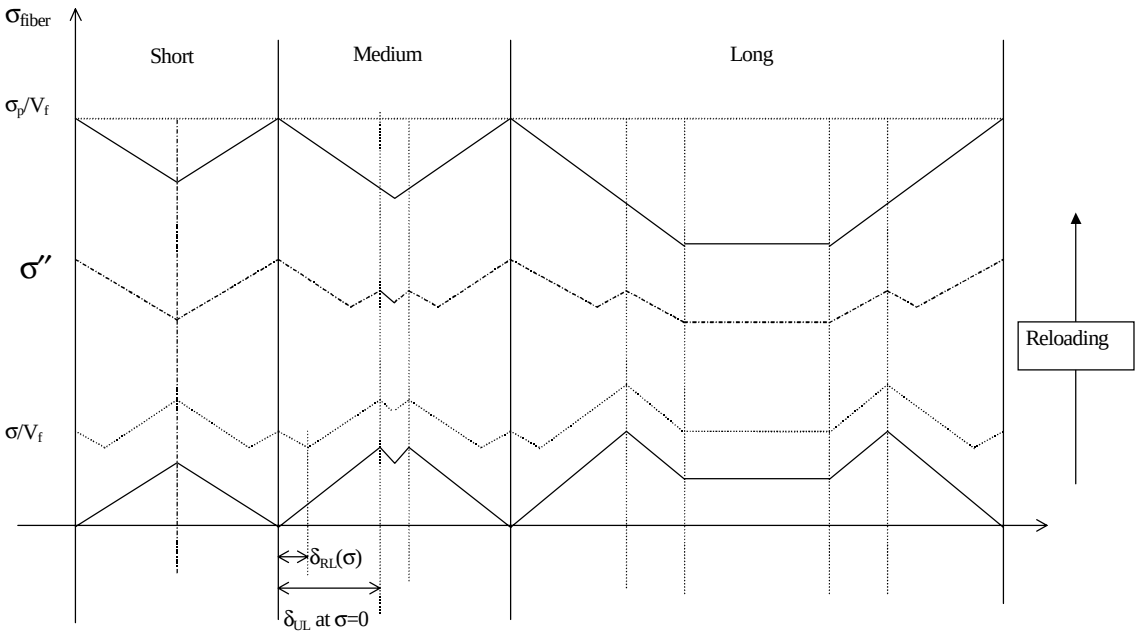

Figure 4.4: Axial stress profiles in the long, medium and short fiber fragments on reloading. For short fragments at a stress σ'', the slip is complete and the stress profile does not change on further reloading.

Integrating the stresses over fragment length then yields the contributions of each class of fragments to the reloading stress, and hence strain. For the long fiber fragments, the integrated stress in the fibers is

$$\sigma_{RL} = \delta_p \alpha \left[\left(\sigma_p + \sigma_{th} \right) - \frac{1}{2} \frac{\left({\sigma_p}^2 - \sigma^2 \right)}{\left(\sigma_p + \sigma_{th} \right)} \right] \cdot L_0 + \left(\sigma \frac{E_f}{E_c} \right) \cdot L_1 \quad . \tag{4.31}$$

For medium fragments,

$$\begin{aligned} \sigma_{RM} = & -\frac{\delta_p \alpha}{2} \left[\frac{\left({\sigma_p}^2 - \sigma^2 \right)}{\left(\sigma_p + \sigma_{th} \right)} \right] \cdot M_0 + \left[\sigma \frac{E_f}{E_c} + \alpha \left(\sigma_p + \sigma_{th} \right) \right] \cdot M_1 \\ & - \frac{\alpha}{4\delta_p} \left(\sigma_p + \sigma_{th} \right) \cdot M_2 \quad . \end{aligned} \tag{4.32}$$

And finally, for short fragments,

$$\begin{aligned} \sigma_{RS} = & \left\{ \frac{\sigma}{V_f} + \alpha \sigma_{th} \right\} \int_0^{\delta''} dx \, x \, P_s(x) - \left\{ \frac{\alpha}{4\delta_p} \left(\sigma_p + \sigma_{th} \right) \right\} \int_0^{\delta''} dx \, x^2 P_s(x) \\ & + \left\{ \frac{\delta_p \alpha}{2} \frac{\sigma^2}{(\sigma_p + \sigma_{th})} \right\} \int_{\delta''}^{\delta_p} dx \, P_s(x) + \left\{ \sigma \frac{E_f}{E_c} + \alpha \sigma_{th} \right\} \int_{\delta''}^{\delta_p} dx \, x \, P_s(x) \\ & + \left\{ \frac{\alpha}{4\delta_p} \left(\sigma_p + \sigma_{th} \right) \right\} \int_{\delta''}^{\delta_p} dx \, x^2 P_s(x) \quad . \end{aligned} \tag{4.33}$$

where the dividing line between fully reversed slip and partial slip is now at the length

$$\delta'' = \delta_p \frac{\sigma}{(\sigma_p + \sigma_{th})} \quad . \tag{4.34}$$

So far, we have obtained expressions for the average stress carried by the fibers under both unloading and reloading, including the long, medium and short fragments, in terms of initial peak stress σ_p, the applied stress σ, the slip length δ_p at σ_p and the moments of

the various parts of the fragment distributions. The unload/reload hysteresis loops are obtained from the equations for unloading and reloading in this section by $\sigma_{UL}+\sigma_{UM}+\sigma_{US}$ versus σ and $\sigma_{RL}+\sigma_{RM}+\sigma_{RS}$ versus σ, respectively. Note that the coefficients L_i, M_i, S_i, or equivalently the distributions $P_L(x)$, $P_M(x)$, $P_S(x)$ are unchanged during the unload/reload cycle. Thus, all of the stress dependence in the hysteresis loops is explicitly shown in Eqs. (4.25), (4.26), (4.28), (4.31)-(4.33). The above formulation is entirely general within the context of the shear lag model, with the only input being the matrix crack spacing distribution $P(x)$.

Before presenting our results, we first briefly review the analysis used by Pryce and Smith [80], and others [81,92], in which the matrix cracks are assumed to be spaced equally throughout the evolution of cracks. The PS results are a special case of our more general formulation described above. If the matrix cracks are all spaced equally, then they all fall into one category, e.g. all long fragments or all medium fragments, and all moments of the distribution are products of the mean fragment length. Note that PS did not attempt to specify the fragments shorter than δ. There are two cases to consider. First, if the average crack spacing $\bar{x}$ is larger than twice the current slip length, $\bar{x}>2\delta(\sigma)$, then the fragments are "long" fragments. The strain in the composite is then given precisely by Eq. (4.16) divided by $L_T E_f$, with the coefficients L_0 and L_1 simply given by

$$L_0 = L_T / \bar{x} \quad ; \qquad L_1 = L_T \quad . \tag{4.35}$$

Substituting these into Eq. (4.16) and rearranging leads to the simple final result

$$\varepsilon_c = \frac{\alpha}{E_f}\frac{\delta(\sigma)}{\bar{x}}\left(\sigma+\sigma_{th}\right)+\frac{\sigma}{E_c} \quad , \qquad \bar{x}>2\delta \tag{4.36}$$

which has been put in a normalized form but is otherwise identical to the form presented by PS.

Beyond a certain stress level, the condition $\bar{x}>2\delta$ ceases to hold and PS assumed all the fragments are in the range of $\bar{x}<2\delta$. If one continues to simply use the average crack spacing, then when $\bar{x}<2\delta$ the fragments are all in the "medium" size category. The composite strain is then given by Eq. (4.17) divided by $L_T E_f$ with the coefficients M_i given by

$$M_0 = L_T / \bar{x} \quad ; \qquad M_1 = L_T \quad ; \qquad M_2 = \bar{x} L_T \quad . \tag{4.37}$$

Substituting these back into Eq. (4.17) yields the composite strain at the higher stress levels of

$$\varepsilon_c = \frac{1}{E_f}\left[\left(\frac{\sigma}{V_f}+\alpha\sigma_{th}\right)-\frac{\bar{x}}{4\delta(\sigma)}\alpha\left(\sigma+\sigma_{th}\right)\right] \quad , \qquad \bar{x}<2\delta \quad . \tag{4.38}$$

Note that there is a conceptual inconsistency here: once the fragments become "medium" in length, there is no region of matrix which can attain the applied stress and thus cracking should saturate. However, since the spacing is actually stochastic and there are still longer fragments which can fragment further, cracking really does continue and the mean spacing continues to decrease. In deriving Eq. (4.38) above, one simply neglects this inconsistency and considers the average crack spacing versus applied stress to be supplied without consideration as to the physical process by which it reached any particular value.

The strains during the unload/reload process are determined in a similar way. Using the special cases of the distribution moments L_i and M_i shown in Eqs. (4.35) and (4.37), we are able to derive the strain equations for "all long" and "all medium" fragments. PS did not consider the "all medium" fragments case on unloading and reloading, but only showed the equations for composite strain when $\bar{x}>2\delta$. Here, we extend the PS theory to take into account the all medium fragments case ($\bar{x}<2\delta$). The strain on unloading is obtainable from Eqs. (4.25) and (4.26) with the distribution moments in Eqs. (4.35) and (4.37),

$$\varepsilon_U = \frac{\sigma}{E_c} + \frac{\alpha}{E_f}\frac{\delta_p}{\bar{x}}\left[\left(\sigma_p + \sigma_{th}\right) - \frac{1}{2}\frac{(\sigma_p - \sigma)^2}{\left(\sigma_p + \sigma_{th}\right)}\right] \quad , \quad \bar{x} > 2\delta \ , \qquad (4.39)$$

$$\varepsilon_U = \frac{\sigma}{E_c} + \frac{\alpha}{E_f}\left[\left(1 - \frac{\bar{x}}{4\delta_p}\right)\left(\sigma_p + \sigma_{th}\right) - \frac{\delta_p}{2\bar{x}}\frac{(\sigma_p - \sigma)^2}{\left(\sigma_p + \sigma_{th}\right)}\right] \quad , \quad \bar{x} < 2\delta \ . \qquad (4.40)$$

Substituting the moments into Eqs. (4.31) and (4.32) gives the composite strain on reloading as

$$\varepsilon_R = \frac{\sigma}{E_c} + \frac{\alpha}{E_f}\frac{\delta_p}{\bar{x}}\left[\left(\sigma_p + \sigma_{th}\right) - \frac{1}{2}\frac{(\sigma_p{}^2 - \sigma^2)}{\left(\sigma_p + \sigma_{th}\right)}\right] \quad , \quad \bar{x} > 2\delta \ , \qquad (4.41)$$

$$\varepsilon_R = \frac{\sigma}{E_c} + \frac{\alpha}{E_f}\left[\left(1 - \frac{\bar{x}}{4\delta_p}\right)\left(\sigma_p + \sigma_{th}\right) - \frac{\delta_p}{2\bar{x}}\frac{(\sigma_p{}^2 - \sigma^2)}{\left(\sigma_p + \sigma_{th}\right)}\right] \quad , \quad \bar{x} < 2\delta \ . \qquad (4.42)$$

The key stress-dependent parameter $\bar{x}$ is obtained below as a function of (statistical) matrix crack parameters and is not obtained from experiment at each load level.

4.2.4. Statistical Matrix Crack Evolution

The analysis performed by Marshall, Cox and Evans [39] determines the matrix cracking stress versus flaw size in a unidirectional fiber composite. Curtin [77,78] has previously shown that such a relationship then leads, for an underlying two-parameter Weibull distribution of flaw sizes, to a three-parameter Weibull distribution for the matrix cracking "strength". Specifically, the number of matrix flaws in a volume V that can propagate at an applied composite stress σ or less, which we denote $\Phi(\sigma,V)$, can be represented as

$$\Phi(\sigma, V) = \frac{V}{V_0}\left(\frac{\sigma - (\sigma^* - \sigma_{th})}{\sigma_0}\right)^{\rho} \tag{4.43}$$

where ρ is the Weibull modulus, and σ_0 is the characteristic strength for one crack in a volume V_0 of material. Matrix cracking occurs over a range of stress starting at σ^*-σ_{th} and with an evolving range of crack spacings. However, there is a characteristic strength level around which most of the matrix cracking occurs and an associated characteristic length scale that is comparable to the matrix crack spacing at the end of the cracking (saturation). To identify the relevant length scale δ_R, we recognize that δ_R must be the slip length associated with some characteristic applied stress σ_R^{th} (Eq. (4.8) with $\sigma=\sigma_R^{th}$), and σ_R^{th} itself is the typical matrix cracking strength at the characteristic gauge length $2\delta_R$, when the thermal stress is included. To avoid confusion, the typical reference stress in the case of no thermal stress is denoted by σ_R. Dividing the volume V into an area A and length L, the characteristic scales δ_R and σ_R^{th} therefore satisfy the relationship

$$\Phi\left(\sigma_R^{th}, L = 2\delta_R\right) = 1 \quad . \tag{4.44}$$

From Eqs. (4.43) and (4.44), the reference stress with thermal stress considered, σ_R^{th}, turns out to be simply σ_R-σ_{th}. With no loss of generality, we can then represent the strength distribution of the matrix by the form

$$\Phi(\sigma, L, A) = \frac{LA}{2\delta_R A_0}\left\{\frac{\sigma - (\sigma^* - \sigma_{th})}{(\sigma_R - \sigma_{th}) - (\sigma^* - \sigma_{th})}\right\}^{\rho} \quad . \tag{4.45}$$

Most of the cracking occurs around an applied stress $\sigma=\sigma_R$-σ_{th}, all stresses are to be measured in terms of σ_R-σ_{th}, and all lengths are measured in terms of δ_R. The strength distribution in this form controls the complete evolution of matrix cracking, as we have discussed previously. Note that Φ is the flaw strength distribution; not every flaw can grow into a matrix crack. The slip zone formation around existing microcracks inhibits some flaws from propagating. This is a key aspect of the cracking evolution, and is

discussed below and in Section 4.4. All of the relevant parameters describing the matrix cracking process are contained in Eq. (4.45): the reference stress σ_R, the onset stress σ^*, the Weibull modulus ρ, and the thermal stress in the composite σ_{th}. It is these four parameters which are the "fitting" parameters for comparing theory to experiment.

The detailed calculation of the normalized crack spacing distribution $P(x/\delta_R)$ as a function of the normalized applied composite stress, $\sigma/(\sigma_R-\sigma_{th})$, in terms of the remaining normalized parameters ρ, $\sigma^*/(\sigma_R-\sigma_{th})$ and $\sigma_{th}/(\sigma_R-\sigma_{th})$, is discussed in detail in Section 4.4. Suffice it to say that the full details of the evolving matrix cracking can be calculated and are a function only of four parameters. Various case studies are shown in the next Section.

Finally, Pryce and Smith, and others, do not present a methodology for determining the crack spacing evolution as a function of the underlying statistical parameters of the matrix cracking strength, but rather utilize the measured average crack spacing as a function of applied composite stress as input into the calculation of the composite strain. The present analysis determines the matrix crack spacing distribution versus applied stress as a function of the four parameters σ_R, ρ, σ^* and σ_{th}, and insists that both the matrix crack spacing distribution and the resulting stress/strain and hysteretic behavior be captured simultaneously.

4.3. Application of the Theory

In this Section, we first discuss the stress/strain curves obtained for various matrix cracking parameters, and then study the hysteresis loops at various stages of the cracking. The constituent properties E_m, E_f, V_m, V_f are needed in all calculations, and for our parameter study we adopt values relevant to the well-studied system of Nicalon fibers in a CAS glass matrix (Table 4.I). We consider the thermal stress as a variable to accommodate variations in the test temperature.

We first investigate matrix cracking in the absence of any thermal stress (σ_{th}=0) and with a normalized onset stress $(\sigma^*-\sigma_{th})/(\sigma_R-\sigma_{th}) = \sigma^*/\sigma_R = 0.5$. The dimensionless stress/strain curves from the present theory for various Weibull moduli ρ=3, 5, and 10 are shown in Fig. 4.5a; the dimensionless composite strain is $\varepsilon E_f/(\sigma_R-\sigma_{th})$. At the beginning of the tensile test, $\sigma<\sigma^*-\sigma_{th}$, no matrix cracking occurs and the slope of the stress/strain curve is the composite modulus E_c. Note that the slope in the figure is E_c/E_f since the transverse axis is the normalized strain, $\varepsilon E_f/(\sigma_R-\sigma_{th})$. After matrix crack saturation, the matrix carries a fixed small load and all additional load is carried by the fibers so that the modulus is simply that of the fiber bundle alone, $V_f E_f$. Variations in the Weibull modulus govern the matrix cracking and deformation between these two limits. For high Weibull modulus, the cracking occurs over a narrow range of stresses around $\sigma_R-\sigma_{th}$ and the stress/strain curve is quite linear to stresses somewhat above $\sigma^*-\sigma_{th}$. Thus, the "proportional" limit appears to be rather higher than the minimum ACK estimate at which the first crack can appear. In fact, the stress at which the very first crack does appear is a function of the actual length of the sample and the Weibull modulus. For low Weibull moduli, some deformation is evident just above the onset stress $\sigma^*-\sigma_{th}$ and the range of matrix cracking is much broader around the characteristic stress $\sigma_R-\sigma_{th}$. In the extreme case of $\rho=\infty$, the stress/strain curve becomes flat at $\sigma_R-\sigma_{th}$; this is the case of a "unique strength" which means the matrix cracking occurs at one specific stress abruptly, and no "evolution" is observed. This case is essentially never observed, which has motivated the present statistical approach for the analysis of matrix cracking.

Stress/strain curves without thermal stress $(\sigma_{th}=0)$ are also shown in Fig. 4.5b for a higher onset stress σ^*/σ_R=0.75 and various Weibull moduli. As $\sigma^*-\sigma_{th}$ approaches $\sigma_R-\sigma_{th}$,

Table 4.I Some material properties of Nicalon/CAS composites.

Material Properties	***Values***
E_f (Fiber modulus)	190 MPa
E_m (Matrix modulus)	90 MPa
V_f (Fiber volume fraction)	0.34
V_m (Matrix volume fraction)	0.66
α_f (Fiber thermal expansion coefficient)	3.3×10^{-6} K^{-1}
α_m (Matrix thermal expansion coefficient)	4.6×10^{-6} K^{-1}

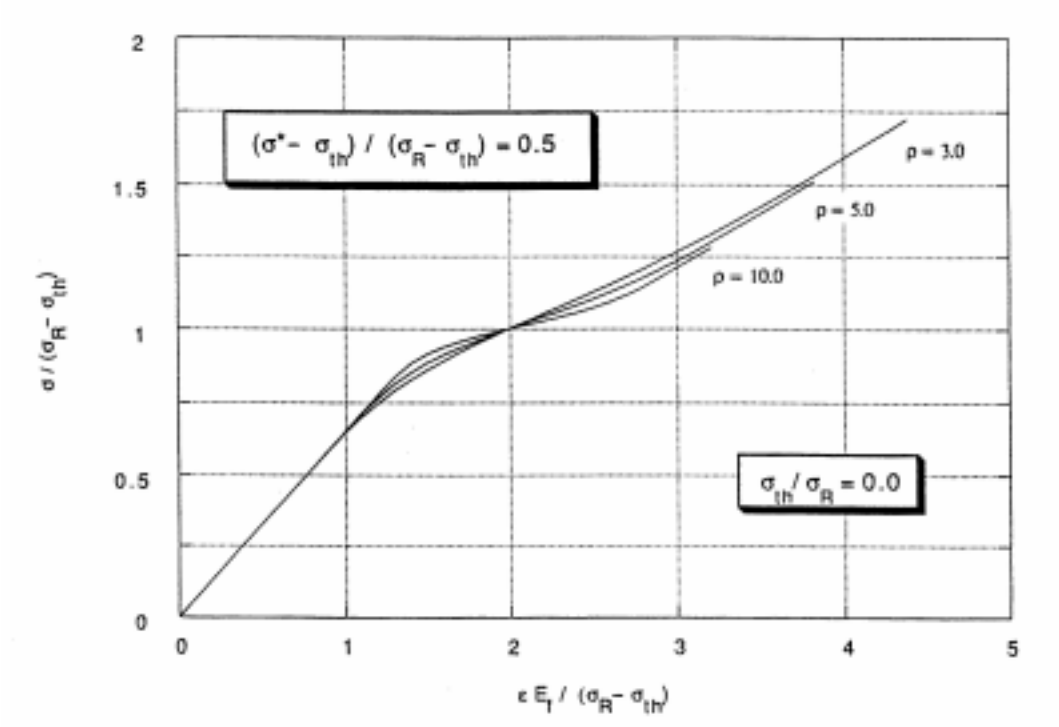

(a)

Figure 4.5: Dimensionless stress/strain curves for various Weibull moduli. The dimensionless applied stress is $\sigma/(\sigma_R-\sigma_{th})$, and the dimensionless composite strain is $\varepsilon E_f/(\sigma_R-\sigma_{th})$. (a) $\sigma^*/\sigma_R=0.5$. (b) $\sigma^*/\sigma_R=0.75$. Thermal stress is zero in both cases. Material properties are given in Table 4.I.

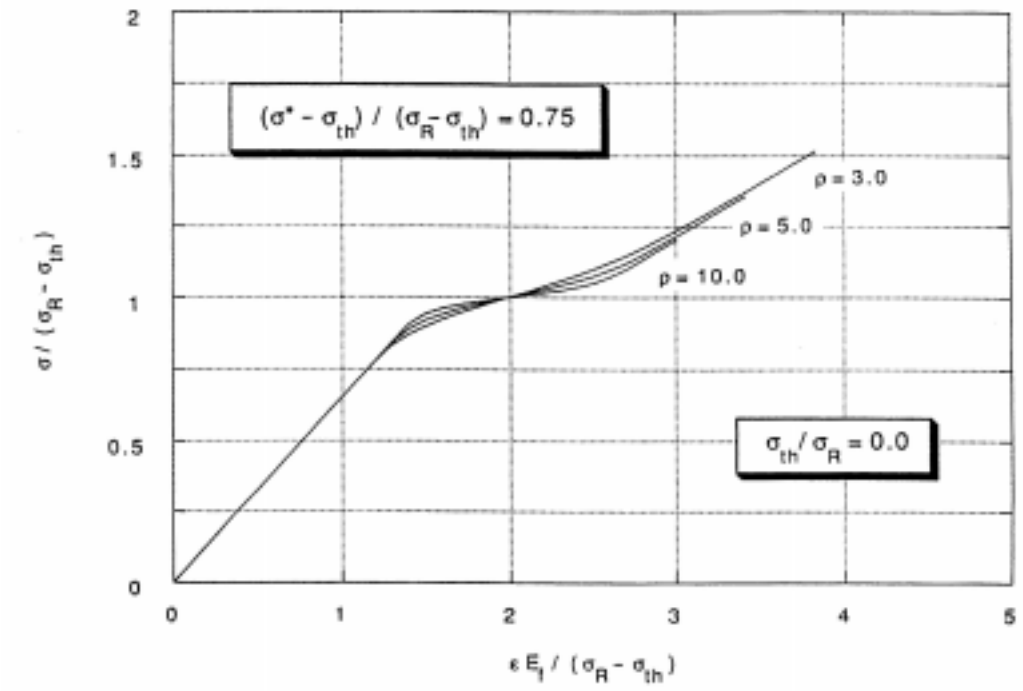

(b)

Figure 4.5 – *Continued.*

the cracking is increasingly confined to the stress range between σ^*-σ_{th} and just above σ_R-σ_{th}, and the deformation becomes less sensitive to the actual Weibull modulus. The limits of (i) $\sigma^*=\sigma_R$ for any ρ and (ii) $\rho=\infty$ for any σ^* yield identical results because in both cases the cracking starts and finishes at σ_R.

In the presence of residual stress, the stress/strain behavior is modified because residual strain is gradually relieved as the matrix cracking progresses. Figure 4.6 shows the stress/strain behavior for fixed σ^*/σ_R=0.5 and ρ=3 for various values of thermal stress σ_{th}. Note that the normalizing stress is σ_R-σ_{th}, which explicitly involves the thermal stress. In this example, we have fixed the underlying quantity σ^*/σ_R which is related to the intrinsic flaws in the matrix independent of the thermal stress. Thus, the onset stress σ^*-σ_{th} varies between the various cases, even when normalized by σ_R-σ_{th}. The cracking initiates at σ^*-σ_{th} and occurs predominantly around σ_R-σ_{th}, and the strain increases more rapidly with increasing thermal stress in the composite (thermal compression in the fibers if $\alpha_f<\alpha_m$), as expected. At saturation, the maximum possible strain in the composite is the strain in the fiber bundle σ/V_fE_f plus the released fiber thermal strain σ_f^T/E_f, and beyond saturation the composite again responds linearly with elastic modulus V_fE_f.

Examples of the unload/reload behavior at various applied stresses are shown in Fig. 4.7 for some typical parameters (σ^*/σ_R = 0.5) and two thermal stresses. As expected, the hysteresis loops widen as the matrix cracking proceeds because there are more cracks, more sliding, and hence more irreversible energy dissipation. The permanent offset strain (strain at zero load) also increases monotonically with increasing load level. Although not clearly evident from the hysteresis loops, the loops cannot strictly be described by simple quadratic power laws. In addition, the thermal stress has a distinct influence on the shape of the hysteresis loop. In particular, the difference between offset strains at zero stress is generally larger than the difference between strains at the maximum load level by an appreciable amount, demonstrating that the thermal stress skews the hysteresis loop

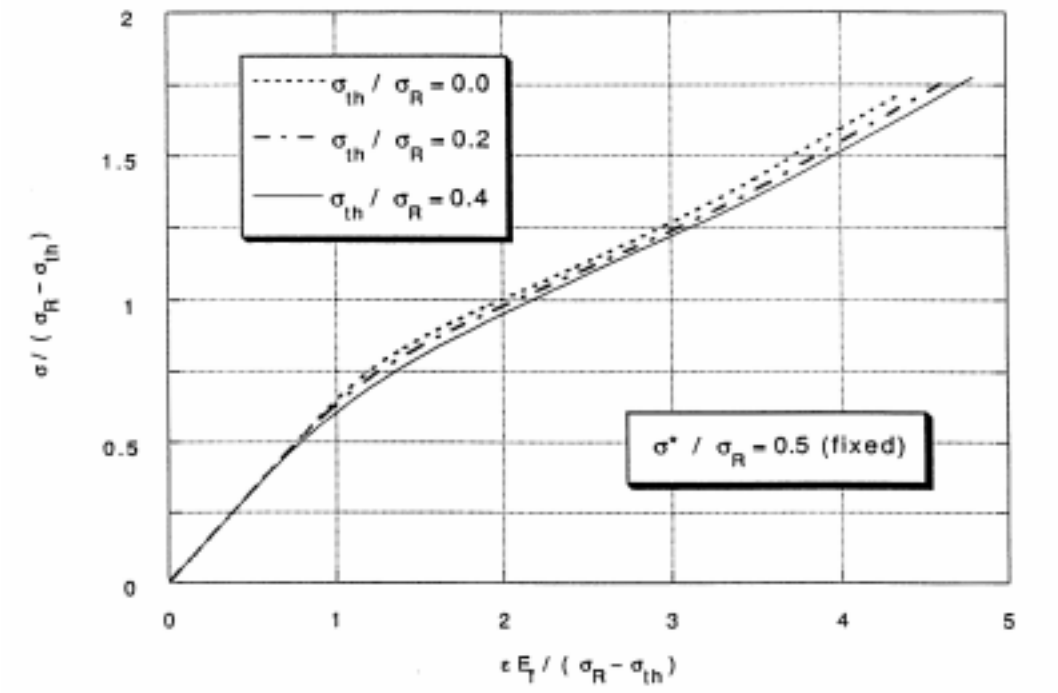

Figure 4.6: Stress/strain curves for various values of dimensionless thermal stress σ_{th}/σ_R. σ^*/σ_R is fixed at 0.5 for all cases, and ρ=3.0. Material properties are given in Table 4.I.

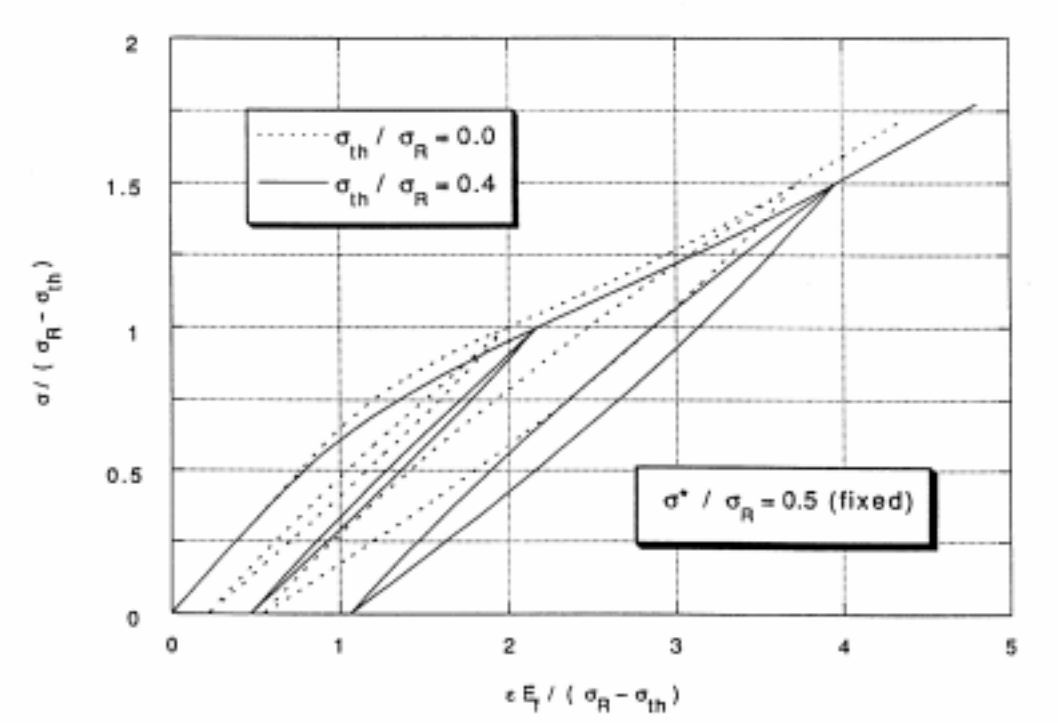

Figure 4.7: Hysteresis loops from unload/reload behavior with/without thermal stresses. σ^*/σ_R=0.5. Material properties are given in Table 4.I.

and, for the case of compressive fiber stresses, narrows the loop relative to the case in the absence of thermal stress.

Using the evolution of matrix cracking as calculated from the full statistical problem, we can determine the mean crack spacing $\bar{x}$ versus applied load and use this as "experimental input" into the simple theory of Pryce and Smith. A comparison of the full statistical prediction and the approximate PS prediction from Eqs. (4.23) and (4.38) is shown in Fig. 4.8a for a typical set of parameters. The PS theory consistently predicts slightly larger strains, with the extent of the deviation increasing with increasing stresses. The origin of the discrepancy is that the PS theory treats all the cracks as "optimally" spaced, which maximizes the amount of slipping in the composite and generates larger deformations. However, since in the true stochastic case many of the cracks are in fact "long" cracks which the PS approach accounts for properly, the overall deviation is not large. In addition, our extension of the PS results to higher stresses, where the mean crack spacing is $\bar{x}<2\delta$ and falls in the "medium" length category, captures the deformation at higher loads fairly well. Thus, an appropriately modified PS theory can predict the deformation fairly well through the entire loading history *as long as the mean crack spacing is supplied by some means.*

To evaluate the precise discrepancy between the PS results and the "exact" deformation calculated here, we proceed as follows. The deformation behavior depends on the fragment lengths relative to the current slip length δ, which in turn depends on the interfacial slip resistance τ. The true value of τ generates the "exact" deformation while the PS prediction shown in Fig. 4.8a is not quite accurate. To make the PS prediction match the "exact" result as closely as possible, the value of τ or δ used in the PS prediction can be adjusted to fit the "exact" results. In other words, if the "exact" results are considered as experimental data and are generated by an underlying value of τ, then using the PS approach to fit this data would lead one to deduce a value of τ_{PS} that is different from the actual τ. The difference in τ is proportional to the difference in the

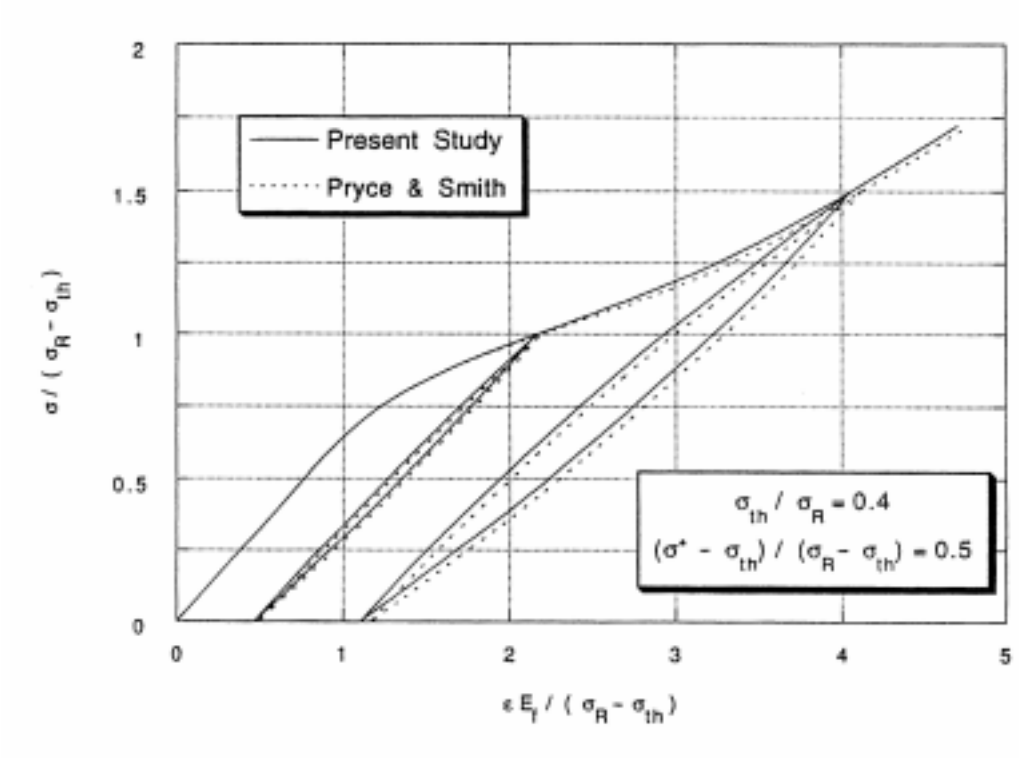

(a)

Figure 4.8: (a) Comparison of hysteresis loops from the present theory (solid line) and those from the Pryce and Smith prediction (dashed line) using the crack evolution from the present theory for parameters σ_{th}/σ_R=0.4, $(\sigma^*-\sigma_{th})/(\sigma_R-\sigma_{th})$=0.5, and ρ=3.0. (b) as in (a) but with adjusting τ in the Pryce and Smith approach to best-fit the present theory. (c) as in (b) but without thermal stress. Material properties are given in Table 4.I.

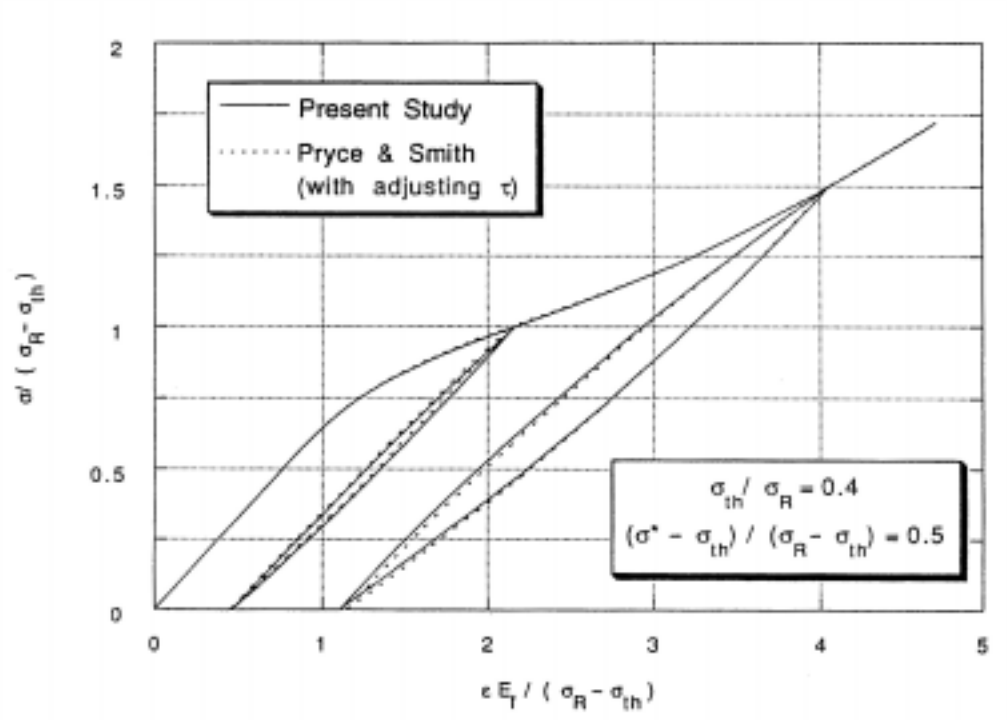

(b)

Figure 4.8 – *Continued.*

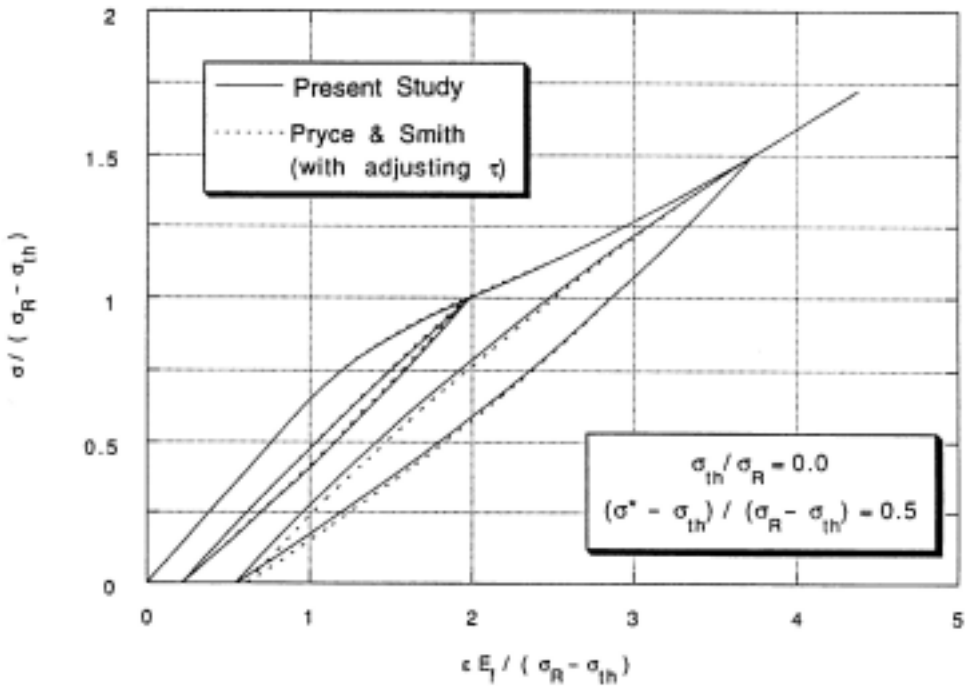

(c)

Figure 4.8 – *Continued.*

reference length δ_R, and so we fit the PS theory to the exact data by adjusting the apparent reference length $\delta_{R(PS)}$ to best fit the exact data. We calculate the difference in strain at the same stress between the exact data and the PS prediction for various $\delta_{R(PS)}$ and select the value of $\delta_{R(PS)}$ that minimizes, in a least-squares sense, the difference over the entire stress/strain curve, including loading and unloading. The discrepancy is then characterized by the ratio of the apparent τ_{PS} from the PS fit to the actual τ in the material, τ_{PS}/τ.

Figures 4.8 b and c show the stress/strain behavior and hysteresis loops that are fit to the "exact" data by adjusting τ for two particular sets of parameters, one with and one without thermal stress. The resulting ratio in both cases is 1.1; that is the derived τ_{PS} value is 10% larger than the actual τ value. The fit is not perfect but is extremely good for the stress/strain behavior and for the upper portions of the hysteresis loops. The hysteresis loop widths are quite comparable, and only the permanent offset strain can not be obtained very accurately. A factor of roughly 10% difference in the τ values is obtained for a wide range of parameters sets, allowing us to conclude that in general the procedure advocated by Pryce and Smith is accurate to within 10% for the value of τ *if the evolving mean crack spacing is given*. This is generally well within the range of other uncertainties in the experimental procedures, variations in real material data, and the limitations of the shear lag model.

4.4. Obtaining τ from Experimental Data

In the previous Section, we performed a parametric study of the predicted deformation behavior with the given underlying parameters σ_R, σ^*, σ_{th}, ρ, and also compared the results to a modified version of the PS approach. Here, we discuss the procedure by which experimental data is analyzed within the context of the present theory. We wish to avoid any need for visual detection of the matrix cracks, except after failure, and to make the most use out of the easily-obtained stress/strain and hysteresis

data. There are only the four parameters, as noted above, that should govern the stress/strain and hysteresis loop behavior. Thus, experimental data can be "fitted" by appropriately adjusting the four parameters, but the manner in which this should be attempted merits some discussion.

First of all, the four parameters used to describe the data should be the thermal-stress corrected stresses σ_R-σ_{th} and σ^*-σ_{th} along with ρ and σ_{th}. Most of the cracking and deformation occurs around σ_R-σ_{th} and no cracking occurs prior to σ^*-σ_{th}. σ_R-σ_{th} is clearly the most pertinent stress to identify, primarily because there is often no noticeable deviation from linearity at the onset stress and hence the overall deformation is usually not too sensitive to the value of σ^*-σ_{th}. An initial guess of σ^*-σ_{th} = 0 can be taken. The rough identification of σ_R-σ_{th} can thus be made as the midpoint between a proportional limit (noticeable deviation from linearity) and a saturation limit (where the tangent modulus becomes constant and approximately $V_f E_f$). The thermal stress can be roughly estimated from the standard Eqs. (4.3), (4.4) and (4.6) but uncertainties in the constituent parameters and the temperature T_0 suggest that σ_{th} should be considered to lie in some range around the estimated value.

With initial guesses for σ_R-σ_{th} and σ_{th}, the experimental stress can then be normalized by σ_R-σ_{th} and the strain by $(\sigma_R$-$\sigma_{th})/E_f$. Calculations of the predicted deformation in the normalized units are then performed for the same values of σ^*-σ_{th} and σ_{th}, and the remaining parameter ρ is varied to obtain the best overall fit to the experimental deformation. Comparison of the best fit prediction with the experimental data will then clearly show directions for further refinement of the normalizing parameter σ_R-σ_{th} and σ_{th} itself. If the overall fit is too low or too high in stress, then the value of σ_R-σ_{th} needs to be corrected in the opposite direction. If the predicted strain agrees well at low stresses but not at high stresses, then the thermal stress should be made more compressive or tensile to push the strain up or down, respectively, at higher stresses. The skewness of the hysteresis loops is also affected by the magnitude of the thermal strain, as demonstrated in Fig. 4.7. If the selected σ_R-σ_{th} and σ_{th} are nearly correct then the best-fit

Weibull modulus should predict an accurate slope of the deformation through the middle portion of the deformation, as indicated in Fig. 4.5b. The correct assessment of the actual values of σ^*-σ_{th} and ρ can be more subtle because, as noted earlier, the effects of larger σ^*-σ_{th} and larger ρ are roughly the same. Thus, it is possible that the deformation behavior is well-predicted by a variety of choices for σ^*-σ_{th} and ρ; in such a case, however, most of the quantities of physical interest, such as τ, will not be sensitive to the precise values of σ^*-σ_{th} and ρ.

After having fit the experimental data to the desired level of accuracy, one now has estimates of the parameters σ_R-σ_{th}, σ^*-σ_{th}, σ_{th}, and ρ. This information alone is not sufficient, however, to determine the interfacial τ. The reference length δ_R is also needed, which is the slip length at a stress σ_R-σ_{th}, and then Eq. (4.8) can be used to obtain τ. But, δ_R has not been explicitly determined and is not important for the macroscopic deformation of the system. Only the product of $\delta_R\tau$ determines the macroscopic deformation; one can obtain the same deformation with a low value of τ and large crack spacings (large δ_R) or with a high value of τ and small crack spacings (small δ_R). To determine which case holds, and hence to find τ, requires the measurement of an actual physical length associated with the matrix cracking at some stage of the test.

The most convenient choice for a length measurement is the average matrix crack spacing at the end of the test, which can be obtained in a separate visual measurement after the mechanical testing is completed! The average crack spacing at the saturation of matrix cracking, $\overline{x}_f$, is uniquely related to δ_R through the relationship

$$\overline{x}_f = \Lambda\left(\rho, \frac{\sigma^*}{\sigma_R}, \frac{\sigma_{th}}{\sigma_R}\right)\delta_R \tag{4.46}$$

where the parameter Λ is a pure number but depends on the four parameters that describe the deformation. A similar form was proposed by Henstenberg and Phoenix [93] with Λ only a function of ρ, and again by Curtin [78] with Λ only a function of ρ and σ^*/σ_R.

Values for the coefficient Λ versus ρ are shown in Fig. 4.9 for a wide range of the other parameter values. Two points are notable. First, the value of Λ is very insensitive to the precise magnitude of the thermal stress. However, Λ is a function of the ratio of σ^*/σ_R and σ_{th}/σ_R whereas the experimentally fit parameters are σ^*-σ_{th} and σ_R-σ_{th}, so the thermal stress is embedded in the determination of σ_R and σ^* from the data. Second, the values of Λ for various combinations of σ^* and ρ can be similar. The value for a large σ^*/σ_R and a low ρ can be quite similar to that for a small σ^*/σ_R but a high ρ. This observation confirms our earlier claims that the precise independent values of ρ and σ^* are not important in determining some physical quantities. A measurement of $\bar{x}_f$ along with the appropriate value of Λ from Fig. 4.9 thus allows for the determination of the important parameter δ_R. Having finally determined δ_R, the value of τ now follows directly from the relationship of Eq. (4.8) i.e.

$$\delta_R = \frac{r_f \alpha}{2\tau}\left\{\left(\sigma_R{}^{th} - \sigma_{th}\right) + \sigma_{th}\right\} = \frac{r_f \alpha}{2\tau}\sigma_R \quad . \tag{4.47}$$

Combining the above Eqs. (4.46) and (4.47), the derived value of τ is thus

$$\tau = \frac{r_f \Lambda}{2\bar{x}_f}\alpha\sigma_R \quad . \tag{4.48}$$

Equations for τ appear often in the literature having exactly the same form as Eq. (4.48) but with several important differences: (i) Λ is often taken to be 1.337 (the value at $\rho=\infty$) or 1.5; (ii) σ_R is replaced by σ^* or some unspecified "matrix cracking stress"; (iii) the role of thermal stress is not accounted for at all.

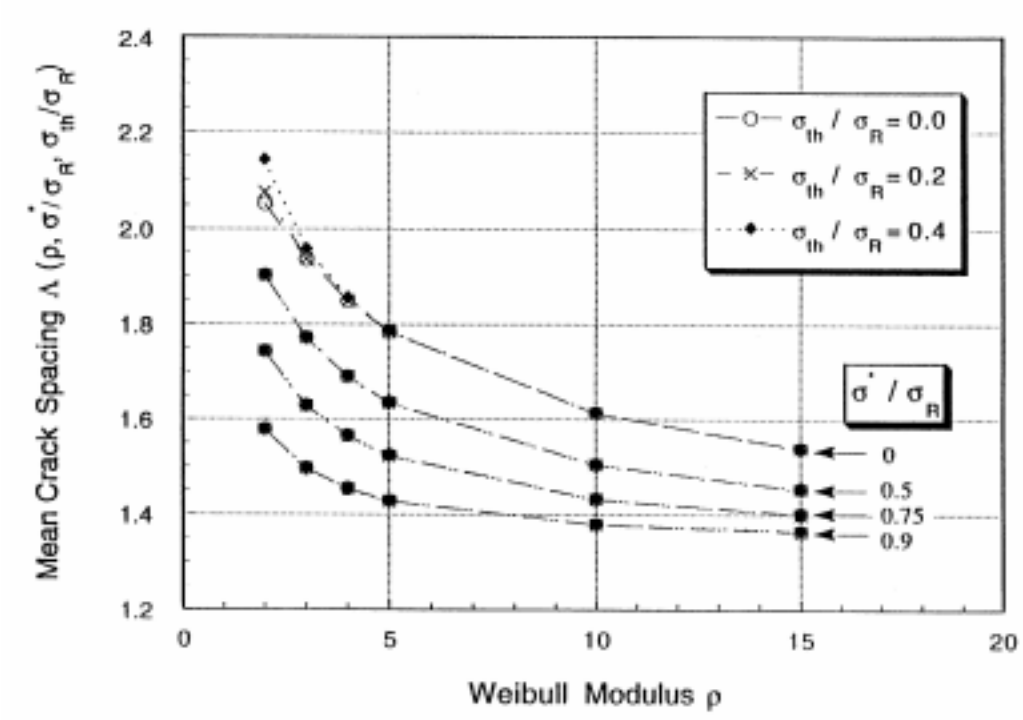

Figure 4.9: Dimensionless final mean crack spacing, $\Lambda = \bar{x}_f / \delta_R$, vs. Weibull modulus ρ for various thermal stresses and σ^*/σ_R. Λ is independent of material properties.

Finally, since the Pryce and Smith result is simple and fairly accurate it is useful to discuss how to apply it to the analysis of experimental data without either (i) measuring crack spacings during the deformation or (ii) using the machinery developed here to determine the evolution of the average crack spacing as input. The former procedure is laborious and should be avoided; the latter provides more detailed information and one might as well use the full results presented here. The suggested procedure is to hypothesize that the evolution of the (normalized) number of matrix cracks versus stress follows a Weibull distribution,

$$\frac{\bar{x}_f}{\bar{x}} = 1 - \exp(-N(\sigma)) \;\; ; \;\; N(\sigma) = \left(\frac{\sigma - (\sigma^* - \sigma_{th})}{(\hat{\sigma}_R - \sigma_{th}) - (\sigma^* - \sigma_{th})} \right)^{\hat{\rho}} \qquad \sigma > \sigma^* - \sigma_{th} \quad , \qquad (4.49)$$

with effective Weibull parameters $\hat{\rho}$ and $\hat{\sigma}_R$, an idea originally proposed by Henstenberg and Phoenix [93] for the related s.f.c. problem. The effective parameters are not actually the underlying and desired parameters ρ and σ_R that describe the matrix crack flaw distribution but rather provide an approximate representation of the crack evolution. The deformation behavior is then fit using the Pryce and Smith results and varying the four parameters $\hat{\sigma}_R$, $\hat{\rho}$, σ_{th} and σ^*. The values of $\hat{\sigma}_R$ and $\hat{\rho}$ are then interpreted as being the proper values σ_R and ρ (although they are not), and τ is obtained just as described above via a measurement of $\bar{x}_f$ and the determination of $\hat{\Lambda} = \Lambda(\hat{\rho}, \sigma^*/\hat{\sigma}_R, \sigma_{th}/\hat{\sigma}_R)$.

To assess the accuracy of the above approach, we consider the example shown in Fig. 4.10 with the known parameters σ_R, ρ=3, σ^* and σ_{th} as "experimental" data to which the approximate PS analysis is then applied. We take σ^* and σ_{th} as given at the proper values and then adjust the remaining two parameters $\hat{\sigma}_R$ and $\hat{\rho}$ to fit the "experimental" deformation. The best-fit parameters are found to be $\hat{\sigma}_R$=1.055σ_R and $\hat{\rho}$=2.0. Using these values in place of the actual σ_R and ρ leads to an estimate of the interfacial τ in terms of $\bar{x}_f$ and other parameters as

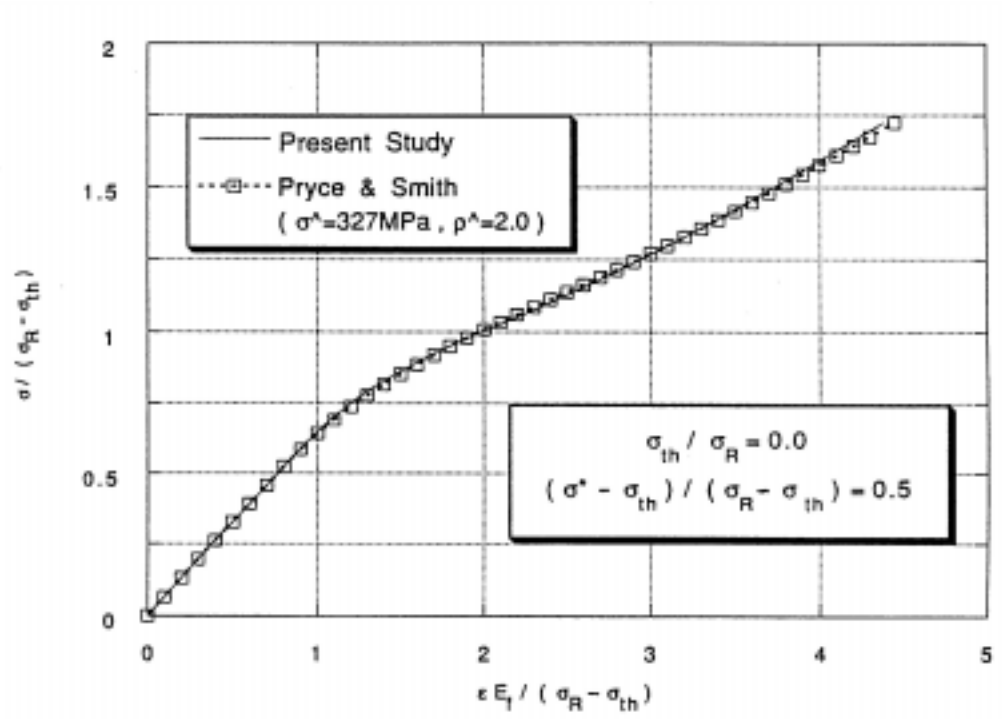

Figure 4.10: Stress/strain curves from the present theory and as fitted using the PS approach with effective Weibull parameters $\hat{\sigma}_R$ and $\hat{\rho}$.

$$\tau = \frac{r_f \hat{\Lambda}}{2\bar{x}_f} \alpha \hat{\sigma}_R \quad . \tag{4.50}$$

This result is larger than the actual value of τ by 14% because $\hat{\sigma}_R > \sigma_R$ and $\hat{\Lambda} > \Lambda$. Note that without an estimate of Λ obtained from Fig. 4.9, the estimated τ would be very inaccurate. Thus, for qualitative purposes the very simple fitting procedure with $\hat{\sigma}_R$ and $\hat{\rho}$ as approximate "statistical parameters" for the matrix cracking is satisfactory if the value of Λ obtained from the full theory is utilized. Such a procedure is easy to use and may be preferable to the more lengthy but more precise analysis discussed above.

4.5. Summary/Discussion

We have presented here a fully statistical theory for the evolution of stress, strain and hysteresis in matrix-cracking ceramic matrix composites. There are two underlying assumptions in the present work. First, the shear lag analysis for fiber and matrix stresses is assumed applicable. Recent work by He *et al*. [94] has shown that a more complete treatment based on a cell model leads to nearly identical results so that the accuracy of the shear lag approximation is acceptable. In principle, the single crack results of He *et al*. could be incorporated into the present framework but the gain in accuracy is probably not worth such an effort. Second, we assume that matrix cracking is driven by a critical stress condition, rather than a critical strain energy release rate condition. The original ACK and BHE results for the onset stress σ^* are energy calculations, and the results of MCE are stress-intensity calculations for isolated single cracks. Zok and Spearing have determined the modified strain energy release rates for long cracks between two surrounding matrix cracks, but no results for shorter cracks are available. Thus, we have adopted the results of MCE as a critical stress condition for the growth of matrix cracks.

Aside from these two important assumptions, the theory is essentially exact. The results for the evolution of matrix cracking as derived by Curtin [77] are not, in fact, exact as

thought earlier. A recent paper by Hui *et al*. [95] demonstrates the exact results. However, the approach taken here and in Curtin [77,78] is extremely accurate when compared to the Hui *et al.* results. This aspect of the present results is thus not considered to be a serious limitation.

We have also considered only the case here in which the interface debond energy is essentially zero. This situation applies only to some composites; in others the debond energy plays a significant role in the evolution of matrix cracking. First, it raises the ACK onset stress to higher values. This can be incorporated into our analysis without difficulty. However, the stress profiles in the fibers and matrix, and the shear stress, change because there is an explicit elastic region of shear relaxation ahead of the debond region. The slip length is modified in this case, and the evolution of cracking is more difficult to assess (see Curtin, [77]). The hysteretic behavior is also changed although this can be incorporated into the analysis if desired. Our goal here has been to assess the effect of the full statistical evolution of cracking on the deformation behavior, and the case of zero debond energy is the conceptually cleanest case in which to perform such a study.

A number of previous workers have attempted to perform analyses of the hysteretic behavior in single fiber "micro-composites", tow-sized "mini-composites", and on full scale composite specimens. None of the recent works deals properly with the statistical evolution of cracking, and occasionally the descriptions of the stress fields in various size fragments are not quite correct. The results presented in our Figs. 4.2, 4.3 and 4.4 for the matrix and fiber stress fields on loading, unloading, and reloading are correct and can be used for general reference. The approximate fitting using Eq. (4.49), the PS equations, and the proper Λ can easily be applied to all of these experiments to derive interfacial slip.

A particular recent emphasis in many of the above recent efforts has been on using the changes in hysteresis loop widths measured under fatigue conditions to assess the fatigue-induced changes in the interfacial sliding resistance τ [96]. If the interface τ decreases

during fatigue, the usual case due to wear of the interface, then the present considerations show that such a change leads to changes in the relative proportions of long, medium, and short fragments in the composite. As τ decreases and the slip length δ increases, the smaller long fragments move into the upper part of the medium fragment distribution while the smaller medium fragments move into the upper part of the short fragment distribution, even though the fragment lengths are not actually changing. The characteristics of the hysteresis loop can thus change somewhat, and the assumption of "long" equal-spaced fragments can lead to misleading deductions on the nature of the changing τ.

We have not applied the present analysis to any real experimental data because of a lack of suitable data. The Nicalon/CAS composites are widely studied, but they are known to undergo fiber failure during matrix cracking [90,94]. This causes additional deformation not associated with the matrix cracking, and applying the present theory would be ill-advised. A combination of matrix cracking and fiber damage can be considered approximately by using the fiber damage constitutive law developed by Curtin and Zhou, and this will be pursued in future work.

In summary, the full stress/strain deformation of ceramic matrix composites during matrix cracking can be characterized by four underlying constituent parameters: statistical parameters σ_R and ρ for the matrix flaw population, the ACK stress σ^*, and the thermal stress σ_{th}. The determination of changes in the deformation behavior with changing temperature, flaw distribution, and interfacial sliding resistance τ can now be calculated using the results presented here. Experimental data can be interpreted using the theory to derive values for important in-situ quantities such as the interfacial sliding resistance τ, and its variations with temperature, exposure to atmospheres, and intrinsic fatigue effects at the microscopic level.

Chapter 5. SUMMARY AND CONCLUSIONS

This study contains two main topics on the micromechanics of ceramic matrix composites. The first part is the behavior of a single matrix crack at the fiber/matrix interface, and the second one is the multiple matrix cracking phenomenon. We also perform the stress analysis around the debond/sliding interface to understand the possible failure mode after interfacial debonding occurs but before multiple matrix cracks are formed. From the applied load perspective, we are interested in between the onset stress for the first matrix crack and the stress at which crack saturation takes place. We have investigated the possible locations of fiber failure using the fiber stress profiles in a matrix-cracked composite, but the detailed research on the fiber failure is not of our interest. Here, the mechanisms for toughening enhancement in fiber-reinforced CMCs, such as a single matrix followed by debonding or the multiple matrix cracking, are our primary concern.

The first part of this research has been contributed to the crack deflection/penetration criterion in a matrix-cracked composite. The numerical tool we use is the Axisymmetric Damage Model (ADM), which was developed by Pagano and his colleagues at Wright-Patterson Air Force Base, Ohio. The model is based on the Reissner's variational theorem and is able to solve the boundary value problems having mixed boundary conditions of stresses and displacements. Our model composite consists of axisymmetric concentric cylinders representing a core fiber and surrounding matrix where the initial crack is formed. Our interest is in the crack propagation after the matrix crack reaches the interface, and we have developed an energy-based criterion to predict the crack deflection or penetration. The criterion is useful for the realistic composites with finite fiber volume fractions and finite crack sizes. Compared to the classic work by He and Hutchinson in which a semi-infinite matrix crack is assumed, the present criterion predicts less tendency for crack deflection especially at high elastic mismatch, and turns out to be consistent with the available experimental data for SCS/glass composites. It appears that the He and

Hutchinson's criterion may overestimate the crack deflection prospects in general. We have also investigated the effects of the crack extensions on the criterion by using several different lengths for the crack extensions. We are interested in this problem because, in the analytic sense, the crack extension could be infinitesimal or nearly zero, but there has not been a clear physical interpretation of this quantity. We have examined the possibility of utilizing the flaw size of the fiber as a crack extension for both deflected and penetrating cracks, and it is shown that the larger flaws lower the possibility of crack deflection.

Before we intensively study the multiple matrix cracking, we have investigated the stress behavior around the sliding interface on the assumption that the matrix crack approaching the interface is deflected onto the interface and develop into a finite debond/sliding zone. In this study we focus more on the debonding rather than the fiber failure; the fiber failure analysis requires extensive research on the statistical aspects of fiber strength and this is beyond our goal of the present study. The stress distributions are obtained using the ADM model with adequate boundary conditions on the material boundary, interface and at the crack tips. We have examined the effects of the extent of debond/slip on the microstress distributions in the matrix and at the interface and on the relative slip of the interface. Through this study we obtain the general idea regarding the relations between the interface conditions (weak or strong interface) and the constituent stresses. We then relate the increasing loading conditions to the axial stresses in the matrix, which play an important role of driving further matrix cracks. The results show that the increasing loading increase the slip length, but the stress in the slip zone remains at the same level, independently of the variation of the loading. That is, the new cracks cannot be formed in the slip zone. This is in fact one of the basic assumptions of the simple shear-lag model used in this study, and the above results are useful to validate the shear-lag model in the calculations of matrix stresses during the evolution of multiple matrix cracking phenomenon. Although we have not studied on the fiber failure in detail, we present some preliminary results to predict the fiber failure locations by evaluating the stress transfer from the cracked matrix to the intact fibers. It appears that, without considering the flaw

distribution or the weakest link concept in the fiber, the most possible spot for fiber break is along the matrix crack plane. We leave this area as a future research topic.

Final topic in this study is the multiple matrix cracking. We have presented a new theory to predict the stress/strain relations and unload/reload hysteresis behavior considering both the statistical aspects (matrix flaw distributions) and the mechanics aspects (crack interactions between neighboring cracks). While most of the previous research works have treated only one of the above aspects, the present theory has been successful in including both aspects. Furthermore, the crack spacings or the matrix crack fragment lengths are assumed stochastic, not equal and uniform. We have extended Curtin's pioneering work which recognized the similarity between the fiber fragmentation in PMCs and the multiple matrix cracking in CMCs and also provided the very accurate solution to the matrix crack problems. From Curtin's work, we have derived the stress/strain relations which is a function of interfacial sliding resistance, thermal residual stress and matrix flaw distributions. We also presented the procedure to obtain the sliding resistance from the experimental data for stress/strain curves and unloading/reloading hysteresis loops. The effects of Weibull parameter and thermal stress on the stress/strain curves and hysteresis loops are investigated. The comparison between the present model and a commonly-used approach in which the crack spacings are equal has been carried out and found that the rough approximation of equal crack spacings results in 10% of discrepancy in the evaluated sliding resistance. The main advantage of the present approach over traditional approaches in applications is that one needs to measure the crack spacings at only one moment such as crack saturation point. This enables one to assess the value of interfacial properties with ease even at high temperatures.

We have made a great deal of achievement in each of the above categories, but we are encouraged to suggest some problem topics for future study. First of all, on the crack deflection criterion, we desire to verify our criterion with more experimental data. In the present study we have used various crack extensions without clearly identifying which one should be acceptable for a specific material system, but we expect that the physical

interpretation of the extension length in connection with the flaw sizes could be clearer if we have enough experimental data to compare our model with. It is worth noting that if the crack extension is heavily flaw size-dependent, then the ideal modeling effort such as the present study would not be enough to analyze the crack behavior at the interface. The manufacturing process and interface roughness would then be key factors to control the *in-situ* properties of the interface.

On the sliding interface problem, we have mainly investigated the effects of some variable factors such as slip length and applied load on the stress distributions; we have not focused on the quantitative assessment on the stress transfer from the broken matrix to the intact fibers. Therefore, more intensive work related to the stress transfer with various boundary conditions will be an interesting area to the ADM model users. Since one can have any type of crack modes in the ADM, as long as the cracks are located parallel or perpendicular to the fiber direction, but not oblique, the stress analysis with various types of cracks will also be a promising field.

Finally on the multiple matrix cracking, we have a plan to consider the interface toughness caused by roughness or adhesion at the interfacial debond crack tip. As Hutchinson and Jensen [63] and Sutcu and Hillig [43] showed, this interface toughness causes discontinuous jumping in the interfacial shear stress and the axial stress in the constituents; then the slip length changes and so do the stress profiles in fiber and matrix. This will eventually affect the stress/strain relations and hysteresis behavior. Another interesting area related to the multiple matrix cracking is the connection of the matrix cracking with the fiber damage. Some of the CMCs show that the fiber failure precedes the extensive matrix cracking, which is not included in our assumptions here, and the fiber damage assumption may explain the fiber failure at early stage of loading history.

REFERENCES

1. Chawla, K.K., *Ceramic Matrix Composites*, Chapman & Hall, New York, 1993.
2. Evans, A.G. and Zok, F.W., "Review: The Physics and Mechanics of Fiber-Reinforced Brittle Matrix Composites," *J. Mater. Sci.*, Vol. 29, pp. 3857-3896, 1994.
3. Evans, A.G., "Design and Life Prediction Issues for High-Temperature Engineering Ceramics and Their Composites," *Acta Mater*., Vol. 45, pp.23-40, 1997.
4. Williams, M.L., "The Stresses Around a Fault or Crack in Dissimilar Media," *Bulletin of the Seismological Society of America*, Vol. 49, pp. 199-204, April, 1959.
5. Dundurs, J., "Edge-Bonded Dissimilar Orthogonal Elastic Wedges Under Normal and Shear Loading," *J. Appl. Mech.*, Vol. 36, pp. 650-652, 1969.
6. Erdogan, F., "Stress Distribution in a Nonhomogeneous Elastic Plane With Cracks," *J. Appl. Mech*., Vol. 30, pp. 232-236, 1963.
7. Erdogan, F., "Stress Distribution in Bonded Dissimilar Materials With Cracks," *J. Appl. Mech*., Vol. 32, pp. 403-410, 1965.
8. Rice, J.R. and Sih, G.C., "Plane Problems of Cracks in Dissimilar Media," *J. Appl. Mech.*, Vol. 32, pp. 418-423, 1965.
9. Rice, J.R., "Elastic Fracture Mechanics Concepts for Interfacial Cracks," *J. Appl. Mech*., Vol. 55, pp. 98-103, 1988.
10. Hutchinson, J.W., Mear, M.E. and Rice, J.R., "Crack Paralleling an Interface Between Dissimilar Materials," *J. Appl. Mech.*, Vol. 54, pp. 828-832, 1987.
11. Zak, A.R. and Williams, M.L., "Crack Point Stress Singularities at a Bi-Material Interface," *J. Appl. Mech*., Vol. 30, pp. 142-143, 1963.
12. He, M.-Y., McMeeking, R.M. and Zhang, N.T., "Small Scale Yielding at a Crack Normal to the Interface Between an Elastic and Yielding Material," *Proc. Materials Research Society Symposium*, Vol. 239, pp. 585-590, Boston, 1992.
13. Hutchinson, J.W. and Suo, Z, "Mixed Mode Cracking in Layered Materials," *Advances in Appl. Mech.*, Ed. by Hutchinson, J.W. and Wu, T.W., Vol. 29, pp. 63-191, 1991.
14. Delfin, P., Gunnars, J. and Stahle, P., "Effect of Elastic Mismatch on the Growth of a Crack Initially Terminated at an Interface in Elastic Plastic Bimaterials," *Fatigue Fract. Engng. Mater. Struct.*, Vol. 18, pp. 1201-1212, 1995.
15. Cook, J. and Gordon, J.E., "A Mechanism for the Control of Crack Propagation in All-Brittle Systems, "*Proc. Royal Society*, Vol. A282, pp. 508-520, 1964.
16. Gupta, V., Yuan, J. and Martinez, D., "Calculation, Measurement, and Control of Interface Strength in Composites," *J. Am. Ceram. Soc*. Vol. 76, pp. 305-315, 1993.
17. He, M.-Y. and Hutchinson, J.W., "Crack Deflection at an Interface Between Dissimilar Elastic Materials," *Int. J. Solids Struct.*, Vol. 25, pp. 1053-1067, 1989.
18. Martinez, D. and Gupta, V., "Energy Criterion for Crack Deflection at an Interface Between Two Orthotropic Media," *J. Mech. Phys. Solids*, Vol. 42, pp. 1247-1271, 1994.
19. He, M.Y., Evans, A.G. and Hutchinson, J.W., "Crack Deflection at an Interface Between Dissimilar Elastic Materials: Role of Residual Stresses," *Int. J. Solids Struct.*, Vol. 31, pp. 3443-3455, 1994.

20. Charlalambides, P.G., Lund, J., Evans, A.G. and McMeeking R.M., "A Test Specimen for Determining the Fracture Resistance of Bimaterial Interfaces," *J. Appl. Mech.*, Vol. 56, 77-82, 1989.
21. Langhaar, H.L., *Energy Method in Applied Mechanics*, Krieger Publishing Co., Malabar, Florida, 1962.
22. Reissner, E., "On a Variational Theorem in Elasticity," *J. Math. Physics*, Vol. 29, pp. 90-95, 1950.
23. Pagano, N.J., "Stress Fields in Composite Laminates," *Int. J. Solids Struct.*, Vol. 14, pp. 385-400, 1978.
24. Pagano, N.J., "Axisymmetric Stress Fields in Involute Bodies of Revolution," *J. Spacecraft*, Vol. 23, pp. 165-170, 1986.
25. Pagano, N.J., "Axisymmetric Micromechanical Stress Fields in Composites," *Proc. 1991 IUTAM Symp. on Local Mechanics Concepts for Composite Materials Systems*, pp. 1-16, Virginia Polytechnic Institute and State University, Blacksburg, Virginia, 1991.
26. Pagano, N.J. and Brown III, H.W., "The Full-Cell Cracking Mode in Unidirectional Brittle-Matrix Composites," *Composites*, Vol. 24, pp.69-83, 1993.
27. Tandon, G.P. and Pagano, N.J., "Matrix Crack Impinging on a Frictional Interface in Unidirectional Brittle Matrix Composites," *Int. J. Solids Struct.*, Vol. 33, pp. 4309-4326, 1996.
28. Kasano, H., Matsumoto, H. and Nakahara, I., "A Torsion-Free Axisymmetric Problem of a Cylindrical Crack in a Transversely Isotropic Body," *Bulletin of JSME*, Vol. 27, pp. 1323-1332, 1984.
29. Kasano, H., Matsumoto, H. and Nakahara, I., "A Cylindrical Interface Crack in a Nonhomogeneous Anisotropic Elastic Body," *Bulletin of JSME*, Vol. 29, pp. 1973-1981, 1986.
30. Pagano, N.J., "On the Micromechanical Failure Modes in a Class of Ideal Brittle Matrix Composites, Part 1: Axial Tension Loading of Coated-Fiber Composites," *to appear in Composites B*, 1997.
31. Pagano, N.J., "On the Micromechanical Failure Modes in a Class of Ideal Brittle Matrix Composites, Part 2: Axial Tension Loading of Uncoated-Fiber Composites," *to appear in Composites B*, 1997.
32. Tandon, G.P. and Schoeppner, G.A., *Axisymmetric Damage Model User Manual*, US Air Force Wright Laboratory, 1996.
33. Gambone, M.L., "The Fiber Strength Distribution and Its Effect on the Creep Behavior of a SiC/Ti-1100 Composite," *Ph.D. Thesis*, School of Engineering and Applied Science, University of Virginia, 1995.
34. Gustafson, C.M., Dutton, R.E. and Kerans, R.J., "Fabrication of Glass Matrix Composites by Tape Casting," *J. Am. Ceram. Soc.*, Vol. 78, pp. 1423-1424, 1995.
35. Lee, W., Howard, S.J. and Clegg, W.J., "Growth of Interface Defects and Its Effect on Crack Deflection and Toughening Criteria," *Acta Mater.*, Vol. 44, pp. 3905-3922, 1996.
36. Herrera-Franco, P.J. and Drzal, L.T., "Comparison of Methods for the Measurement of Fiber/Matrix Adhesion in Composites," *Composites*, Vol. 23, pp. 2-27, 1992.

37. Swain, R.E., Reifsnider, K.L., Jayaraman, K. and El-Zein, M., "Interface/Interphase Concepts in Composite Materials Systems," *J. Thermoplastic Comp. Mater.*, Vol. 3, pp. 13-23, 1990.
38. Aveston, J., Cooper, G. and Kelly, A., "Single and Multiple Fracture: The Properties of Fiber Composites," *Proc. Nat. Phys. Lab.*, pp. 15-26, IPS Science and Technology Press Ltd., Surrey, U.K., 1971.
39. Marshall, D.B., Cox, B.N., and Evans, A.G., "The Mechanics of Matrix Cracking in Brittle Matrix Fiber Composites," *Acta Metall.*, Vol. 33, pp. 2013-2021, 1985.
40. Budiansky, B. Hutchinson, J.W., and Evans, A.G., "Matrix Fracture in Fiber-Reinforced Ceramics," *J. Mech. Phys. Solids*, Vol. 34, pp. 167-189, 1986.
41. McCartney, L.N., "Mechanics of Matrix Cracking in Brittle-Matrix Fiber-Reinforced Composites," *Proc. R. Soc. Lond.*, Vol. A409, pp. 329-350, 1987.
42. Wijeyewickrema, A.C. and Keer, L.M., "Matrix Cracking in a Fiber Reinforced Composite with Slip at the Fiber-Matrix Interface," *Int. J. Solids Struct.*, Vol. 30, pp. 91-113, 1993.
43. Sutcu, M. and Hillig, W.B., "The Effect of Fiber-Matrix Debond Energy on the Matrix Cracking Strength and the Debond Shear Strength," *Acta Metall. Mater.*, Vol. 38, pp. 2653-2662, 1990.
44. Steif, P.S. and Dollar, A., "Longitudinal Shearing of a Weakly Bonded Fiber Composites," *Metall. Trans. A*, Vol. 19A, p. 129, 1988.
45. Gao, Y.C., Mai, Y.W. and Cotterell, B, "Fracture of Fiber Reinforced Materials," *J. Appl. Math. Phys. (Zamp)*, Vol. 39, pp. 550-572, 1988.
46. McCartnery, L.N., "New Theoretical Model of Stress Transfer Between Fiber and Matrix in a Uniaxially Fiber-Reinforced Composite," *Proc. R. Soc. Lond.*, Vol. A425, pp. 215-244, 1989.
47. Steif, P.S., "Stiffness Reduction Due to Fiber Breakage," *J. Comp. Mater.*, Vol. 18, pp. 153-172, 1984.
48. Dollar, A. and Steif, P.S., "Load Transfer in Composites with a Coulomb friction Interface," *Int. J. Solids Struct.*, Vol. 24, pp. 789-803, 1988.
49. Dollar, A. and Steif, P.S., "A Tension Crack Impinging Upon Frictional Interfaces," *J. Appl. Mech.*, Vol. 56, pp. 291-298, 1989.
50. Schwietert, H.S. and Steif, P.S., "An Interface Integral Equation Method Applied to a Crack Impinging upon a Bimaterial, Frictional Interface," *Int. J. Fract.*, Vol. 49, pp. 257-272, 1991.
51. Meda, G., Hoysan, S.F. and Steif, P.S., "The Effect of Fiber Poisson Expansion in Micro-Indentation Tests," *J. Appl. Mech.*, Vol. 60, pp. 986-991, 1993.
52. Pagano, N.J. and Tandon, G.P., "Modeling of Imperfect Bonding in Fiber-Reinforced Brittle Matrix Composites," *Mech. Mater.*, Vol. 9, pp. 49-64, 1990.
53. Kaw, A.K. and Pagano, N.J., "Axisymmetric Thermoelastic Response of a Composite Cylinder Containing an Annular Crack," *J. Comp. Mater.*, Vol. 27, pp.540-571, 1993.
54. Kaw, A.K., Kunchithapatham, S. and Pagano, N.J., "The Stress Field in a Cracked Brittle Matrix Composite Cylinder with a Frictional Interface," *Int. J. Solids Struct.*, Vol. 32, pp. 2127-2154, 1995.
55. Tandon, G.P. and Pagano, N.J., "Micromechanical Analyses of Unidirectional Brittle Matrix Composites with Frictional Interfaces," *Proc. the ASME Matl. Div.*, Vol. 69-1, pp. 265-275, 1995.

56. Evans, A.G., Zok, F.W. and Davis, J., "The Role of Interfaces in Fiber-Reinforced Brittle Matrix Composites," *Comp. Sci. Technol.*, Vol. 42, pp. 3-24, 1991.
57. Thouless, M.D. and Evans, A.G., "Effects of Pull-Out on the Mechanical Properties of Ceramic-Matrix Composites," *Acta Metall.*, Vol. 36, pp. 517-522, 1988.
58. Sutcu, M., "Weibull Statistics Applied to Fiber Failure in Ceramic Composites and Work of Fracture," *Acta Metall.*, Vol. 37, pp. 651-661, 1989.
59. Cox, H.L., "The Elasticity and Strength of Paper and Other Fibrous Materials," *British J. Appl. Phys.*, Vol. 3, pp. 72-79, 1952.
60. Aveston, J and Kelly, A., "Theory of Multiple Fracture of Fibrous Composites," *J. Mater. Sci.*, Vol. 8, pp. 352-362, 1973.
61. Piggot, M.R., "Expressions Governing Stress-Strain Curves in Short Fiber Reinforced Polymers," *J. Mater. Sci.*, Vol. 13, pp. 1709-1716, 1978.
62. Sigl, L.S. and Evans, A.G., "Effects of Residual Stress and Frictional Sliding on Cracking and Pullout in Brittle Matrix Composites," *Mech. Mater.*, Vol. 8, pp. 1-12, 1989.
63. Hutchinson, J.W. and Jensen, "Models of Fiber Debonding and Pullout in Brittle Composites with Friction," *Mech. Mater.*, Vol. 9, pp. 139-163, 1990.
64. Hsueh, C.-H., "Interfacial Debonding and Fiber Pull-Out Stresses of Fiber-Reinforced Composites," *Mater. Sci. Engng.*, Vol. A123, pp. 1-11, 1990.
65. Hsueh, C.-H., "Interfacial Debonding and Fiber Pull-Out Stresses of Fiber-Reinforced Composites II: Non-Constant Interfacial Bond Strength," *Mater. Sci. Engng.*, Vol. A125, pp. 67-73, 1990.
66. Marshall, D.B., "An Indentation Method for Measuring Matrix-Fiber Frictional Stresses in Ceramic Composites," *Comm. Am. Ceram. Soc.*, C 259-260, 1984.
67. Takaku, A. and Arridge, R.G.C., "The Effect of Interfacial Radial and Shear Stress on Fiber Pull-Out in Composite Materials," *J. Phys. D: Appl. Phys.*, Vol. 6, pp. 2038-2047, 1973.
68. Shetty, D.K., "Shear-Lag Analysis of Fiber Push-Out (Indentation) Tests for Estimating Interfacial Friction Stress in Ceramic-Matrix Composites," *J. Am. Ceram. Soc.*, Vol. 71, pp. C107-C109, 1988.
69. Weitsman, Y. and Zhu, H., "Multi-Fracture of Ceramic Composites," *J. Mech. Phys. Solids*, Vol. 41, pp. 351-388, 1993.
70. Carman, G.P., Averill, R.C., Reifsnider, K.L., and Reddy, J.N., "Optimization of Fiber Coatings to Minimize Stress Concentrations in Composite Materials," *J. Comp. Mater.*, Vol. 27, pp.589-612, 1993.
71. Tsai, H.C., Arocho, A.M. and Gause, L.W., "Prediction of Fiber-Matrix Interphase Properties and Their Influence on Interface Stress, Displacement and Fracture Toughness of Composite Material," *Mater. Sci. Eng.*, Vol. A126, pp. 295-304, 1990.
72. Piggot, M.R., "The Effect of the Interface/Interphase on Fiber Composite Properties," *Polymer Comp.*, Vol. 8, pp. 291-297,1987.
73. Giurgiutiu, V., Reifsnider, K.L., Kriz, R., Ahn, B.K. and Lesko, J.J., "Influence of Fiber Coating and Interphase on the Design of Polymeric Composites Strength: Analytic Predictions," *Proc. 36th AIAA/ASME/ASCE/AHS/ACS Structural Dynamics and Materials Conference*, New Orleans, LA, 1995.

74. Droillard, C. and Lamon, J., "Fracture Toughness of 2-D Woven SiC/SiC CVI-Composites with Multilayered Interphases," *J. Am. Ceram. Soc.*, Vol. 79, pp. 849-858, 1996.
75. Curtin, W.A., Halverson, H., Ahn, B.K. and Carter, R.H., "Mechanical Testing and Mechanical Modeling of SiC/SiC Composites with Multilayer SiC Interface Coatings," *Final Project Report*, 1996.
76. Xia, Z.C., Hutchinson, J.W., Evans, A.G. and Budiansky, B., "On Large Scale Sliding in Fiber-Reinforced Composites," *J. Mech. Phys. Solids*, Vol. 42, pp. 1139-1158, 1994.
77. Curtin, W.A., "Exact Theory of Fiber Fragmentation in a Single-Filament Composite," *J. Mater. Sci.*, Vol. 26, pp. 5239-5253, 1991.
78. Curtin, W.A. "Multiple Matrix Cracking in Brittle Matrix Composites," *Acta Metall. Mater.*, Vol. 41, pp. 1369-1377, 1993.
79. Evans, A.G., Domergue, J.M. and Vagaggini, E., "A Methodology for Relating the Tensile Constitutive Behavior of Ceramic Matrix Composites to Constituent Properties," *High Temperature Ceramic Matrix Composites*, Ed. R. Naslain *et al*., pp. 5-35, 1993.
80. Pryce, A.W. and Smith, P.A., "Matrix Cracking in Unidirectional Ceramic Matrix Composites Under Quasi-Static and Cycling Loading," *Acta Metall. Mater.*, Vol. 41, pp. 1269-1281, 1993.
81. Vagaggini, E., Domergue, J.-M., and Evans, A.G., "Relationships Between Hysteresis Measurements and the Constituent Properties of Ceramic Matrix Composites, I: Theory," *J. Am. Ceram. Soc*., Vol. 78, pp. 2709-2720, 1995.
82. Domergue, J.-M., Vagaggini, E., and Evans, A.G., "Relationships between Hysteresis Measurements and the Constituent Properties of Ceramic Matrix Composites, II: Experimental Studies on Unidirectional Materials," *J. Am. Ceram. Soc*., Vol. 78, pp. 2721-2731, 1995.
83. Morscher, G.N., Martinez-Fernandez, J., and Purdy, M.J., "Determination of Interfacial Properties Using a Single Fiber Microcomposite Test," submitted to *J. Am. Ceram. Soc.*, 1995.
84. Lamon, J., Rebillat, F., and Evans, A.G., "Microcomposite Test Procedure for Evaluating the Interface Properties of Ceramic Matrix Composites," *J. Am. Ceram. Soc.*, Vol. 78, pp. 401-405, 1995.
85. Marshall, D.B., "Analysis of Fiber Debonding and Sliding Experiments in Brittle Matrix Composites," *Acta Metall. Mater.*, Vol. 40, pp. 427-441, 1992.
86. Zok, F.W. and Spearing, S.M., "Matrix Crack Spacing in Brittle Matrix Composites," *Acta Metall. Mater.*, Vol. 40, pp. 2033-2043, 1992.
87. Spearing, S.M. and Zok, F.W., "Stochastic Aspects of Matrix Cracking in Brittle Matrix Composites," *J. Eng. Mater. Tech.*, Vol. 115, pp. 314-318, 1993.
88. Yang, X.F. and Knowles, K.M., "The One-Dimensional Car Parking Problem and Its Application to the Distribution of Spacings between Matrix Cracks in Unidirectional Fiber-Reinforced Brittle Materials," *J. Am. Ceram. Soc.*, Vol. 75, pp. 141-147, 1992.
89. Neumeister, J.M., "A Constitutive Law for Continuous Fiber Reinforced Brittle Matrix Composites with Fiber Fragmentation and Stress Recovery," *J. Mech. Phys. Solid.*, Vol. 41, pp. 1383-1404, 1993.

90. Curtin, W.A. and Zhou, S.J., "Influence of Processing Damage on Performance of Fiber-Reinforced Composites," *J. Mech. Phys. Solids*, Vol. 43, pp.343-363, 1995.
91. Rouby, D. and Navarre, G., "Role of Interfaces on Mechanical Properties of Ceramic-Ceramic Fiber Composites," *Proc. 11th Risϕ Int. Symp. in Structural Ceramics, Processing, Microstructure and Properties,* Risϕ Nat'l Lab., pp. 127-144, Roskilde, Denmark, 1990.
92. Zhu, H. and Weitsman, Y., "The Progression of Failure Mechanisms in Unidirectionally Reinforced Ceramic Materials," *J. Mech. Phys. Solids*, Vol. 42, pp. 1601-1632, 1994.
93. Henstenburg, R.B. and Phoenix, S.L., "Interfacial Shear Strength Studies Using the Single-Filament-Composite Test, Part II: A Probability Model and Monte Carlo Simulation," *Polymer Composites*, Vol. 10, pp. 389-408, 1989.
94. He, M.Y., Wu, B.-X., Evans, A.G. and Hutchinson, J.W., "Inelastic Strains Due to Matrix Cracking in Unidirectional Fiber-Reinforced Composites," *Mech. Mater.*, Vol. 18, pp. 213-229, 1994.
95. Hui, C.-Y., Phoenix, S.L., Ibnabdeljalil, M. and Smith, R.L., "An Exact Closed Form Solution for Fragmentation of Weibull Fibers in a Single Filament Composite With Applications to Fiber-Reinforced Ceramics," *J. Mech. Phys. Solids*, Vol. 43, pp. 1551-1585, 1995.
96. Evans, A.G., Zok, F.W. and McMeeking, R.M., "Fatigue of Ceramic Matrix Composites," *Acta Metall. Mater.*, Vol. 43, pp. 859-875, 1995.
97. Widom, B., "Random Sequential Addition of Hard Spheres to a Volume," *J. Chem. Phys.*, Vol. A4, pp. 3888-3894, 1966.

APPENDIX A

Detailed expressions for μ_{iJ}, χ_{iJ}, F and H in Eq. (2.19) are presented here.

$$\frac{\delta J_k}{2\pi} = \int_{z_1}^{z_2} \Big[(\mu_{iJ} + \chi_{iJ})\delta p_{iJ} + r_2(p_{32}\delta u_2 + p_{52}\delta w_2) - r_1(p_{32}\delta u_1 + p_{51}\delta w_1)$$
$$- r_1(p_{32}\delta u_1 + p_{51}\delta w_1) - (F_1\delta\bar{u} + F_2\delta\hat{u} + F_3\delta\breve{u} + F_4\delta\bar{u} + F_7\delta\hat{w} + F_8\delta\breve{w})\Big]^k dz \qquad (2.19)$$
$$+ \Big[(H_1\delta\bar{u} + H_3\delta\breve{u} + H_4\delta\bar{u} + H_7\delta\hat{w} + H_8\delta\breve{w})^k \Big]_{z=z_1}^{z=z_2} - \int_{L_k'} (\tilde{T}_r\delta u + \tilde{T}_z\delta w) r dL_k$$

where

$$\chi_{iJ} = \eta_{iJ} - E_{iJ} - s_{ijKJ}\, p_{jK} \qquad (i,j = 1,2,3,5;\ J,K = 1,2,\ldots 5) \qquad (A.1)$$

with

$$E_{iJ} = \int_{r_1}^{r_2} e_i\, f_J^{(i)} r dr \qquad (i,j = 1,2,3,5;\ J,K = 1,2,\ldots 5)\ , \qquad (A.2)$$

and

$$s_{ijKJ} = \int_{r_1}^{r_2} S_{ij}\, f_K^{(j)}\, f_J^{(i)} r dr \qquad (i,j = 1,2,3,5;\ J,K = 1,2,\ldots 5)\ . \qquad (A.3)$$

Also, the following definitions have been employed in Eq. (A.1).

$$\eta_{11} = \frac{r_2\hat{w}' - \breve{w}'}{r_2 - r_1}\ , \qquad \eta_{12} = \frac{\breve{w}' - r_1\hat{w}'}{r_2 - r_1}\ ,$$

$$\eta_{21} = \frac{r_2\bar{u} - \hat{u}}{r_2 - r_1}\ , \qquad \eta_{22} = \frac{\hat{u} - r_1\bar{u}}{r_2 - r_1}\ ,$$

$$\eta_{31} = \frac{2\hat{u} - r_2\bar{u}}{r_2 - r_1}\ , \qquad \eta_{32} = \frac{r_1\bar{u} - 2\hat{u}}{r_2 - r_1}\ ,$$

$$\eta_{33} = -r_1r_2(r_1 + r_2)\bar{u} + 2(r_1^2 + r_1r_2 + r_2^2)\hat{u} - 4\bar{u}\ , \qquad (A.4)$$

$$\eta_{34} = -r_1r_2\bar{u} + 2(r_1 + r_2)\hat{u} - 3\breve{u}\ ,$$

$$\eta_{35} = \begin{cases} \dfrac{(r_1 + r_2)\bar{u} - 2\hat{u}}{r_1r_2} & \text{if } r_1 \neq 0 \\ 0 & \text{if } r_1 = 0 \end{cases}\ ,$$

$$\eta_{51} = \begin{cases} \dfrac{3\breve{w} - 2r_2\hat{w} + r_2\breve{u}' - \hat{u}'}{r_1(r_2 - r_1)} & \text{if } r_1 \neq 0 \\ 0 & \text{if } r_1 = 0 \end{cases},$$

$$\eta_{52} = \begin{cases} \dfrac{2r_1\hat{w} - 3\breve{w} + \hat{u} - r_1\tilde{u}}{r_2(r_2 - r_1)} & \text{if } r_1 \neq 0 \\ \dfrac{\breve{u}' - 2\hat{w}}{r_2} & \text{if } r_1 = 0 \end{cases},$$

$$\eta_{53} = \begin{cases} \dfrac{(r_1^2 + r_1r_2 + r_2^2)(2\hat{w} - \breve{u}') + (r_1 + r_2)(\hat{u}' - 3\breve{w}) + r_1^2r_2^2\bar{u}'}{r_1^2r_2^2} & \text{if } r_1 \neq 0 \\ 2r_2\hat{w} - 3\breve{w} + \bar{u}' - r_2\breve{u}' & \text{if } r_1 = 0 \end{cases},$$

with

$$\eta_{iJ} = 0 \quad (i = 1,2 \text{ and } J = 3,4,5 \text{ or } i = 5 \text{ and } J = 4,5) \quad , \tag{A.5}$$

and

$$\begin{aligned} &\mu_{31} = -r_1u_1 \quad , \quad \mu_{51} = -r_1w_1 \quad , \\ &\mu_{32} = -r_2u_2 \quad , \quad \mu_{52} = r_2w_2 \quad , \end{aligned} \tag{A.6}$$

with

$$\mu_{iJ} = 0 \ (i = 1,2 \text{ or } J = 3,4,5) \quad . \tag{A.7}$$

Finally, the following contractions have been used in Eq. (2.19) for the case of $r_1 \neq 0$.

$$\begin{aligned} F_1 = &\frac{r_2p_{31} - r_1p_{32}}{r_2 - r_1} + r_1r_2(r_1 + r_2)p_{33} + r_1r_2p_{34} \\ &- \frac{(r_1 + r_2)p_{35}}{r_1r_2} + \frac{r_1p_{22} - r_2p'_{21}}{r_2 - r_1} + p'_{53} \end{aligned} \quad ,$$

$$F_2 = \frac{2(p_{32} - p_{31})}{r_2 - r_1} - 2(r_1^2 + r_1 r_2 + r_2^2) p_{33}$$
$$-2(r_1 + r_2) p_{34} + \frac{2 p_{35}}{r_1 r_2} + \frac{p_{21} - p_{22}}{r_2 - r_1} \quad ,$$

$$F_3 = 3p_{34} + \frac{r_2^2 p'_{51} - r_1^2 p'_{52}}{r_1 r_2 (r_2 - r_1)} - \frac{(r_1^2 + r_1 r_2 + r_2^2) p'_{53}}{r_1^2 r_2^2} \quad , \qquad \text{(A.8)}$$

$$F_4 = 4p_{33} + \frac{r_1 p'_{52} - r_2 p'_{51}}{r_1 r_2 (r_2 - r_1)} + \frac{(r_1 + r_2) p'_{53}}{r_1^2 r_2^2} \quad ,$$

$$F_7 = \frac{r_2 p'_{11} - r_1 p'_{12}}{r_2 - r_1} + \frac{2(r_2^2 p_{51} - r_1^2 p_{52})}{r_1 r_2 (r_2 - r_1)} - \frac{2(r_1^2 + r_1 r_2 + r_2^2) p_{53}}{r_1^2 r_2^2} \quad ,$$

$$F_8 = \frac{p'_{12} - p'_{11}}{r_2 - r_1} + \frac{3(r_1 p_{52} - r_2 p_{51})}{r_1 r_2 (r_2 - r_1)} + \frac{3(r_1 + r_2) p_{53}}{r_1^2 r_2^2} \quad ,$$

and

$$H_1 = p_{53} \quad ,$$

$$H_3 = \frac{r_2^2 p_{51} - r_1^2 p_{52}}{r_1 r_2 (r_2 - r_1)} - \frac{(r_1^2 + r_1 r_2 + r_2^2) p_{53}}{r_1^2 r_2^2} \quad , \qquad \text{(A.9)}$$

$$H_4 = \frac{r_1 p_{52} - r_2 p_{51}}{r_1 r_2 (r_2 - r_1)} + \frac{(r_1 + r_2) p_{53}}{r_1^2 r_2^2} \quad ,$$

while, if $r_1 = 0$, instead of Eqs. (A.8) and (A.9), we have

$$F_1 = p_{31} - p_{21} \quad ,$$

$$F_2 = \frac{2(p_{32} - p_{31}) + p_{21} - p_{22}}{r_2} - 2r_2^2 p_{33} - 2r_2 p_{34} \quad ,$$

$$F_3 = 3p_{34} + \frac{p'_{52}}{r_2} - r_2 p'_{53} \quad , \qquad \text{(A.10)}$$

$$F_4 = 4p_{33} + p'_{53} \quad ,$$

$$F_7 = p'_{11} + 2\frac{p_{52}}{r_2} - 2r_2 p_{53} \quad ,$$

$$F_8 = \frac{p'_{12} - p'_{11}}{r_2} + 3p_{53} \quad ,$$

and

$$H_1 = 0 \quad ,$$

$$H_3 = \frac{p_{52}}{r_2} - r_2 p_{53} \quad , \tag{A.11}$$

$$H_4 = p_{53} \quad ,$$

while

$$H_7 = \frac{r_2 p_{11} - r_1 p_{22}}{r_2 - r_1} \quad ,$$

$$H_8 = \frac{p_{12} - p_{11}}{r_2 - r_1} \tag{A.12}$$

hold for any value of r_1.

APPENDIX B

In Chapter 4, we mentioned that the crack spacing distribution is divided into three categories according to the fragment length. The fragment distribution of the entire matrix is the sum of $P_L(x)$, $P_M(x)$ and $P_S(x)$ at the given applied stress. The desired distributions for long and medium fragments are related to Widom's distribution of gaps $q(x;\eta)$ by

$$P(x;\eta) = \frac{1}{\eta\delta} q(x;\eta) \quad , \tag{B.1}$$

where η is the dimensionless fiber break density in the long and medium fragments taken together, $\eta = N\delta/L$, with N and L the number and total length, respectively, of the long and medium fragments taken together [97].

$$\begin{aligned} q(x;\eta) &= 2\int_0^{\eta} d\eta' \psi(\eta') e^{-\left(x/\delta - 1\right)\psi(\eta')} \quad , \quad \delta < x < 2\delta \quad (Medium) \\ &= \frac{\psi^2(\eta)}{\psi'(\eta)} e^{-\left(x/\delta - 2\right)\psi(\eta)} \quad , \quad x > 2\delta \quad (Long) \quad . \end{aligned} \tag{B.2}$$

The auxiliary function ψ is defined implicitly by

$$\eta = \int_0^{\psi} dt \exp\left(-2\int_0^t ds \frac{1 - e^{-s}}{s} \right) \quad . \tag{B.3}$$

The distribution for short fragments, $P_S(x)$, is to be obtained from the following evolution equation which connects $P(x)$ (actually $P_M(x)$ here) to $P_S(x)$ at $x = \delta$

$$\frac{dP_S(x)}{d\sigma} = NP(\delta;\eta) \frac{d\delta}{d\sigma} \delta_D(x - \delta) \ , \tag{B.4}$$

where δ_D denotes the Dirac delta function. The evolution of N and L is also needed to analyze the matrix cracking evolution, and the differential equations involving these processes are as follows:

$$\frac{dL}{d\sigma} = -N\delta P(\delta;\eta)\frac{d\delta}{d\sigma} \quad , \tag{B.5}$$

$$\frac{dN}{d\sigma} = -NP(\delta;\eta)\frac{d\delta}{d\sigma} + \frac{d\Phi(\sigma, L^*)}{d\sigma} \quad , \tag{B.6}$$

$$L^* = N\int_{2\delta}^{\infty} dx\,(x-2\delta)P(x;\eta) \quad . \tag{B.7}$$

L^* is the total length of the remaining matrix able to incorporate a break, i.e. the total length of long fragments minus their slip regions. By solving the above equations with the initial conditions $L(0)=L_T$, $N(0)=0$ and $P_S(\sigma=0)=0$, we can keep track of the crack spacing distribution moments for the three types of fragments which are defined in Eqs. (4.19) - (4.21) of Chapter 4. Substituting Eqs. (B.1) and (B.2) into Eqs (4.19) and (4.20) and rearranging the expressions in terms of slip length δ and auxiliary function ψ, we finally have the moments of distributions L_0, L_1, M_0, M_1 and M_2:

$$L_0 = \frac{L}{\delta^2}\int_{2\delta}^{\infty} dx \frac{\psi^2}{\psi'} e^{-\frac{\psi}{\delta}(x-2\delta)} \quad , \tag{B.8}$$

$$L_1 = \frac{L}{\delta^2}\int_{2\delta}^{\infty} dx\, x \frac{\psi^2}{\psi'} e^{-\frac{\psi}{\delta}(x-2\delta)} \quad , \tag{B.9}$$

and

$$M_0 = \frac{2L}{\delta^2}\int_0^{\eta} d\eta' \psi \int_{\delta}^{2\delta} dx\, e^{-\frac{\psi}{\delta}(x-\delta)} \quad , \tag{B.10}$$

$$M_1 = \frac{2L}{\delta^2}\int_0^{\eta} d\eta' \psi \int_{\delta}^{2\delta} dx\, x\, e^{-\frac{\psi}{\delta}(x-\delta)} \quad , \tag{B.11}$$

$$M_2 = \frac{2L}{\delta^2}\int_0^{\eta} d\eta' \psi \int_{\delta}^{2\delta} dx\, x^2\, e^{-\frac{\psi}{\delta}(x-\delta)} \quad . \tag{B.12}$$

The integrals over x are easily evaluated analytically, leaving integrals over η.

For short fragment distributions, we use Eq. (B.4) to calculate $P_S(x)$. In fact, S_0 is the total number of short fragments at the present applied stress, S_1 is the mean length of short fragments, and S_2 is equivalent to the mean square length of short fragments.

VITA

Byung Ki Ahn was born on October 25, 1963, to Yoon-Mo Ahn and Sang-Sook Nam in Seoul, Korea. He graduated from Seoul National University with his B.S. in 1986, and M.S. in 1988, both in Mechanical Design and Production Engineering. After serving in the Korean Army as a second lieutenant, he came to the United States in 1990 to broaden his academic knowledge. He spent a semester at Old Dominion University in Norfolk, Virginia where his eyes were opened to the micromechanics of composite materials and transferred to Virginia Tech in the fall of 1991. He completed his Ph.D. in Engineering Mechanics, with an emphasis on Interfacial Mechanics in Ceramic Matrix Composites, in December 1997. While in Blacksburg, he served as an administrative committee member at the Korean Baptist Church for five years and as vice-president of the Korean Students Association of Virginia Tech in 1995-1996. Despite a long journey to this academic achievement, Byung Ki still wishes to further explore the field of composite materials, and has started his career as a postdoctoral research associate at Virginia Tech. With his wife Jaewon, he has a daughter, Grace Hayne.